

MASTER

Turbulence in the merging wakes of a honeycomb and two side channels

Koster, Chiel

Award date:
2022

[Link to publication](#)

Disclaimer

This document contains a student thesis (bachelor's or master's), as authored by a student at Eindhoven University of Technology. Student theses are made available in the TU/e repository upon obtaining the required degree. The grade received is not published on the document as presented in the repository. The required complexity or quality of research of student theses may vary by program, and the required minimum study period may vary in duration.

General rights

Copyright and moral rights for the publications made accessible in the public portal are retained by the authors and/or other copyright owners and it is a condition of accessing publications that users recognise and abide by the legal requirements associated with these rights.

- Users may download and print one copy of any publication from the public portal for the purpose of private study or research.
- You may not further distribute the material or use it for any profit-making activity or commercial gain



Department of Applied Physics
Fluids and Flows group

Turbulence in the merging wakes of a honeycomb and two side channels

60 EC Graduation Project

C. Koster, 1228159

Public

Members of Thesis Committee:

Dr.ir. J.C.H. Zeegers (Supervisor, F&F)
Prof.dr. J.G.M. Kuerten (Mech. Eng.)
Dr.ir. L.P.J. Kamp (F&F)
Dr.ir. S. Nijdam (EPG)

This project was conducted in accordance with the TU/e Code of Scientific
Conduct.

Eindhoven, December 8th 2022

Abstract

Magnetic Density Separation is a novel method to separate different types of plastics from each other in order to make them recyclable. The machine separates the plastics based on density, by creating a density gradient in the fluid, in which the plastic particles are dispersed. In order to make the process of separation efficient, the fluctuations and turbulence in the flow have to be suppressed. Therefore, a honeycomb is placed at the entrance of the machine which laminates the flow, while the dispersed plastics are inserted in inlet ducts located above and below the honeycomb. Furthermore, conveyor belts can be added to remove shear near the respective walls. In this report, the effects of both the plates between the three inlet ducts and a bottom conveyor belt are investigated using 2-dimensional DNS simulations. The typical behaviour of the flow is investigated for several merged flow velocities with the belt velocity set equal to this merged velocity. Investigations of the side channel velocities showed that the optimal side channel velocities are equal to 80% of the center channel velocity. The influence of the belt velocity is also investigated. Increasing the belt velocity such that there is no shear near the belt resulted in significantly less turbulent intensity. Lastly, an addition of triangular caps to the plates is found to reduce the turbulent intensity significantly and is proposed as an addition for the experimental set-up. Using that experimental set-up, the flow emerging from Honeycomb 3 is investigated and compared to DNS. Laminar flows were found not to be fully developed, while turbulent flows were fully developed and in accordance with the DNS. Similarly, after the removal of the honeycomb, the flow emerging from the center duct is compared to DNS. The flow was found not to be fully developed, because the flow profile differed significantly with that of the DNS.

Contents

Contents	v
1 Introduction	1
2 Theory	3
2.1 Reynolds number	3
2.2 Laminar flow	3
2.2.1 Laminar channel flow	4
2.2.2 Laminar duct flow	5
2.3 Transition to turbulence	7
2.4 Turbulence	8
2.4.1 Wall bounded turbulent shear flows	9
2.4.2 Turbulence intensity	11
2.4.3 Turbulent duct flow	11
2.5 K-factor	12
2.6 Kelvin Helmholtz	13
2.7 Wake behind plate	14
3 Numerical Research	15
3.1 Numerical set-up	15
3.2 Mesh	16
3.3 Results and Discussion	18
3.3.1 Effect of Reynolds number at equal velocities in all channels	19
3.3.2 Side channel velocity effects	26
3.3.3 Influence of the velocity of the belt.	30
3.3.4 Geometry and thickness of the splitter plates	34
4 Experimental Research	37
4.1 Experimental set-up	37
4.1.1 Wind tunnel	38
4.1.2 Laser Doppler Velocimetry	39
4.2 Results and Discussion	40
4.2.1 Leakage bottom duct	40
4.2.2 Measurements with honeycomb 3.	45
4.2.3 Measurements without honeycomb	49
5 Conclusion	53
5.1 Numerical simulations	53
5.1.1 Instabilities zone	53
5.1.2 Turbulent intensity in the wake of the splitter plates	53
5.1.3 Vortex shedding	53
5.1.4 Effects of the side channel velocities	54

5.1.5	Influence of the belt	54
5.1.6	Plate thickness	54
5.2	Experiments	54
5.2.1	Leakage	54
5.2.2	Cell honeycomb velocity	55
5.2.3	Flow in center duct	55
5.3	Acknowledgements	55
	Bibliography	57
	Appendix	A1
	A Derivation equation 2.16 from equation 2.15.	A1
	B Matlab scripts	B1
B.1	Matlab script used in section 4.2	B1
B.2	Matlab scripts laminar flow	B5
B.3	Matlab script for determination leakage for different belt velocities.	B9

Chapter 1

Introduction

Plastic is a versatile material with various properties that make it applicable in all types of applications, including: packaging, transport, electronic devices, furniture. Besides all the unique properties, one of the troublesome properties of plastics is the lack of biodegradability. This becomes problematic if plastics are disposed and end up in the environment. In 2019, the total amount of plastic ever produced reached 9.5 billion metric tonnes, with an annual production rate of plastic amounting 460 million tonnes. This is more than a tonne of total produced plastic, with a yearly addition of another 50 kilos, per person alive as of today. In 2015, it was estimated that of the 8.3 billion metric tonnes produced up til then, 4.6 billion metric tonnes was discarded. Part of that discarded plastic ends up in the environment. Estimates are that about 12.6 million metric tonnes of plastic is dumped into oceans each year, resulting in an worldwide environmental disaster.[1]

In order to obtain a sustainable planet, recycling of plastics is the solution to the plastic waste problem. More plastics are recycled every year, with currently roughly 20% of the yearly produced plastic being recycled globally.[1] One of the challenges of recycling plastics in order to make it feasible, is to obtain high purity plastic waste. When separating the plastics from waste, the different types of plastics are still ending up in one waste stream.[2] As every plastic has its own composition and characteristics, the recycling of unsorted plastics without type sorting is insufficient for producing recycled plastic products. Hence, type specific sorting is necessary.[3] A promising method of separating and recycling plastics is by the use of Magnetic Density Separation (MDS). The concept of MDS is displayed in figure 1.1.

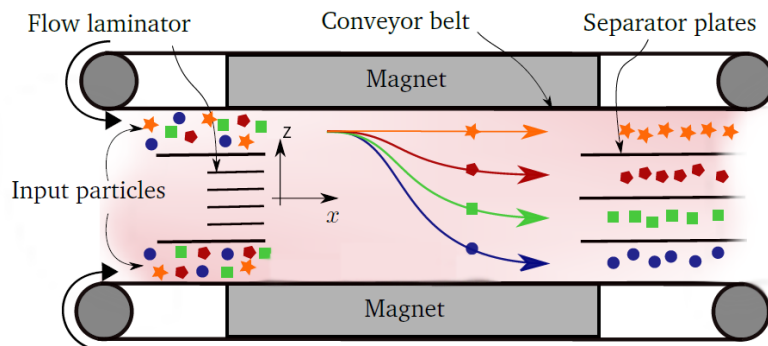


Figure 1.1: Concept of a magnetic density separation machine. Altered from Tajfirooz[4].

Plastics are shredded to small particles and flakes of the size of millimeters, and dispersed into a magnetic fluid, which flows through the MDS machine. The magnets induce a vertical density gradient in the fluid, causing the particles to float at a height corresponding to their density. By

inserting horizontal plates afterwards, the particles are sorted on their density. However, fluctuations and turbulence in the flow can cause particles to end up in the wrong separation zone, and therefore degrade the separation quality. In order to limit the flow instabilities in the magnetic zone, a flow laminator is placed upstream of the magnets, with two side channels, at the top and bottom left open where the dispersed plastic flakes enter. This laminator consists of several small square cross-section ducts separated by thin walls, and is called a honeycomb in this report. Apart from the honeycomb laminator, flow fluctuations in the set-up are prevented by the inclusion of conveyor belts at the bottom and top, that remove wall shear stress in the fluid by moving at the average flow velocity.

Different aspects of the flow in this machine have been studied at the TU/e. The aspect of flow studied during this research are the flow fluctuations, which are also expressed as turbulent intensity. For the study of the flow, a wind tunnel has been used. The effects of the magnetic forces on the flow are not investigated and are not discussed in this thesis. Within the topic of fluctuations and turbulence in the machine, in previous research, measurements were performed in the wake of the honeycomb by Thijs[5] using Particle Image Velocimetry (PIV) without side channels nor a single conveyor belt. Driessen[6] and Giesbergen[7] investigated the turbulence intensity in the wake of a honeycomb with side channels using Laser Doppler Velocimetry (LDV), where they investigated the effects of different honeycombs on the flow at various velocities. Giesbergen also investigated the effects of the side channel velocity compared to the velocity through the honeycomb. Thijs, Driessen and Giesbergen were supervised by Dellaert[8], who also conducted measurements himself on the LDV setup. The LDV setup is significantly smaller than the real MDS machine, but because a gas is used instead of the magnetic fluid, the fluid dynamics is the same because the Reynolds numbers of the real MDS and laboratory wind tunnel are similar.

After the research by Driessen and Giesbergen was finished, a conveyor belt was installed in the LDV set-up at the bottom wall of the duct. Installing another conveyor belt at the top wall of the setup was difficult and could not be realized. Van Vugt[9] performed measurements with the single conveyor belt on, and found some promising results, where the fluctuations were less at the belt than at the top wall, but an issue was found in the measurements. It appeared that more than 40% of the fluid was leaking out of the gap made for the conveyor belt in the bottom inlet duct, resulting in lower to even negative inlet velocities. Since the research by van Vugt, the gap has been closed off better, but still some leakage was expected. In order to be able to use the setup, it is necessary to determine the amount of that leakage first. Then, the bottom inlet velocity could be adapted to compensate for that leakage. As a result, the effects of the bottom conveyor belt on the merged flow in the set-up were investigated in this project.

Because the setup was not always operational during this graduation project, 2-dimensional simulations, with the domain based on the dimensions of the LDV set-up, were also used as a exploratory means to investigate the effects of the bottom conveyor belt on the merged flow in the set-up. Numerical simulations of the whole LDV setup have not been done before and is a novel type of research on the MDS. An advantage of the use of numerical simulations is how easy it is to change the dimension of the domain. This is used to investigate the effects of the dimensions of the splitter plates on the merged flow in the set-up. These plates separate the center inlet duct and the side inlet ducts from each other, and are only a few millimeters thick. Together, the combined thickness of these two plates account for over 10% of the hydraulic diameter of the height of the setup, which is very significant. The major part of this report describes in detail the numerical studies on the MDS geometry using Comsol Multiphysics software.

The report has the following structure. In chapter 2, the relevant theory to this research is discussed. In chapter 3, the numerical simulations are dealt with. This part is split in the numerical set-up, and then the results with discussion. In chapter 4, the experimental set-up used is explained, followed by discussion the results of the measurements using it. The results from chapter 3 and 4 are concluded in chapter 5.

Chapter 2

Theory

This chapter contains the theory used for this research. Firstly, the important dimensionless quantity known as the Reynolds number is introduced, which is used to predict whether a flow is laminar or turbulent. Then fully developed laminar (duct) flow is discussed, followed transition to turbulence, and fully developed turbulent (duct) flow. Lastly, vortex generation by instabilities is discussed, like the Kelvin Helmholtz instability and wakes behind bluff bodies.

2.1 Reynolds number

For flows of Newtonian fluids that do not have significant pressure changes compared to the atmospheric pressure, the governing equations are

$$\nabla \cdot \mathbf{u} = 0 \quad (2.1)$$

and

$$\frac{\partial \mathbf{u}}{\partial t} + (\mathbf{u} \cdot \nabla) \mathbf{u} = -\frac{\nabla p}{\rho} + \mathbf{g} + \nu \nabla^2 \mathbf{u}. \quad (2.2)$$

Equations 2.1 and 2.2 are called the continuity equation and Navier-Stokes equation respectively. In the case equation 2.2 is non-dimensionalized, two dimensionless parameters appear, of which one is the Reynolds number defined as

$$Re = \frac{UL}{\nu}, \quad (2.3)$$

where U is the average velocity, L is the characteristic length scale, and ν the kinematic viscosity of the fluid. The Reynolds number is the ratio of the inertial forces over the viscous forces. It predicts whether it is possible for a flow to be turbulent, or whether the turbulence gets suppressed by the viscous forces. For plane flows, often called channel flows, the height of the channel h is chosen as the characteristic length L . For flow in rectangular ducts, it is common to replace the characteristic length scale with the hydraulic diameter

$$D_h = \frac{4A}{P} = \frac{2ab}{a+b} \quad (2.4)$$

for a rectangular cross section with dimensions a times b .

2.2 Laminar flow

For this project, it is important to know what kind of flow profiles are to be expected in the honeycomb, and the side channels. First, understanding of the fully developed laminar flow profiles is relevant. Based on these profiles one can determine what the maximum velocity would

be and at which locations the velocity is very close to the maximum velocity. When a laminar flow enters a channel or duct, the walls have an effect on the flow. As a result, the velocity profile changes to fulfill the boundary conditions. This is called entry flow. The deeper the flow enters the channel or duct, the more the flow is effected by the boundary layers up until the laminar flow becomes fully developed. This also means that the y - and z -components of the velocity become zero because of equation 2.1 and the fact that the flow at the walls is zero. The length it takes for a laminar flow to become fully developed is called the entrance length. For laminar pipe flow, this length is approximately

$$L_{e,laminar} = 0.05D_h Re, \quad (2.5)$$

where $L_{e,laminar}$ is the entrance length for laminar flow.[10] For both a duct and channel, this length is assumed to be roughly the same.

2.2.1 Laminar channel flow

When a laminar channel flow, with walls at $z = 0$ and $z = h$, is fully developed, equation 2.2 becomes

$$-\frac{\partial p}{\partial x} + \mu \frac{\partial^2 u}{\partial z^2} = 0, \quad (2.6)$$

where μ is the dynamic viscosity. For stationary walls, the solution is the well-known plane Poiseuille flow

$$u(z) = -\frac{dp}{dx} \frac{1}{2\mu} z(h-z), \quad (2.7)$$

which is well known for its parabolic shape. Another well known solution is the Couette-solution. This holds in case one of the walls is moving in the x -direction, and when no pressure gradient is applied. The solution is given as

$$u(z) = \frac{h-z}{h} u_b \quad (2.8)$$

where u_b is the velocity of the wall. The velocity profiles of the plane Poiseuille and plane Couette solution are plotted in figure 2.1.

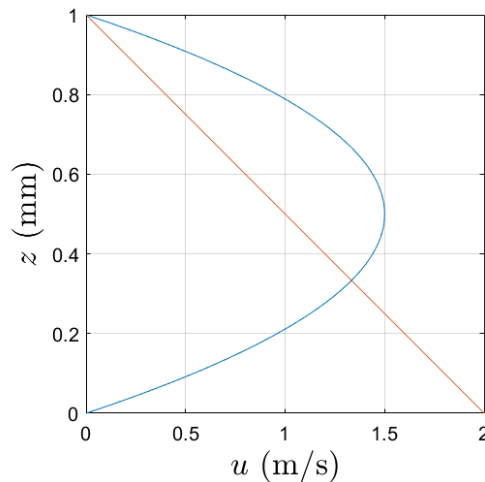


Figure 2.1: Velocity profiles of plane Poiseuille (blue) and plane Couette (red) flows, with average velocity of 1 m/s.

Note that for a plane Poiseuille flow, the maximum velocity is 1.5 times the average velocity.

This follows from

$$u_{max} = u\left(\frac{1}{2}h\right) = -\frac{dp}{dx} \frac{h^2}{8\mu} \quad (2.9)$$

$$\bar{u} = \frac{1}{h} \int_0^h u(x) dx = -\frac{dp}{dx} \frac{h^2}{12\mu} \quad (2.10)$$

$$u_{max} = \frac{3}{2} u_{avg}. \quad (2.11)$$

During this project, there is, most of the time, a combination present of both an applied pressure and a moving bottom wall. As a result, there is a mix of both types of the in figure 2.1 depicted velocity profiles present. These can be found using the same general solution of equation 2.6 by applying a fixed boundary condition at $x = h$, a moving wall boundary condition at $x = 0$ and a pressure gradient $\Delta p/\Delta x$ to generate a fixed flow. During the report, these flows are referred to as Poiseuille-Couette flows. In figure 2.2, some plane Poiseuille-Couette flows are plotted.

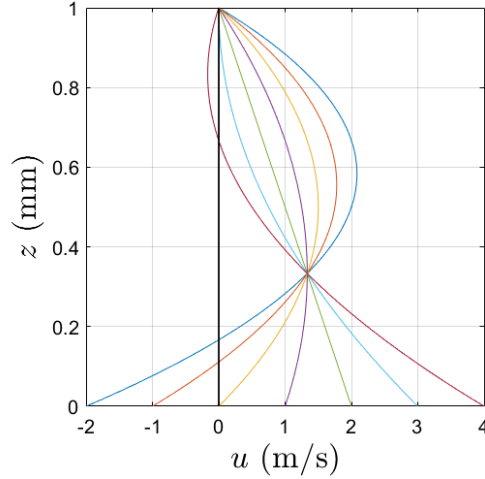


Figure 2.2: Velocity profiles of plane Poiseuille-Couette flows with various belt speed and pressure gradient under the constraint of average velocity of 1 m/s.

The velocity profiles in figure 2.2 are generated using a matlab script, which computes the profile based on the average velocity and the speed of the bottom boundary. These velocity profiles can be compared with those in simulations.

2.2.2 Laminar duct flow

For a fully developed laminar duct flow, equation 2.2 simplifies into

$$-\frac{1}{\rho} \frac{\partial p}{\partial x} + \nu \left(\frac{\partial^2 u}{\partial y^2} + \frac{\partial^2 u}{\partial z^2} \right) = 0 \quad (2.12)$$

for the x-flow direction and

$$\frac{1}{\rho} \frac{\partial p}{\partial y} = 0 \quad (2.13)$$

$$\frac{1}{\rho} \frac{\partial p}{\partial z} = 0 \quad (2.14)$$

for the y -direction and z -direction respectively. Equation 2.12 is solved for the case of fixed boundaries ($u = v = w = 0$) as

$$u_p(y, z) = -\frac{16a^2}{\pi^3 \rho} \frac{\partial p}{\partial x} \sum_{n=1,3,\dots}^{\infty} \frac{1}{n^3} (-1)^{(n-1)/2} \left(1 - \frac{\cosh n\pi z/(2a)}{\cosh n\pi b/(2a)} \right) \cos\left(\frac{n\pi y}{2a}\right) \quad (2.15)$$

for a duct with dimensions $2a \times 2b$ and center in the origin [11], see figure 2.3.

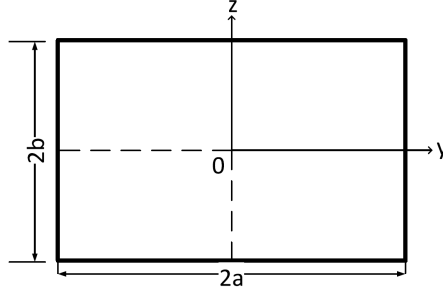


Figure 2.3: The $2a \times 2b$ duct used for the analytical Poiseuille duct flow solution. Altered from Thijs[5].

Equation 2.15 is the Poiseuille solution for the duct. During the experiments, instead of the pressure gradient, the average velocity of the flow is known, hence equation 2.15 was rewritten into

$$u_P(y, z) = u_{P,avg} \frac{\sum_{n=1,3,5,\dots}^{\infty} \frac{1}{n^3} (-1)^{(n-1)/2} \left(1 - \frac{\cosh(n\pi z/2a)}{\cosh(n\pi b/2a)} \right) \cos\left(\frac{n\pi y}{2a}\right)}{\frac{2}{\pi} \sum_{n=1,3,5,\dots}^{\infty} \frac{1}{n^4} \left(1 - \frac{2a}{n\pi b} \tanh\left(\frac{n\pi b}{2a}\right) \right)}, \quad (2.16)$$

where $u_{P,avg}$ is the mean velocity caused by the pressure gradient. The numerator of the fraction in equation 2.16 describes the profile of the flow, whereas the denominator normalizes the fraction, such that the average of the fraction is equal to one. The derivation of equation 2.16 can be found in the appendix.

In case one or more of the walls of the duct are moving, but there is no pressure applied, the solution of equation 2.12, where the moving wall is placed at $z = -b$, is

$$u_C(y, z) = \frac{4u_b}{\pi} \sum_{n=1,3,5,\dots}^{\infty} \frac{1}{n} \frac{\sinh\left(\frac{n\pi(b-z)}{2a}\right)}{\sinh\left(\frac{n\pi b}{a}\right)} \sin\left(\frac{n\pi(y+a)}{2a}\right), \quad (2.17)$$

where u_b is the velocity of the wall. Equation 2.17 is the Couette duct flow. The average velocity $u_{C,avg}$ is given by

$$u_{C,avg} = \frac{\int_{-a}^a \int_{-b}^b u_C dz dy}{4ab} = \frac{8au_b}{\pi^3 b} \sum_{n=1,3,5,\dots}^{\infty} \frac{1}{n^3} \left(\frac{1}{\tanh(n\pi b/a)} - \frac{1}{\sinh(n\pi b/a)} \right). \quad (2.18)$$

As already mentioned, a combination of a conveyor belt and a applied pressure is used during this project. Due to the linearity of equation 2.12, one can split it into two equations, because it is linear. The solution is therefore given by a linear combination of equations 2.16 and 2.17. The starting point for combining the solutions is that for the velocity and average velocity, it holds that

$$u(y, z) = u_C(y, z) + u_P(y, z) \quad (2.19)$$

and

$$U = u_{C,avg} + u_{P,avg} \quad (2.20)$$

respectively. As u_C , and thus $u_{C,avg}$, is determined when the domain and the speed of belt are defined, it is useful to express $u_{P,avg}$ as a function of the other two quantities in equation 2.20 and rewrite equation 2.19 as

$$u(y, z) = u_C(y, z) + \frac{U - u_{C,avg}}{u_{P,avg}} u_P(y, z), \quad (2.21)$$

where $u_{P,avg}$ appears in the denominator, but cancels out with the $u_{P,avg}$ in u_P , defined in equation 2.16. The advantage of equation 2.21 is that it is possible to choose any mean velocity in a certain domain, and to set up one of the walls at a certain speed in order to recreate the flow profile in Matlab. With this, for instance, it is possible to make predictions about flow profiles to be measured. An example can be seen in figure 2.4. There the average velocity and the belt are both set at 1 m/s, and the width-height ratio is 10.

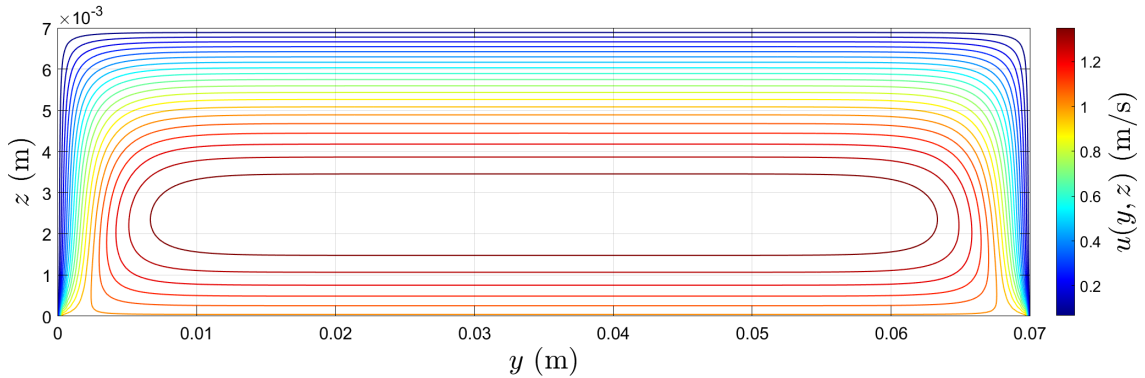


Figure 2.4: Contour of fully developed duct flow with both bottom belt and average velocity equal to 1 m/s.

In figure 2.4, the area where the velocity is very close to the maximum velocity is thin and wide. It shows the velocity at $y = 1$ cm is approximately equal at the position $y = 4$ cm. When the flow is turbulent, the profile is even more flat, as is explained in section "Turbulence". So close by the wall, the maximum can be measured and this is experimentally a great advantage as will become clear in chapter 4.

2.3 Transition to turbulence

The most common geometry investigated for transition from Poiseuille flow to turbulent flow is a circular cross section pipe. For this geometry, instabilities have been observed at about $Re = 2000$ [12], but generally it is assumed that flow in a pipe is laminar for Reynolds numbers below 2300 and turbulent for Reynolds numbers larger than 4000, with the transitional zone in between the two Reynolds numbers.[13] For square duct flow, Owolabi[14] found that the transition to turbulence starts at $Re \approx 1800$ and becomes fully turbulent at $Re \approx 3200$. Hanks et al[15] measured the critical Reynolds number Re_c , which is the Reynolds number where the transition to turbulence starts, as the function of the aspect ratio of the duct. They found that for a square duct $Re_c = 2060$. For increasing values of the aspect ratio up to about 1.6, they found that Re_c decreased to 1850. Afterwards, Re_c increased to 2300 at an aspect ratio of 4, and for increasingly larger aspect ratios, Re_c goes towards an asymptotic limit of 2800.[15] This value of 2800 is in agreement with values of $Re_c = 1350$ found by Dou et al[12] for plane Poiseuille flow, where instead of the hydraulic diameter, the height was taken as length scale. For a large aspect duct $D_h \approx 2h$.

Plane Couette flow is the most simplest case for a moving wall flow. Typically, experiments and simulations are conducted for the case of 2 walls moving in the opposite direction. For this case, plane Couette flow becomes unstable at $Re_w = 370$, where the characteristic length is taken as the channel half height and for the characteristic velocity the wall velocity is used.[12] For a square duct with 2 opposite walls moving in opposite direction with equal velocity, Klotz et al[16] found that $Re_w = 825$, where again the characteristic length is taken as the duct half height and for the characteristic velocity the wall velocity. They found for aspect ratios of 2 and 4 with the moving walls at the long side, $Re_w = 625$ and 500 respectively.[16] Looking from the perspective of 1 of the moving walls, the critical Reynolds numbers, calculated with the hydraulic diameter and the average flow in the duct with respect to that wall, for ducts with aspect ratio 1, 2 and 4 become $Re_c=1650$, 1667 and 1600 respectively. For a wider duct, Re_c goes towards 1480, as Re_c for a plane Couette flow is equal to 740, where the height is taken as the characteristic length scale. The values for the start of the transition to turbulence of a Couette duct flow can slightly differ from these values, as from the belt perspective, the side walls are also slightly moving.

For plane Poiseuille-Couette flow, the critical Reynolds number increases with a factor of more than two when the wall is moving at 10% of the maximum velocity in the channel compared to a stationary wall. When the wall moves towards 70% of the maximum Poiseuille velocity, Re_c starts to ramp up in value and becomes infinite above 70%.[17] Perturbations still can still ruin this stability, and cause turbulence to start. Furthermore, this phenomenon does not occur for Poiseuille-Couette duct flow. Instead it is believed that addition of a small Couette-component to a Poiseuille duct flow results in a slightly less stable flow with a slightly lower Re_c than the critical Reynolds number of a Poiseuille duct flow.[16]

2.4 Turbulence

Turbulent flow consists of many unpredictable fluctuations, but on a macro scale it is possible to make useful predictions. Fluctuations is not the only characteristic of turbulence. Turbulence is characterised as containing large amounts of vorticity and diffusion and energy dissipation occurs inside a turbulent flow.[13]

In order to describe turbulence, it is often useful to split the instantaneous velocity into an average velocity and a fluctuation as

$$u_i = \bar{u}_i + u'_i, \quad (2.22)$$

where the bar is the average and the prime the fluctuation. Equation 2.22 is called the Reynolds decomposition, for which the following Reynolds conditions hold

$$(i) \overline{f + g} = \bar{f} + \bar{g} \quad (2.23)$$

$$(ii) \overline{\alpha f} = \alpha \bar{f} \quad (2.24)$$

$$(iii) \overline{\frac{\partial f}{\partial s}} = \frac{\partial \bar{f}}{\partial s} \quad (2.25)$$

$$(iv) \overline{f g} = \bar{f} \bar{g}. \quad (2.26)$$

f and g are fluctuating quantities and α is a constant. Furthermore, it holds per definition that the average of the fluctuation from the average velocity is equal to 0. The average velocity can be calculated using the ensemble average defined as

$$\bar{u} = \lim_{N \rightarrow \infty} \frac{1}{N} \sum_{\alpha=1}^{\infty} u^{(\alpha)}, \quad (2.27)$$

where α is the realisation of an unique experiment.[18]

Using the Reynolds decomposition on the continuity equation results in

$$\nabla \bar{\mathbf{u}} = 0 \quad (2.28)$$

$$\nabla \mathbf{u}' = 0. \quad (2.29)$$

Applying the Reynolds decomposition on the pressure too and applying it on equation 2.2, results in

$$\frac{\partial \bar{u}_i}{\partial t} + \frac{\partial \bar{u}_i \bar{u}_j}{\partial x_j} = -\frac{1}{\rho} \frac{\partial \bar{p}}{\partial x_i} + g\delta_{i3} + \nu \frac{\partial^2 \bar{u}_i}{\partial x_j^2} - \frac{\partial \overline{u'_i u'_j}}{\partial x_j} \quad (2.30)$$

and

$$\frac{\partial u'_i}{\partial t} + \bar{u}_j \frac{\partial u'_i}{\partial x_j} + u'_j \frac{\partial \bar{u}_i}{\partial x_j} + \frac{\partial u'_i u'_j}{\partial x_j} - \frac{\partial \overline{u'_i u'_j}}{\partial x_j} = -\frac{1}{\rho} \frac{\partial p'}{\partial x_i} + g\delta_{i3} + \nu \frac{\partial^2 u'_i}{\partial x_j^2}, \quad (2.31)$$

where δ_{ij} is equal to one if $i = j$ and is otherwise equal to 0[18].

2.4.1 Wall bounded turbulent shear flows

The main source of turbulence during this project is due to the shear stress on the walls. Therefore it is important to understand these. The simplest case of a wall bounded turbulent shear flow is found in fully developed channel flow. If the stream direction is along the x-axis and the height is in the y-direction, it holds that $\partial \bar{u} / \partial x = 0$. Furthermore, after applying the continuity equation and stating that $\bar{v} = 0$ at the walls, it follows that $\bar{v} = 0$. Therefore, the x-momentum equation 2.30 changes into

$$-\frac{\partial \bar{p}}{\partial x} + \frac{\partial \bar{\tau}}{\partial y} = 0, \quad (2.32)$$

where $\bar{\tau} = \mu(\partial \bar{u} / \partial y) - \rho \bar{u} \bar{v}$ is the total average shear stress, composed of the viscous stress and Reynolds stress respectively. The y-momentum equation becomes

$$\frac{\partial}{\partial y}(\bar{p} + \rho \bar{v}^2) = 0. \quad (2.33)$$

Differentiating equation 2.33 with respect to x, shows that the pressure gradient in the x-direction is constant in the whole domain as

$$\frac{\partial^2 \bar{p}}{\partial y \partial x} = 0. \quad (2.34)$$

From this, it follows that the y-derivative of the total average stress $\bar{\tau}$ in equation 2.32 is also constant.[13]

An important parameter is the wall friction velocity u_* , which is the velocity of the fluid directly at the wall. It is defined as

$$u_* = \sqrt{\frac{\bar{\tau}(0)}{\rho}}. \quad (2.35)$$

Using the wall friction velocity, the dimensionless wall units are defined,

$$u^+ = \frac{\bar{u}}{u_*} \quad y^+ = \frac{y u_*}{\nu}, \quad (2.36)$$

which are used to match the viscous sub-layer near the wall with the rest of the flow field. This flow field is typically divided in different regions, see figure 2.5. The inner region, which is close to the wall, and the outer region, which towards the center of the flow. Within the inner region, 3 separate layers can be distinguished: closest to the wall is the viscous sublayer, then the buffer

layer and within the overlap of the inner and outer region lies the logarithmic layer[13]. A typical wall-bounded turbulent flow with these regions is depicted in figure 2.5, which is taken from Kundu [13].

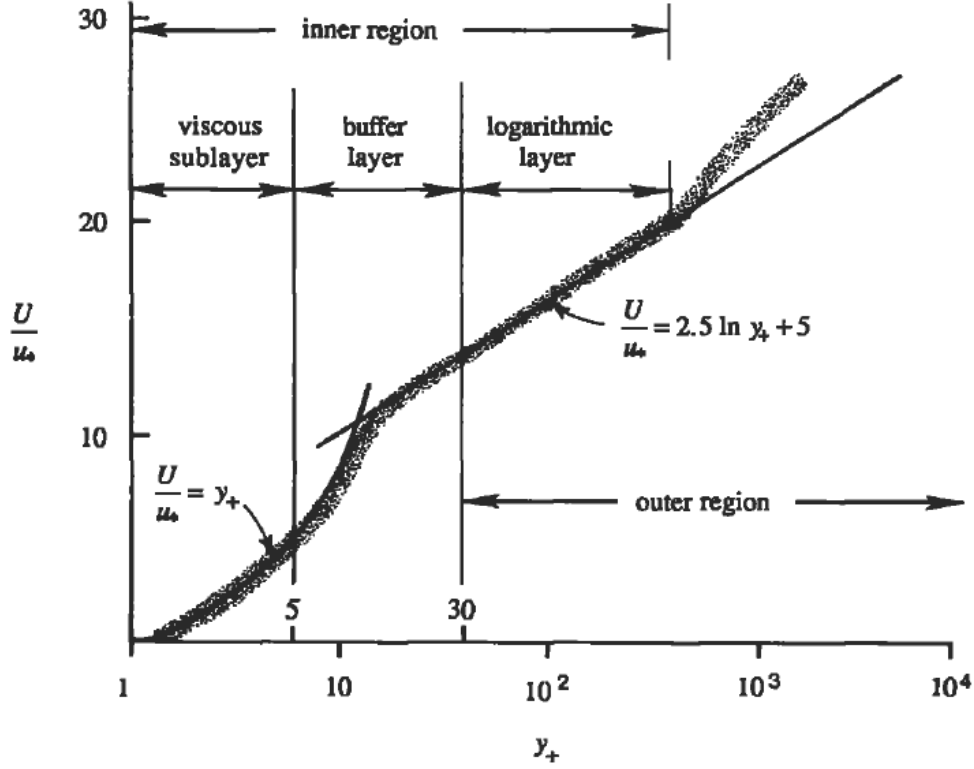


Figure 2.5: A typical profile of a wall-bounded turbulent flow in terms of wall units[13].

In the viscous sub-layer, the turbulent shear stresses are negligible as the viscosity effects dominates. Hence, the total average stress in the viscous layer is equal to $\mu(\partial\bar{u}/\partial y)$, from which, combined with equations 2.35 and 2.36, follows that in the viscous sub-layer

$$u^+ = y^+ \quad (2.37)$$

holds. Equation 2.37 holds up to $y^+ = 5$. For y^+ larger than 5, the Reynolds stresses start playing a role, meaning that that the solution of equation 2.37 no longer holds.[13]

In the outer region, the flow is characterised by eddies, the swirling of the fluid. Because of the momentum transfer by these eddies, the viscous stress is negligible compared to the Reynolds stress resulting in

$$\tau \cong \rho\overline{u'v'}. \quad (2.38)$$

Furthermore, we imply a mixing length hypothesis where

$$u' \simeq v' = \mathcal{L} \frac{\partial\bar{u}}{\partial y}, \quad (2.39)$$

where \mathcal{L} is the characteristic length of the eddies and y the distance from the wall. On the overlap of the inner and outer region, inside the logarithmic layer, the size of these eddies is limited by the wall. The length scale for the eddies is $\mathcal{L} = \kappa y$, where $\kappa \approx 0.4$ is the Von Kármán constant. Furthermore, in the proximity of the wall, the shear stress is considered roughly equal as the

shear stress at the wall.[18] As a result, from equations 2.38 and 2.39, one can derive that for the logarithmic layer

$$u_*^2 \cong \frac{\tau}{\rho} = \kappa^2 y^2 \left(\frac{\partial u}{\partial y} \right)^2 \quad (2.40)$$

holds, for which the solution is

$$u^+ = \frac{1}{\kappa} \ln y^+ + B, \quad (2.41)$$

where B is a constant with value about 4 to 5. The name of this layer originates from equation 2.41.[13] The logarithmic law starts at $y^+ = 30$ and the length of it depends on the Reynolds number[18].

In between the viscous sub-layer and the logarithmic layer, there is the so-called buffer layer ($5 < y^+ < 30$). In the buffer layer, both the viscous and the Reynolds stresses are significant, so there is no analytical solution there. [18] The buffer layer is the main source for the production of turbulence.[13]

2.4.2 Turbulence intensity

One way to characterize the amount of turbulence in the duct is the turbulence intensity. It is a local dimensionless quantity that compares the velocity variations with the average velocity of a steady turbulent flow. The turbulent intensity is commonly calculated as the individual turbulence intensity from N_T measurements of a velocity components at a certain points based on the single velocity components, and is defined as

$$I_j = \frac{\sqrt{\frac{1}{N_T} \sum_{t=1}^{N_T} (\bar{u}_j - u_j^t)^2}}{\bar{U}_\infty}, \quad (2.42)$$

where \bar{u}_j is the average velocity in the j -direction, u_j^t is the velocity in the j -direction at time step t at a fixed position and \bar{U}_∞ the velocity the average velocity in the far downstream.[8] A large value of the individual turbulent intensity indicates that there is a lot of velocity variations, hence turbulence, present in a duct, whereas a value of zero indicates no turbulence. In previous experimental work [8][6][7][5][9], instead of the individual turbulent intensity, a combined turbulent intensity was used

$$I = \sqrt{\frac{1}{D} \sum_{j=1}^D I_j}, \quad (2.43)$$

where D is the dimension of the domain (3D for the experimental set-up, 2D for the simulations).

2.4.3 Turbulent duct flow

Similar to the laminar case, the entrance length of a pipe is used to estimate the entrance length. Turbulent flow develops faster than laminar flow, because of the mixing by the eddies, resulting in a shorter entrance length than in equation 2.5. The entrance length for turbulent flow in a pipe is

$$L_{c,turbulent} = 1.359 \cdot D_h \cdot Re^{1/4}.[19] \quad (2.44)$$

The mean streamwise velocity profile in a fully developed turbulent duct flow follows the same trend as displayed in figure 2.5, when measured perpendicularly at a far enough distance from the corners. Nearer to the corner, this no longer holds, as there is less wall shear stress resulting

in a lower wall friction velocity.[20] Instead, there is secondary motion present in the yz -plane, where momentum is transported from the center of the duct towards the corners, resulting in 2 vortices in the wall region near each corner. These vortices are already clearly visible in the laminar-turbulence transition, as is seen in figure 2.6. In figure 2.6, the secondary velocity in the y - z -plane has a magnitude of order 3% of the main flow velocity in the x -direction[14].

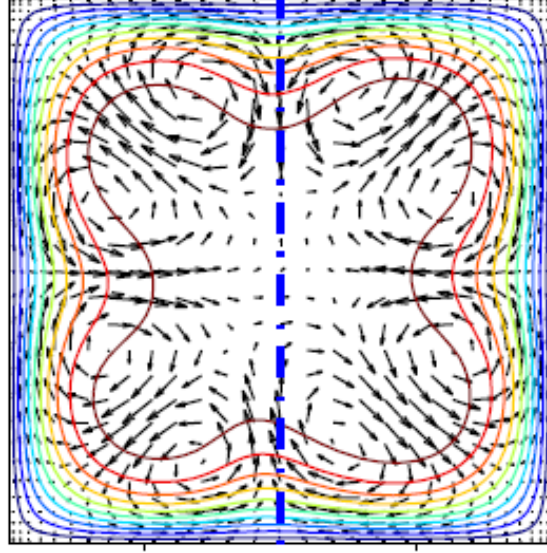


Figure 2.6: For $Re=2410$, the contour of the mean streamwise velocity and the average secondary flow indicated by arrows. [14]

For fully turbulent flows, these averaged secondary flows are also there, resulting in a slightly curvy flow profile similar to figure 2.6. Similar to a turbulent channel flow, in a turbulent duct flow, most of the turbulence generation is in the buffer layer as is also seen Owolabi[14]. Near the corners, however, there is substantially less turbulence present. Melling et al [21] found that near the diagonal bisectors, the turbulence and the velocity contours bulge towards the corner, while outside of that region they are parallel to the wall.

2.5 K-factor

With eddies being present in a more and more turbulent flow, there is more transport of momentum in the flow. Due to this additional transport of momentum from the center of the duct/channel towards the walls, the flow profile changes from a parabolic shape to a more flattened profile. As a result, the maximum velocity is lower than expected from the laminar solution. Hence, the maximum velocity provides information about the state of turbulence in a channel or duct. Plotting the ratio of the maximum velocity and average velocity would be an obvious quantity, but, as the minimum of that ratio is 1, it is much more worthwhile to use the so-called "K-factor"[6], defined by

$$K = \frac{u_{max} - \bar{U}}{\bar{U}} = \frac{u_{max}}{\bar{U}} - 1, \quad (2.45)$$

where u_{max} is the maximum velocity in a duct or channel and \bar{U} is the average velocity in a duct or channel. For a square duct, the K-factor is plotted as a function of the Reynolds number in figure 2.7 based on data from Owolabi et al.[14], Modesti[22], Zhang[23] and Kuerten[24].

In figure 2.45, for small Reynolds numbers, the K-factor is just above 1. This is in agreement with the laminar solution of a square duct in equation 2.16, from which follows that the K-

factor is equal to 1.0963 for a fully developed laminar flow. This value is also found using by direct evaluation of equation 2.12 using fourth order central finite differential schemes of second derivatives[25] on a 501x501 grid.

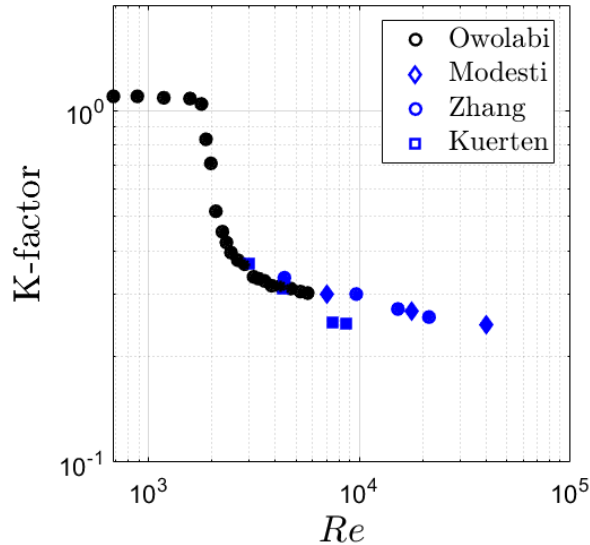


Figure 2.7: K-factor as a function of the Reynolds number in a square duct. Obtained using experimental data from Owolabi et al.[14] and DNS data from Modesti [22], Zhang[23] and Kuerten[24].

Starting at $Re = 1800$, the K-factor starts to drop in value, indicating the start of the development of turbulence. In between $Re = 2000$ and $Re = 3000$, the K-factor drops significantly to about 0.3. Afterwards, the K-factor follows the following power law downwards

$$K = 1.120 \cdot Re^{-0.155}, \quad (2.46)$$

which was found by Driessen[6], by fitting the data [14][22][23][24] with additional data from experiments and DNS of circular cross section pipe flow.

2.6 Kelvin Helmholtz

When two flows fluid layers move parallel to each other, it is possible for instabilities to occur if either there is a density difference or a velocity difference between the layers. For both cases, the instability is named after Kelvin Helmholtz.[13] During this research, only velocity induced instabilities occur as there is only one incompressible fluid used. It turns out that in that case, the flow is always unstable. [13] The instability results in rolling motion at the interface between the layers, as is shown in figure 2.8.

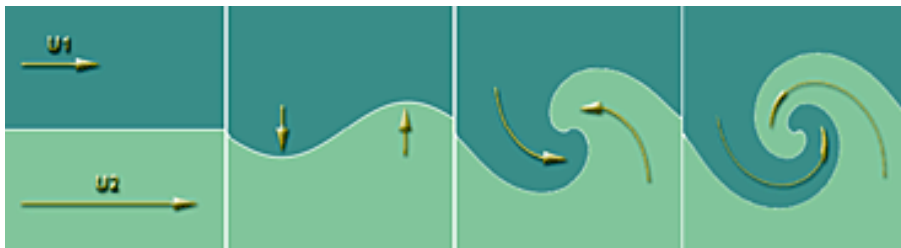


Figure 2.8: Velocity induced Kelvin Helmholtz instability.[26]

2.7 Wake behind plate

When a fluid flows past an object, it can cause oscillations in its wake. The most famous example is of flow past a cylinder. When taking the diameter of the cylinder as the characteristic length scale, there are already oscillations behind the cylinder at $Re=30$, which amplify the more the Reynolds numbers increases[27]. One way to quantify the oscillations is by using the Strouhal number

$$St = \frac{fL}{U}, \quad (2.47)$$

where f is the frequency of the oscillations. For wakes of a cylinder, the Strouhal number is typically at about 0.167.[13]

Instead of cylinders, the main objects in this research are the separation plates between the different channels, and the small plates in the honeycomb. For a very thin plate, the flow is laminar, before it starts to oscillate and eventually starts to form vortices in an alternating pattern. This results in a Kármán Vortex Street.[27] For a thick plate, there is more of a wake behind the plate. From the trailing edge, vortex shedding erupts, for which the Strouhal number has a value of just below 0.2.[28] This is in agreement with values of the Strouhal number found by Dellaert[8], where he measured Strouhal numbers of about 0.175 for large Reynolds numbers.

Chapter 3

Numerical Research

The numerical part is done using the Comsol model Laminar Flow. It has been decided to use 2-dimensional simulations of channel flow in the xz -plane. The reason is that the simulations are used as a means to understand the results from the experimental set-up better, and it is far less computationally extensive to perform than a 3-D computation of duct flow.

3.1 Numerical set-up

The set-up used for the simulations is derived from the measurements on the geometry in Van Vugt [9]. The schematic of the 2d simulations is depicted in figure 3.1.

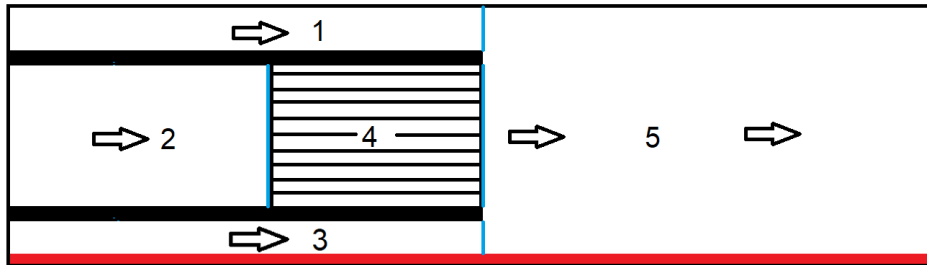


Figure 3.1: Cross-section of the set-up used for the simulations: 1 and 3 are the side channels, 2 is the center channel with optional a honeycomb (4) placed in it, 5 is the channel where the flows merge. At the bottom of channels 3 and 5, a conveyor belt is placed that moves in the same direction as the flow. In between the separate channels, plates are placed. Altered from Van Vugt [9].

The inlets on the left hand side of channels 1 and 2 have been set up as fully developed plane Poiseuille flows, whereas the inlet on the left hand side of channel 3 is a fully developed plane Poiseuille-Couette flow. The length of the channels are determined such that there is no vertical component of the pressure gradient, caused by the vortex shedding, present at the inlets. This is done such that the flow entering domain 5 is closest to physical reality. With a honeycomb, the upstream pressure effects reach significantly less far, so the length of the inlet channels are reduced to reduce computation time. Furthermore, due to the thickness of the belt, channel 3 is 7 mm in height, whereas channel 1 is 10 mm in height. The dimensions are shown in table 3.1,

The height of channel 5 is more than channels 1, 2 and 3 combined, so therefore the average velocity in channel 5 is lower than the average velocity of channels 1, 2 and 3. From table 3.1, the ratio of total height of the channels is $77/67$. Because one of the parameters used for the analysis of the merged flow uses the average velocity far downstream, the average velocity in channel 5 is

Table 3.1: Dimensions of the channels shown in figure 3.1.

Section	Height (mm)	Length (m) (no honeycomb)	Length (m) (with honeycomb)
1	10	0.3	0.1
2	50	0.3	-
3	7	0.3	0.1
4	50	-	0.1
5	77	0.6	0.6
Plates	5	0.3	0.1
Belt	3	0.9	0.7

deemed most important, hence the velocity in the other channels is multiplied with the aforementioned factor of $77/67$ for all settings.

Because it is of interest to investigate the steady turbulence, the flow state in the simulations needs to reach a steady state. For this purpose, it is checked whether the energy and enstrophy have become steady at the end of the simulation. If not, the simulation time is extended until these quantities are steady. The starting condition of each simulation is that the fluid has zero velocity. If the simulation starts with the inlet velocity and belt at the desired velocity, a shock wave appeared, causing an overshoot of the amount of unsteadiness in the domain. This unsteadiness dampens out over time as the flow becomes more steady. In order to limit computation time, it was decided to slowly ramp up the inlet velocities and belt over the first half a second using a smoothed step function in Comsol. As a result, the shock wave is reduced, causing the amount of fluctuations appearing at the start to be closer to the steady state fluctuations.

3.2 Mesh

The mesh convergence study was done before it was found that the unsteadiness and vortex generation had effects on the flow profile in the center channel, so it was done with a slightly different geometry. The changes with respect to the dimensions in table 3.1 are the length of the channels 1,2 and 3 being 0.03 m and the length of channel 5 being 0.17 m. Furthermore, the inlets were set up as developed flow condition in Comsol. One of the meshes checked is displayed in figure 3.2.

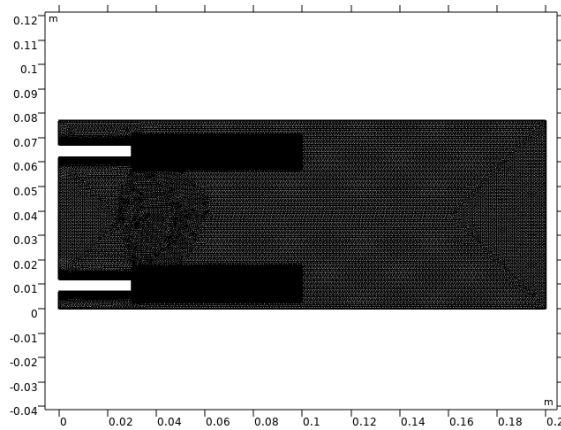


Figure 3.2: Extra fine mesh used for the mesh check, with locally extra refinements close behind the plates.

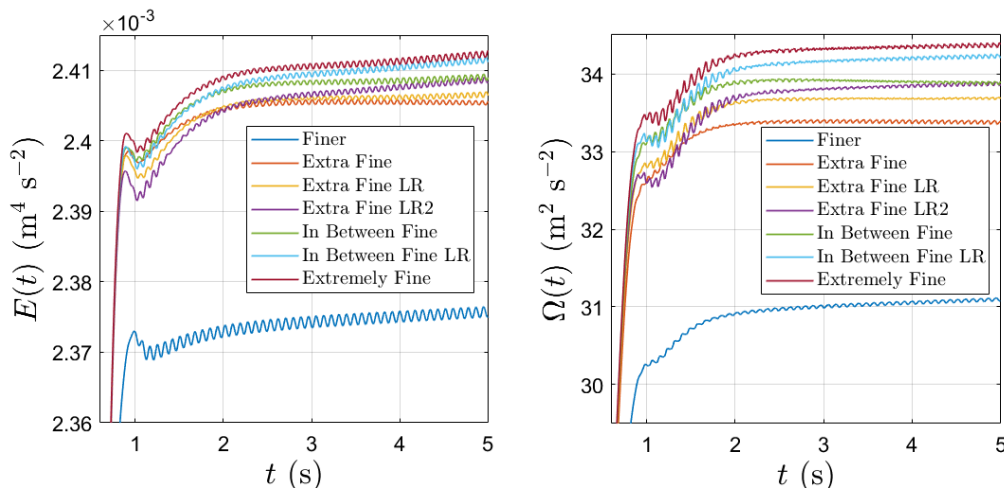
When inspecting the mesh in figure 3.2, one notices that direct behind the plates there are 2 rectangles where the mesh is more refined. These local refinements of the mesh are used to limit the simulation time, while improving the modeling of the instability. It is simulated in Comsol using the option 'refine', using either 1 or 2 refinements locally at the rectangles.

For the convergence, 4 different mesh sizes are used, of which 3 are preset in Comsol: "Finer", "Extra Fine" and "Extremely Fine". Because the elements size is of a factor 4 between the different refinements, the "In Between Fine" refinement is introduced, which has element sizes of about a factor 2 smaller than "Extra Fine" and a factor 2 larger than "Extremely Fine". The mesh statistics of these meshes are installed in a table 3.2, for which the computation times are displayed for the case a velocity of half a meter per second is run in the simulations. The local refinements are displayed in table 3.2 as "LR", where the 1x or 2x means the number of refinements setting used in COMSOL. The mesh statistics displayed in table 3.2, are the number of elements the mesh is built up with and the mesh vertices. The first one counts all the triangles, rectangles, etc, in the mesh, whereas the latter counts the number of points where the corners of these elements are.

Table 3.2: Statistics and computation times of the mesh used for $U=0.5$ m/s.

Mesh	Local Refinements	Mesh Vertices	Number of Elements	Computation time
Finer		5641	9590	8 min 54s
Extra Fine		22191	41026	1 h 4 min
Extra Fine	1x	31226	58415	1 h 28 min
Extra Fine	2x	67838	128974	5 h 48 min
In Between Fine		38227	71990	2 h 55 min
In Between Fine	1x	54129	102848	3 h 21 min
Extremely Fine		77979	149527	>6 h

For all the meshes of table 3.2, the area integrated energy and enstrophy are plotted as a function of time.



(a) Area integral of the energy as a function of time for the meshes in table 3.2.

(b) Area integral of the enstrophy as a function of time for the meshes in table 3.2.

Figure 3.3

Figure 3.3 shows that the flow using the "Finer" mesh has a significantly different energy and enstrophy level. As a result of that, the "Finer" mesh is not considered good enough for the

simulations. Furthermore, looking at runs of the "Extra Fine", "In Between Fine" and "Extremely Fine" meshes without the local refinements, one can see that the "In Between Fine" mesh is in the middle of the "Extra Fine" and the "Extremely Fine" meshes.

However, one local refinement, namely "In Between Fine LR" (light blue), causes the mesh to behave very closely to the "Extremely Fine" mesh. Considering that it only took half an hour more simulation time on a 3 hour simulation according to table 3.2, the addition of a local refinement proved to be worthwhile in this case. For the extra fine mesh, a local refinement (yellow) barely has any effect on the energy in figure 3.3a. Two local refinements are not worthwhile to use, because the simulation time drastically increases as seen with the "Extra Fine" mesh, but when looking at figure 3.3, the energy and enstrophy of that mesh is very similar of the "In Between Fine" mesh without refinements, which only has half of the simulation time. Hence, it is concluded that adding higher order refinements is not worth it.

Based on the convergence for the energy and enstrophy, it was chosen to use the "In Between Fine LR". The computation time of it is not extremely long, but it still gives very good results compared to the more rough meshes. Furthermore, the mesh performs almost as good as a refinement more, which takes twice as long to compute. The extra fine mesh with a local refinement would have been a good alternative if there was more of a time constraint for this project.

3.3 Results and Discussion

This section contains the results of the simulations. Figure 3.4 displays an impression of a typical moving belt simulation. This simulation had a merged flow velocity of one meter per second, and also the bottom wall moved at that velocity. The Reynolds number of the merged flow is therefore equal to 5106. The three inlets are fully developed Poiseuille(-Couette) flows and have an average velocity of 1.15 m/s, which is equal to $77/67$. Furthermore, a second gas, with the exact properties of nitrogen gas, is included in order to display the mixing of the fluids of the three channels. In figure 3.4, the molar fraction x_i of 1 of the 2 nitrogen gasses is displayed.

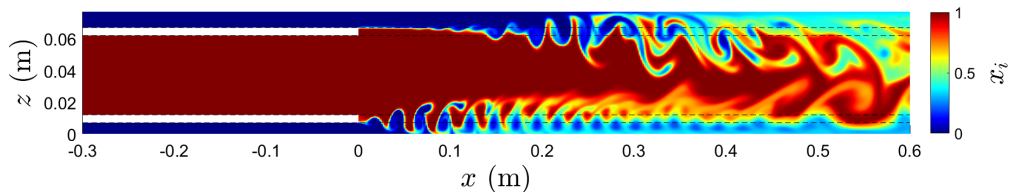


Figure 3.4: Mixing of the fluids after merging for $Re=5106$.

In figure 3.4, the effects of the instabilities behind the plate become immediately apparent; the interface between the fluid layers start oscillating, until they break up completely, especially at the top plate. As a result, near the end of the domain most of fluid coming from the top channel have mixed with the fluid coming from middle channel. At the bottom channel this is not the case. The vortex shedding behind the plates starts at different x-locations. Whereas for the bottom plate the vortex shedding occurs almost directly behind the plate, for the top channel it is after roughly 0.1 m downstream.

These observations suggest that both the plates and the conveyor belt have a significant influence on the flow. In order to investigate and possibly optimize these effects, the following things have been done. In the first subsection, the belt and the merged flow velocity have been varied simultaneously from 0.2 m/s up until 2.0 m/s. In the second subsection, for specific values of the center channel velocity, the side channel velocities have been adjusted. The belt velocity is kept the same as the merged channel velocity during these simulations. After that, in the next subsection, the side channels velocities are set equal again compared to the center channel velocity, and

instead influences of the belt are investigated. This is done for the case both walls are stationary, both walls are moving, and the case that the bottom wall moves at 1.5 times the merged flow velocity. After that, the influence of the plate thickness is investigated, and also the shape of the edge of the plate. Lastly, additional plates have been placed in the center channel to mimic the honeycomb in order to see the influence of the honeycomb on the results and to compare it with past results obtained by Driessen[6] and Giesbergen[7].

3.3.1 Effect of Reynolds number at equal velocities in all channels

In this subsection the velocities between each channel are kept the same. Furthermore, the belt has been set at a equal velocity as the merged flow. The velocities are displayed in the form of Reynolds numbers, for which the length scale is chosen to be the diameter of the channel of the merged flow.

An example of an plot of the turbulent intensity is depicted in figure 3.5 for the case $Re = 5106$.

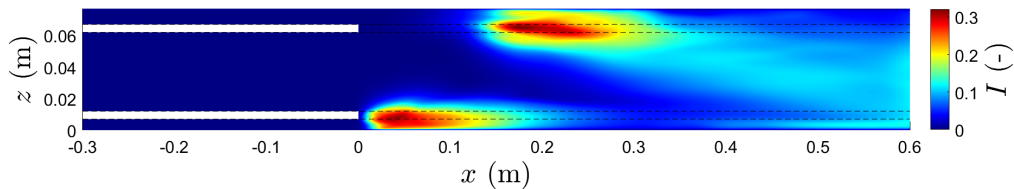


Figure 3.5: Turbulent intensity for $Re=5106$, $\bar{U}_\infty = 1$ m/s

Figure 3.5 shows that the turbulent intensity zone appears at roughly the same height as the plates, and dampens out after 20 cm. However, there are 2 main differences between the situations behind the top and bottom plate. First, the fluctuations start immediately behind the bottom plate, whereas the turbulent intensity zone at the top plate occurs further downstream in the wake. Secondly, the fluctuations behind the bottom plate do not seem to influence the center flow. Comparing figure 3.5 with the mixing displayed in figure 3.4, the locations of the start of the instability correspond with the locations of large magnitude of turbulent intensity. So it is clear that vortex shedding is responsible for the large fluctuations generating the turbulent intensity maxima.

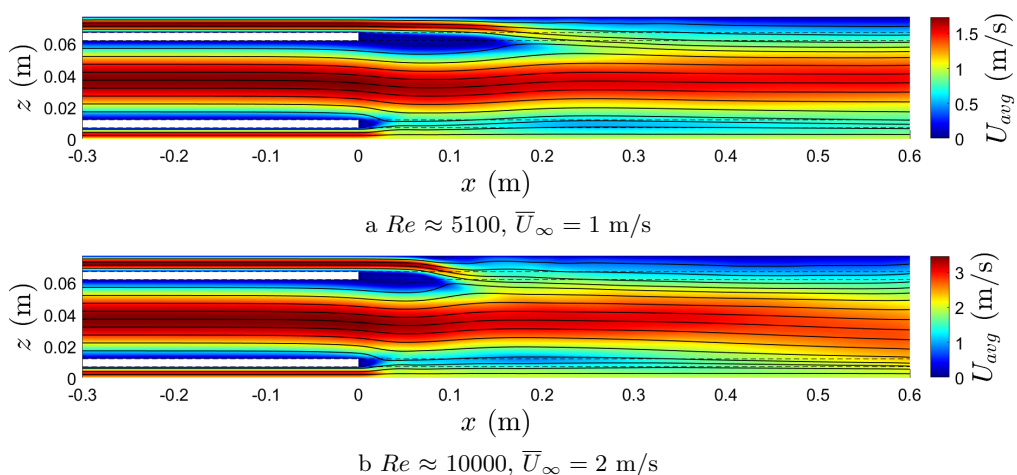


Figure 3.6: Magnitude of the average velocity with streamlines of the average velocity for (a) $Re=5106$ and (b) $Re=10112$.

The asymmetric starting position of the vortex shedding seems to be correlated with the mean

flow bending downwards and back upwards again as seen in figure 3.6. This downwards bending of the flow is already visible near the end of the center channel. For a larger velocity, the bending of the flow back upwards occurs significantly quicker and therefore the merging of the flows from channels 1 and 2 occur closer to the top plate. Furthermore, near the end of the domain, there is also a significant difference between the flows: for $Re \approx 5100$ the streamlines are in the horizontal direction, whereas for $Re \approx 10000$, a small angle of the streamlines towards the belt is observed.

In order to quantify the average vertical velocity component inside the the inlet channels better, these profiles are plotted at different x-locations inside the inlets in figure 3.7.

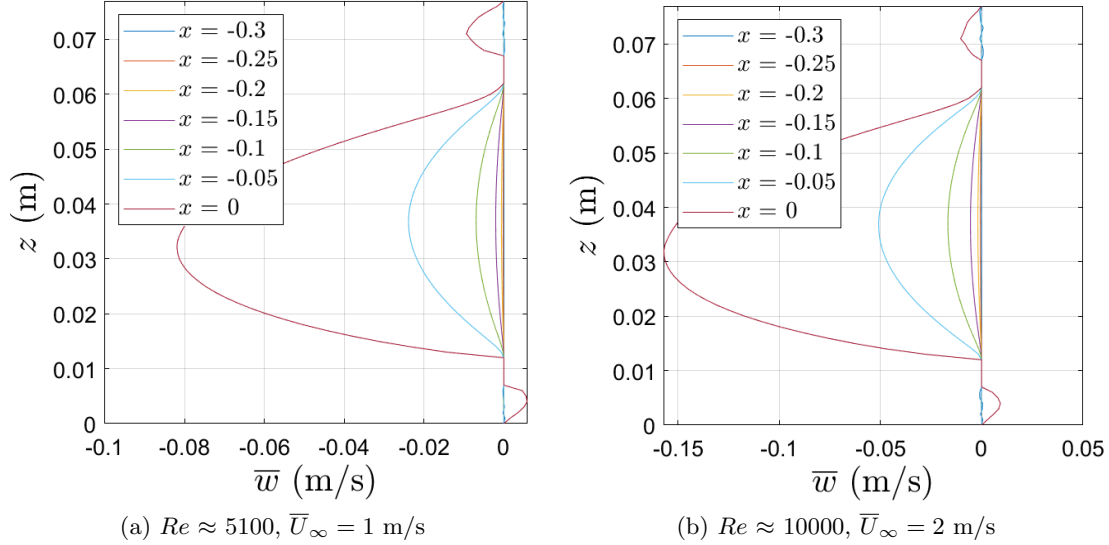


Figure 3.7: Average vertical velocity inside channels 1, 2 & 3 for (a) $Re=5106$, $\bar{U}_\infty = 1$ m/s and (b) $Re=10112$, $\bar{U}_\infty = 2$ m/s.

Figure 3.7a shows that when the inlet velocity is 1.15 ($=77/67$) m/s, the downwards velocity component starts to develop at a depth of roughly -15 cm. At about 5 cm upstream of the end of the plates, the vertical velocity component is 0.02 m/s, which corresponds to a downward angle of about -1° . At the end of the plates, the angle with respect to the horizontal line even increases to about -4° . For a twice as large inlet velocity, the vertical velocity component is also twice as large as is seen in figure 3.7.

For different Reynolds numbers of the merged flow, color plots of the turbulent intensity, defined by equation 2.43 are made. For the simulations with Reynolds numbers below 2300, the magnitude of the root mean square of the velocity components were of the order of 10^{-3} and no vortex shedding was observed.

Figure 3.8 shows that for Reynolds numbers just above 2500, there is only significant turbulent intensity present directly behind the bottom plate. These fluctuations decay to zero within twenty centimeters after its first appearance. Behind the top plate, the start of the turbulent intensity is a bit further downstream compared to the bottom plate, and is considerably less at the 'lower' Reynolds numbers. However, somewhere between $Re \approx 4100$ and $Re \approx 5100$, the turbulent intensity behind the top plate becomes larger than at the bottom plate. Furthermore, a tail is observable, that diffuses slightly downwards, and for even larger Reynolds numbers, seem to cause significant turbulent intensity at the end of the domain by interacting with the flow field there. These fluctuations at the end of the domain most likely cause the average flow bending downwards at the end in figure 3.6b.

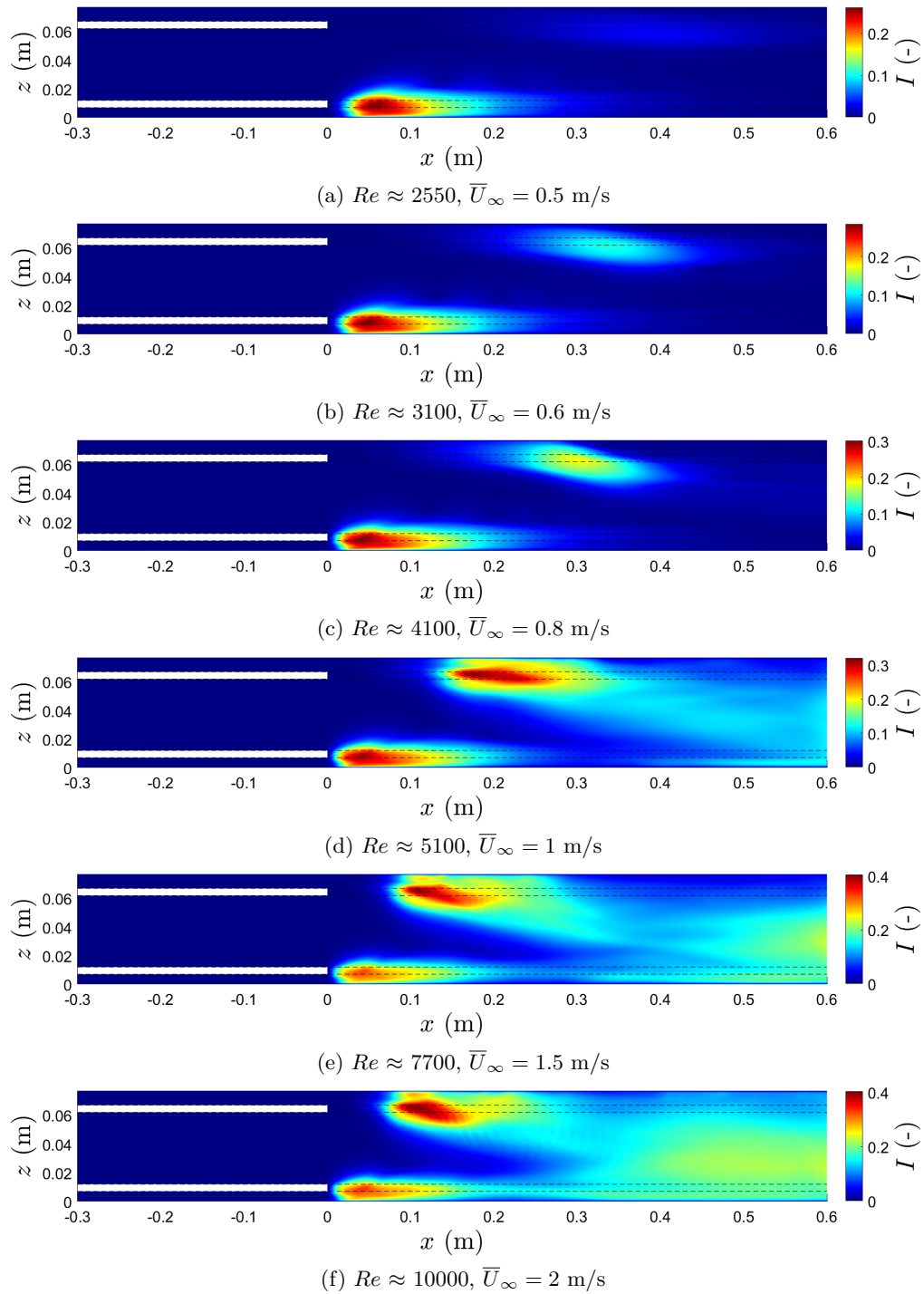


Figure 3.8: Turbulent intensity for different Reynolds numbers.

In figure 3.9, the maximum turbulent intensity behind both plates is plotted as a function of the Reynolds number of the merged flow. For finding the maximum turbulent intensity points, a scan routine was used in both the upper half and lower half of the domain. For the bottom plate, the maximum turbulent intensity slowly converges to a value just below 0.35, after its initial

appearance. For the top plate, the turbulent intensity initially rises slower than at the bottom plate, but the maximum turbulent intensity becomes larger for Reynolds numbers above 5000 than the maximum at the bottom plate and above 6000, the intensity saturates at a value of 0.41.

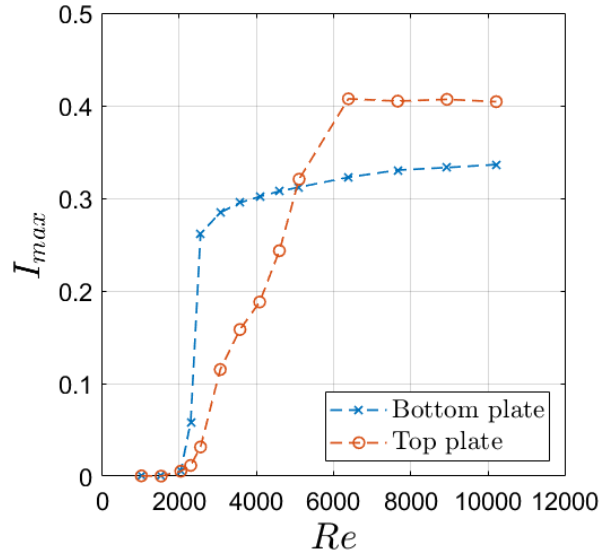


Figure 3.9: Maximum value of turbulent intensity behind both plates versus the Reynolds number.

Similarly to the maximum turbulent intensity, the distance between the maximum turbulent intensity and the plates is plotted as a function of the Reynolds number, as it was found that the maximum turbulent intensity is very close to where the start of the turbulent intensity, and thus the instability, behind the plate is. Hence, plotting the location of the maximum turbulent intensity gives info on where the instability starts.

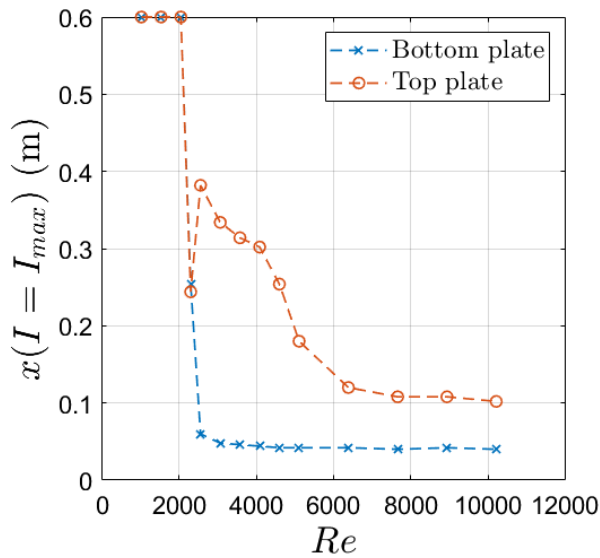


Figure 3.10: Location of the maximum intensity behind the plates versus the Reynolds number.

In figure 3.10, the data points where the x-coordinate of the maximum turbulent intensity is

equal to 0.6, are fully laminar solutions where the maximum turbulent intensity is of order 10^{-3} . For the bottom plate, the instability occurs almost instantly behind the plate, and remains at the same distance, 40 mm, from the plate. On the contrary, for the top plate, the initial instability occurs further downstream of the plate, and moves closer to the plate for larger Reynolds numbers up until it is 100 mm from the plate for Reynolds numbers larger than 10000. The behaviour of the location of the maximum intensity moving closer to the plates for increasing Reynolds numbers was also observed during measurements behind the honeycomb by Driessen[6] and Giesbergen[7].

The turbulent intensity at the end of the domain is also of interest, because fluctuations later on the duct can still ruin the separation of plastics. For this purpose, in figure 3.11, the turbulent intensity is averaged over the last five centimeters of the domain, and plotted as a function of the height.

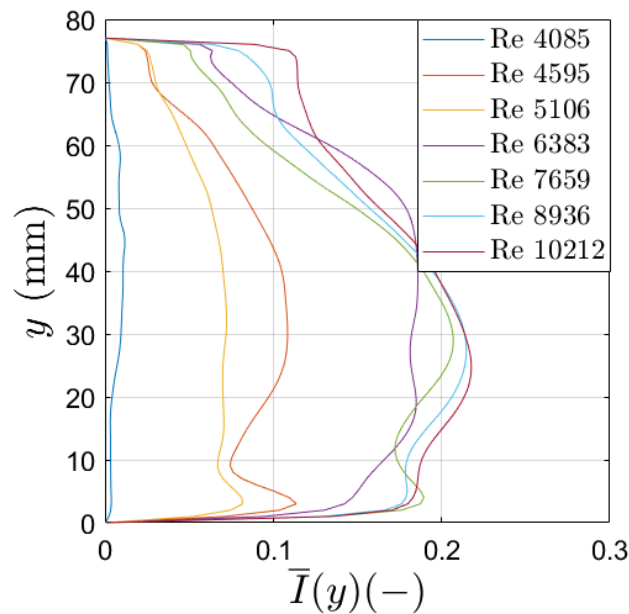


Figure 3.11: Turbulent intensity, averaged from $x=0.55$ m to $x=0.6$ m, versus the height for different Reynolds numbers.

In figure 3.11, one notices that the bulk of the turbulent intensity is mainly present in the bottom half of the domain. The reason for this observation is the vortices that are shed at the trailing edge of the top plate move downwards and disturb the flow field in the bottom half. Furthermore, the turbulent intensity is slightly larger for larger Reynolds numbers. Especially at the top wall, the turbulent intensity is increasing for larger Reynolds numbers. For the center zone of the channel, there is not much difference in turbulent intensity for Reynolds numbers above 7000.

In order to study the effects in the wake of the splitter plates with the presence of a wall near one of the plates, it was decided to investigate the frequencies of the vortex shedding at the trailing edge of the plates. For this purpose, data of the time evolution of the pressure was exported at certain points in the domain, and a Fast Fourier Transform applied to that data in order to determine the frequencies. It was found experimentally that the optimal place to determine the frequency of the vortex shedding is at the maximum turbulent intensity. The frequencies found are converted into the Strouhal number, for which the characteristic length scale that is used is the plate thickness. The Strouhal number is then plotted as a function of the Reynolds number Re_T , where the T denotes that the plate thickness is used as the characteristic length scale. Figure 3.12 shows that for increasing wall Reynolds numbers, the Strouhal number converges to a value

just below 0.166. This is close to Strouhal numbers obtained from earlier experimental work by Dellaert[8], who found the Strouhal number to be close to 0.175 for $Re_T > 200$.

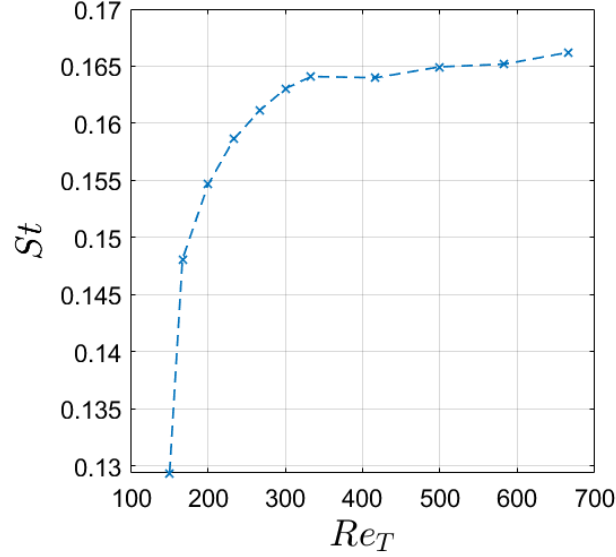


Figure 3.12: Strouhal number as function of the Reynolds number for the bottom plate.

Whereas there is only one distinct peak in the frequency of the oscillations at the bottom plate, there are multiple present at the top plate. The hypothesis for this is that the top wall greatly influences the flow there due to the vortex generation. This phenomenon becomes more pronounced the larger the velocity becomes. For instance, at the simulation of $Re=10000$ in figure 3.13, one can see multiple frequencies of the pressure oscillations behind the top plate compared to a single frequency of the pressure oscillations measured at the bottom plate.

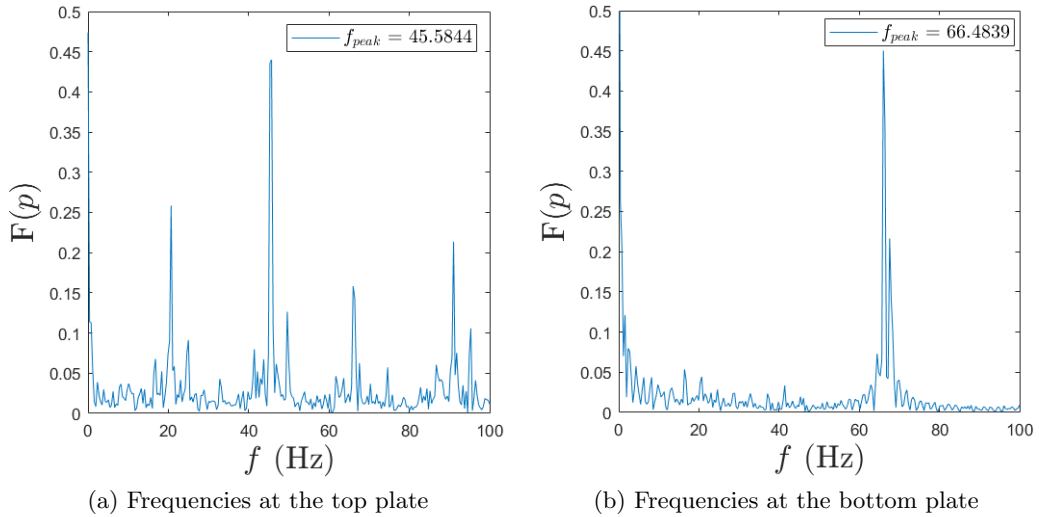


Figure 3.13: Simulation at Reynolds number 10000, or $Re_T=667$, the Fourier transform of the pressure versus the frequency for (a) behind the top plate and (b) behind the bottom plate.

In figure 3.13b, there is only one distinct peak visible, whereas in figure 3.13a, there are four distinct peaks: at 20.5 Hz, 45.5 Hz, 66.5 Hz and 91 Hz. The peak at 66.5 hertz most likely

corresponds to the vortex shedding by the plate, as it is the same frequency as the one seen at the bottom plate. The peaks at 20.5 Hz and 45.5 Hz are most likely due to the vortex generation at the wall, whereas the 91 Hz is the second harmonic of the 45.5 Hz. Looking at the amplitudes of the peaks, the 66.5 Hz peak is much lower than the 20.5 Hz and 45 Hz peaks. Because of this, one can conclude that the wall-vortex generation is dominant at the top plate. Inspection of this specific simulation by eye confirms this: in the first time elapse of the simulation, the vortex generation at the top and bottom plate look similar, but in the end phase of the simulation elapse, instabilities start to occur at the top wall, resulting in a completely different flow field than in the first time elapse. The first instability is visualized using vorticity in for the case of $Re \approx 10000$.

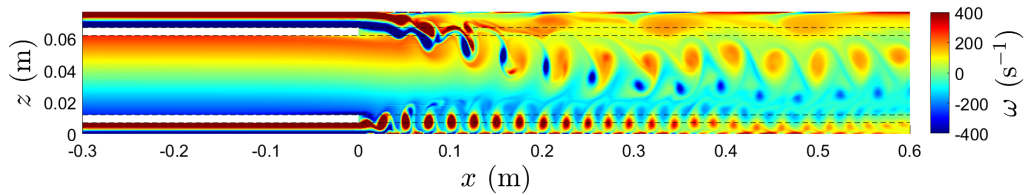


Figure 3.14: Vorticity for $Re \approx 10000$ just before the first collapse.

In figure 3.14, there is a big difference in vortex shedding behind the top and bottom plate. The vortices behind the top plate are large in size, whereas the vortices behind the bottom plate are small and occur more frequently. This seems to indicate that the frequency of vortex shedding behind the bottom plate is larger than that behind the top plate, which is not the case. Instead, the velocity of the vortices behind the bottom plate is observed to be much smaller than the vortices shed at the trailing edge of the top plate. The difference in speed can be seen in figure 3.6b. Besides the vortex generation by the plates, there are also vortices visibly rolling up at the top wall. These vortices collapse later on during the simulation, creating more chaotic motion. This results in the final situation depicted in figure 3.15.

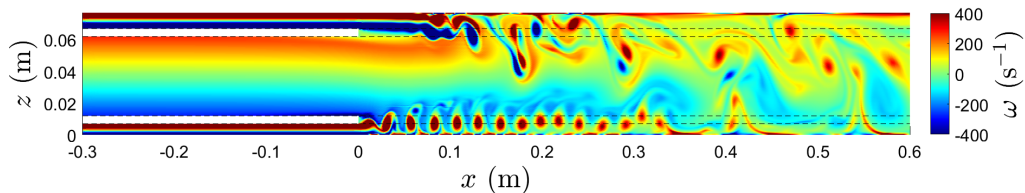


Figure 3.15: Vorticity for $Re \approx 10000$ after the second collapse.

In figure 3.15, the vortex street at the top plate, that was visible in figure 3.14, is completely unrecognisable. Instead, the vortex street is chaotic and clearly distorts the vortices at the bottom plate. The vortex street at the bottom is completely destroyed at $x=0.35$ m. This is also very close to the start of the third patch of turbulent intensity in figure 3.8f.

3.3.2 Side channel velocity effects

The effect of different side channel velocities with respect to the mean channel velocity were investigated by changing both side channel velocities in the simulations at $Re \approx 3100$, $Re \approx 5100$ and $Re \approx 10000$. These Reynolds numbers were chosen based on the three distinct differences in development of turbulent intensity in figure 3.8. The smallest Reynolds number was chosen because the turbulent intensity spots died out and the flow became stable. $Re \approx 5100$ was chosen as it was the first case where a distinct tail behind the top side turbulent intensity spot appeared. And the largest Reynolds number is chosen because it results in the most turbulent intensity in the profile. The velocity of the center channel is kept constant. Because the average merged flow velocity changes when the velocity in the side inlets change, the belt velocity is adjusted to maintain the same velocity compared to the average merged velocity.

For the simulations with $Re \approx 5100$, or $\bar{U}_\infty = 1$ m/s, both side channel velocities were varied equally from 0 to 2.3 m/s. Low velocities either made the flow field stable or very unstable as is seen in figure 3.16, where vorticity fields are plotted for side channel velocities of 0 and 0.23 m/s.

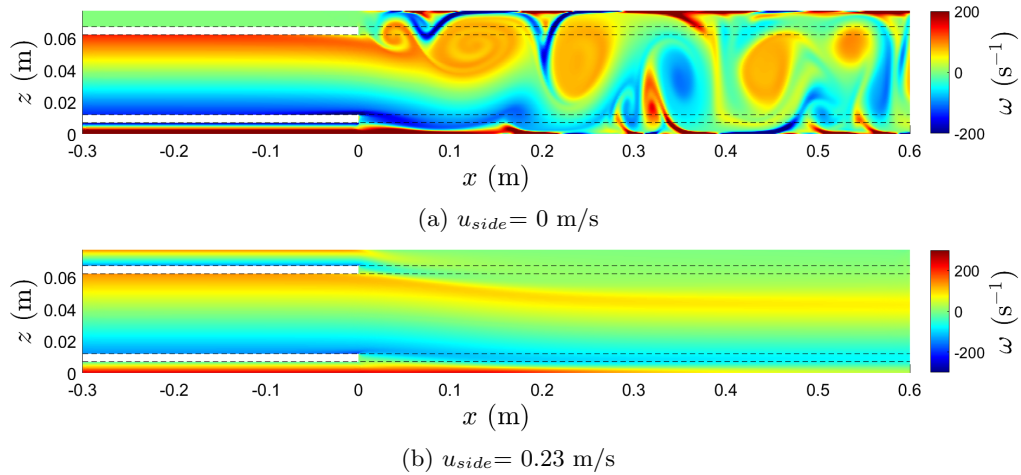


Figure 3.16: Vorticity for low side channel velocities with center channel velocity equal to 1.15 m/s.

The difference in a flow field having a zero side channel velocity with a side channel velocity of 0.23 m/s is very big as is seen in figure 3.16. For no side channel velocity, there is huge vortex generation, whereas for a small side channel velocity no instability in the domain occurs. Apparently, instabilities are very sensitive on a slight bias of the side channel velocity. An explanation for this sensitivity is the suction that is only present in the bottom channel for the simulation with zero side channel velocity.

For side channel velocities larger than the center channel velocity, it is observed that the vortex generation is at y -values closer to the center compared to equal velocity runs, as is for instance simulated for the case of a side channel velocity of 1.84 m/s in figure 3.17.

In figure 3.17, similar to the runs of equal velocity, the vortex shedding behind the bottom plate starts closer to the plate than at the top plate. Furthermore, the vortices from the top plate also move diagonally downwards to the bottom, disrupting the vortex street originating from the bottom plate and generating much turbulent intensity at the bottom.

It is of interest to know the amount of turbulent intensity in the domain. Hence, similarly as done earlier, the maximum turbulent intensity and the location of that maximum turbulent intensity is plotted in figure 3.18. On the x -axis, it is chosen to put the difference in velocity

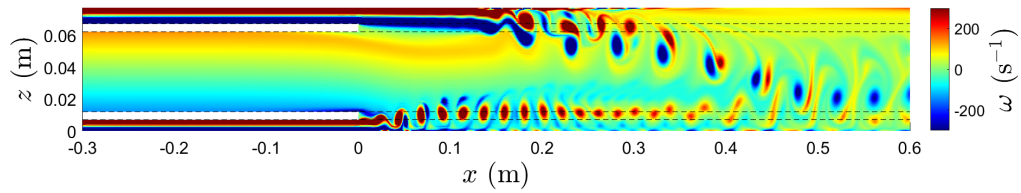


Figure 3.17: Vorticity for 1.84 m/s side channel velocity with center channel velocity equal to 1.15 m/s.

between the side channel and the center channel. A larger side channel than center channel velocity results in a positive Δu .

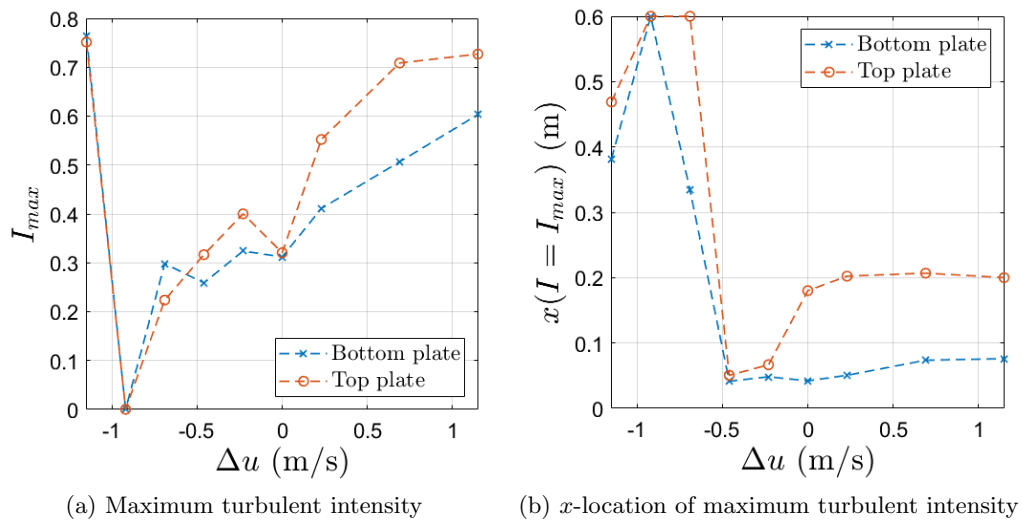


Figure 3.18: (a) The maximum turbulent intensity and (b) its respective x -location as a function of the velocity difference between the center inlet channel and side inlet channels for center inlet velocity 1.15 m/s.

Equal velocities in all inlet channels results in a less fluctuations than a small velocity difference as shown in figure 3.19a. Typically, for increasing side channel velocities, the maximum turbulent intensity also increases and vice versa for decreasing side channel velocities. However, for the bottom plate, the maximum turbulent intensity flattens out at about 0.3 for negative velocity differences. The first two points in the domain were already discussed in figure 3.16, where the suction in the bottom channel plays a major role in the destabilisation of the flow. In figure 3.18b, increasing the side channel velocities from $\Delta u=0$ m/s results in a marginally further distance of the largest fluctuations from the plates. When the side channel velocity is decreased, a jump in observed at $\Delta u=-0.23$ m/s for the top plate, as the distance of the largest fluctuations move over 10 cm closer to the plate, whereafter the location barely changes. The differences in distance of the maximum intensity behind the bottom plate, from 4 cm to 7 cm, is not as significant in comparison. The trends found in figure 3.18 are in agreement at $u_{center} = 2.3$ m/s, where the side channel velocities were varied from 1.15 to 3.45 m/s. The maximum intensity and its distance from the plates in those simulations is plotted in figure 3.19.

In figure 3.19a, the maximum turbulent intensity rises for increasing side channel velocities, where the maximum turbulent intensity behind the top plate is more sensitive to the rise in side channel velocities. In figure 3.19b, a jump occurs at $\Delta u=-0.23$ m/s. The difference of the x -location of the maximum turbulent intensity at the top plate is explained by figure 3.10, there a factor of 1.8 between Reynolds numbers of 5000 and 10000 occurs for the distance.

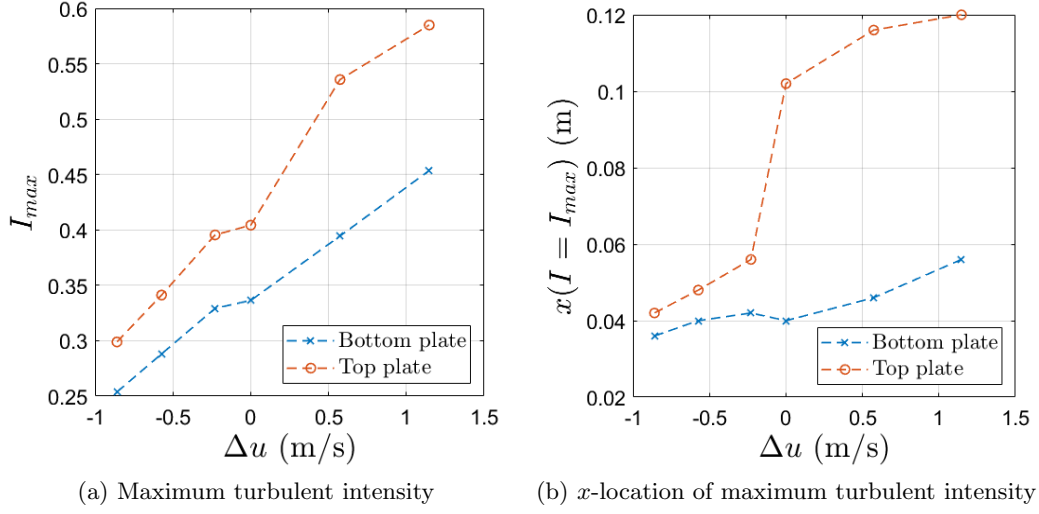


Figure 3.19: (a) The maximum turbulent intensity and (b) its respective x-location as a function of the velocity difference between the center inlet channel and side inlet channels for center inlet velocity 2.3 m/s.

Similarly, as done in the previous subsection, the turbulent intensity is averaged over the last 5 cm of the domain, and plotted over the height in figure 3.20.

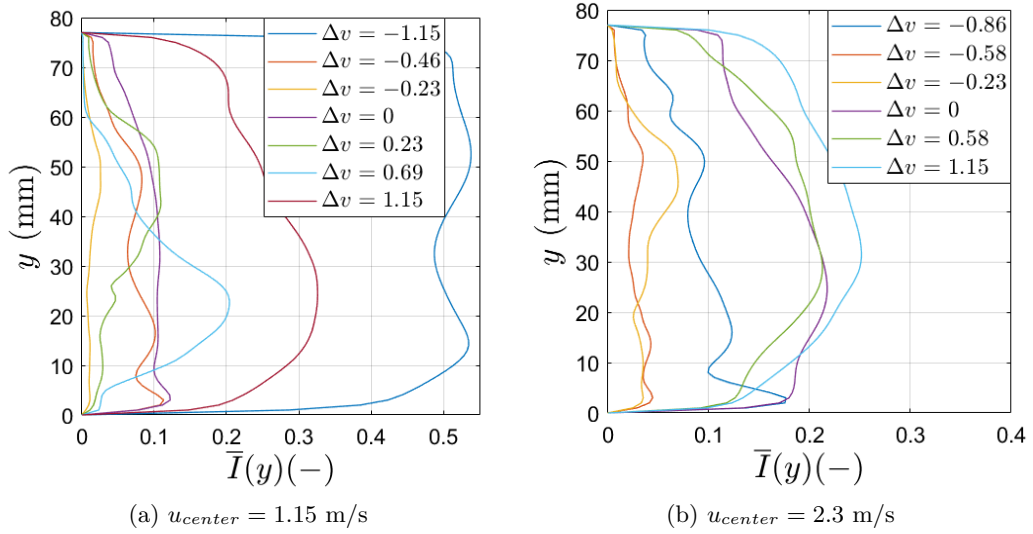


Figure 3.20: Turbulent intensity averaged over the last five centimeters of the domain versus the height for (a) $u_{center} = 1.15$ m/s and (b) $u_{center} = 2.3$ m/s.

From figure 3.20a, it immediately becomes clear that large velocity differences between the center and side channels cause significantly more fluctuations in the domain when comparing $\Delta v \pm 1.15$ m/s with $\Delta v = 0$ m/s. Also for the simulation with $\Delta v = 0.69$ m/s, there is significantly more turbulent intensity present near the belt. Simulations with $\Delta v = -0.46$ m/s and $\Delta v = \pm 0.23$ m/s have less intensity at the end of the domain than the simulation with $\Delta v = 0$ m/s, where the simulation with $\Delta v = -0.23$ m/s has the least turbulent intensity near the end of the domain. In figure 3.20b, the simulations with smaller side channel velocity than the center channel velocity are less turbulent near the end of the domain compared with the simulations with a larger side

channel velocity. The simulation with the least turbulent intensity turns out to be the one with $\Delta v = -0.58$ m/s.

Based on the results, it turns out that setting the side channel velocity at 75% to 80% of the center channel velocity results in less fluctuations, as both the peak turbulent intensity is lower, as well as the turbulent intensity leaving the domain. This is in stark contrast with results from experiments conducted by Giesbergen[7], where he found that it was optimal to set the velocity of the side channels at about 120% of the center channel velocity. Giesbergen did have a honeycomb in the center channel during his measurements. Furthermore, he did not have a moving belt at the bottom, and lastly, three-dimensional effects likely also play a role in real life experiments. Because of these differences, it is useful to verify these results experimentally in 3d.

3.3.3 Influence of the velocity of the belt.

In the experimental setup, there is a conveyor belt placed at the bottom wall, as can be seen in figure 3.1. It is of interest to know what the effect is of having a belt moving with the same velocity as the merged flow compared to a stationary wall. Hence, simulations are performed where there is no moving bottom wall. Furthermore, a belt at the top plate is added, which also moves with the same velocity as the bottom belt. Lastly, the belt at the top has been removed, and instead the bottom belt is increased to such speed that a laminar solution would have no gradient in the velocity directly at the belt.

For the simulations with stationary walls, Reynolds numbers of the merged flow equal to 5100, 7700 and 10000 are chosen. In figure 3.21, color plots of the turbulent intensities of these simulations are shown.

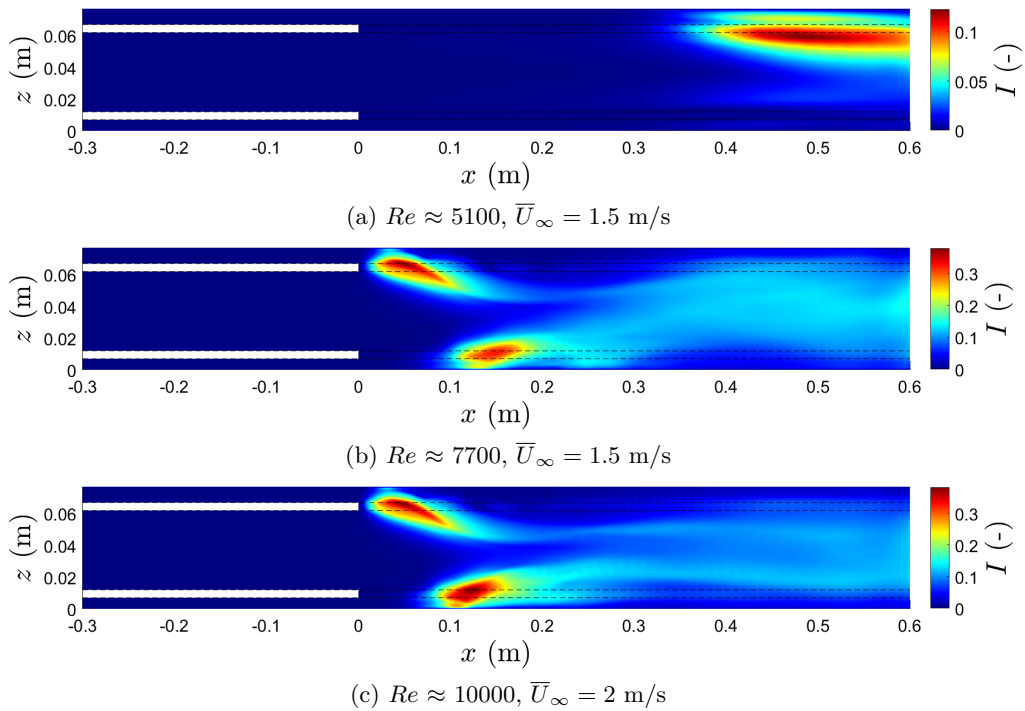


Figure 3.21: Turbulent intensity for different Reynolds numbers, with two stationary walls.

In figure 3.21, the flow becomes unstable near the end of the domain at the top, whereas at the bottom of the domain, there are no fluctuations present. An increase in velocities of the inlet channels results in the fluctuation to start close to the plate, as seen in figures 3.21b and 3.21c. Furthermore, fluctuations behind the bottom plate are also observed, albeit at a further distance compared to the fluctuations at the top. This opposes the simulation with a moving belt, where the distances of the fluctuations and the plates where reversed. The wake is larger at the top plate, because the boundary layer is larger in the top channel due to its larger height. With the belt on, the boundary layer at the top side of the bottom channel increases, which results in a larger wake. This can explain why the start of the fluctuations inverts behind the top and bottom plate when the conveyor belt is turned on or off. Comparing the location of the start of the fluctuations behind the bottom plate between figures 3.21b and 3.21c, one can see that for the larger velocities, the start of the fluctuations is closer to the plate. This is in agreement with what is found with the belt on.

Looking at the tails behind the starting spots of turbulent intensity, in figures 3.21b and 3.21c, the turbulent intensity does not fully fade away. Instead, towards the end of the domain, there is

a development of fluctuations, especially in figure 3.21b. Because of this, it is decided to plot the turbulent intensity as a function of height at every multiple of 10 centimeters.

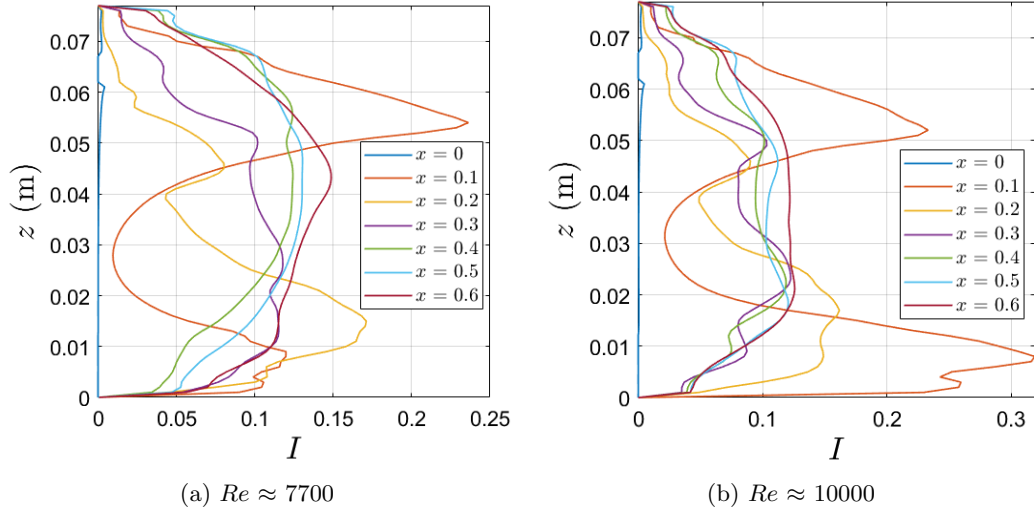


Figure 3.22: Turbulent intensity averaged over the last five centimeters of the domain versus the height for (a) $Re \approx 7700$ and (b) $Re \approx 10000$.

Initially, in figure 3.22, the big turbulent intensity spikes near the bottom and the top plate fade, while in the center of the domain the turbulent intensity is increasing. From 0.3 meters onwards, the turbulent intensity in the whole domain is slowly increasing. Because of this observation, it is decided to elongate the domain for the simulation of $Re \approx 10000$ for both with stationary and moving bottom wall in order to compare the effects far downstream. Colour plots of the turbulent intensity of both simulations are found in figure 3.23.

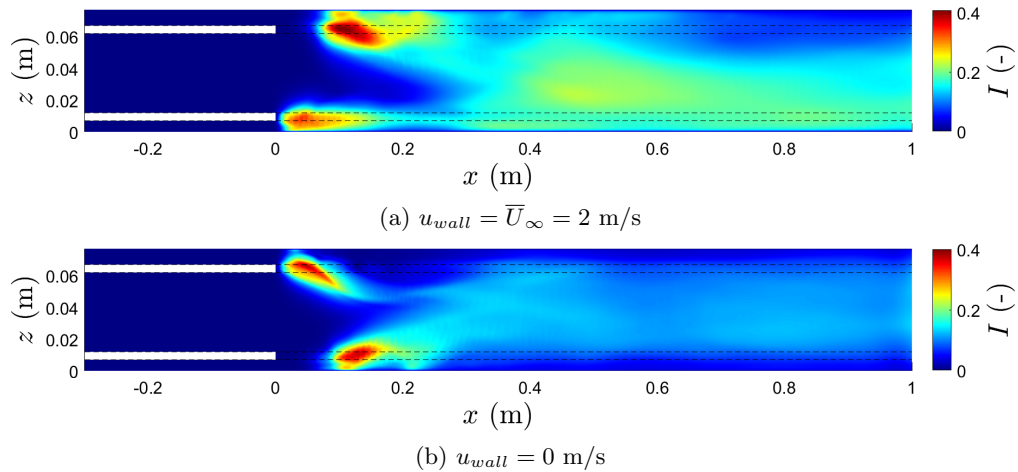


Figure 3.23: Turbulent intensity for $Re \approx 10000$, with (a) the bottom wall moving at $u_{wall} = \bar{U}_\infty = 2 \text{ m/s}$ and (b) a stationary bottom wall

In figure 3.23a, the amount of fluctuations does decrease significantly in the last 50 centimeters of the domain, but it is still considerably more than for a stationary bottom wall at one meter behind the plates, as seen in figure 3.23b. There, the turbulent intensity is steady in the last 40 cm of the domain, reaching values up to 0.11. The difference in turbulent intensity later on in the channel between the 2 cases is likely caused by the distance it takes for the flow to develop, as

seen in figure 3.24. For the simulation with stationary walls, the flow is already developed 20 cm in the duct, whereas with a moving bottom belt, the development of the flow profile takes over 70 cm.

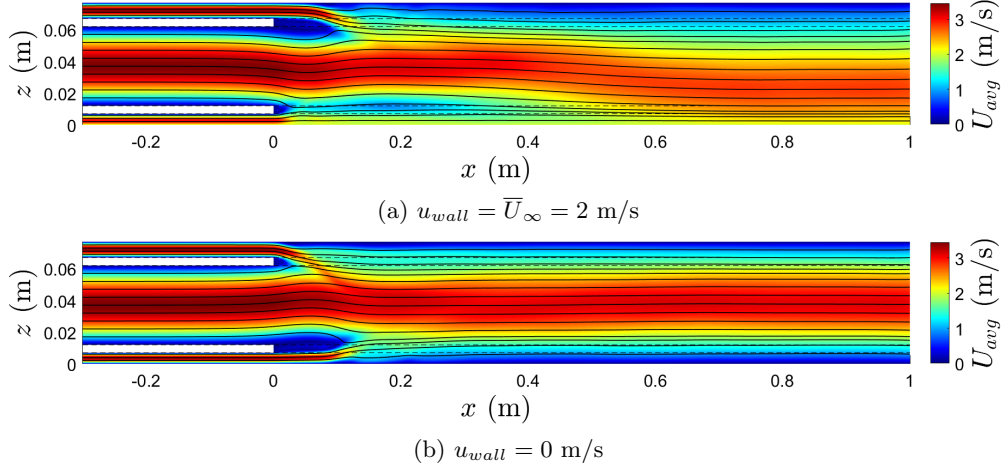


Figure 3.24: Average velocity magnitude, including streamlines, for $Re \approx 10000$, with (a) the bottom wall moving at $u_{wall} = \bar{U}_\infty = 2 \text{ m/s}$ and (b) a stationary bottom wall

When the conveyor belt has the same velocity as the merged flow, there is a shear flow near the conveyor belt for a fully developed laminar flow. This would not be the case if the top plate is also moving at the average merged flow velocity. For $Re=10000$ the turbulent intensity for the case of two moving belts is displayed in figure 3.25.

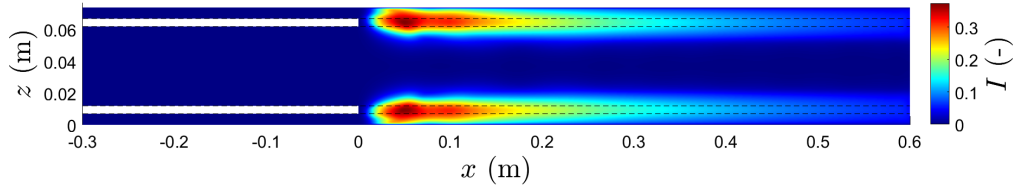


Figure 3.25: Turbulent intensity for $Re \approx 10000$, with both top and bottom wall moving at $u_{wall} = \bar{U}_\infty = 2 \text{ m/s}$

In figure 3.25, there are only 2 turbulent intensity spots directly behind the plate, that are slowly dampening out. Near the center of the domain no fluctuations are observed.

Because in the experimental set up, there is no conveyor belt at the top wall, it is useful to find a setting for the bottom belt where there is no shear flow at the belt, and if it possibly results in less fluctuations. In order to achieve no shear at the bottom belt in the case of a fully laminar flow, the belt is increased to 1.5 times the averaged merged flow velocity. In figure 3.26, color plots of the velocity and turbulent intensity for a simulation with $Re \approx 10000$ are made with the adjusted bottom belt velocity.

The fluid layer from the top channel merges with the center fluid layer within the first 10 cm behind the plate, as is seen in figure 3.26a. This is not the case for the fluid coming from the bottom channel. Instead, the fluid layers are separated by the vortex shedding behind the plate. This vortex shedding that dampens out over one meter distance behind the plate, while it is not distorted by the vortices coming from the top plate. Hence, having no shear at the belt by increasing its velocity seems to be an improvement. Therefore, it is worthwhile to test such a

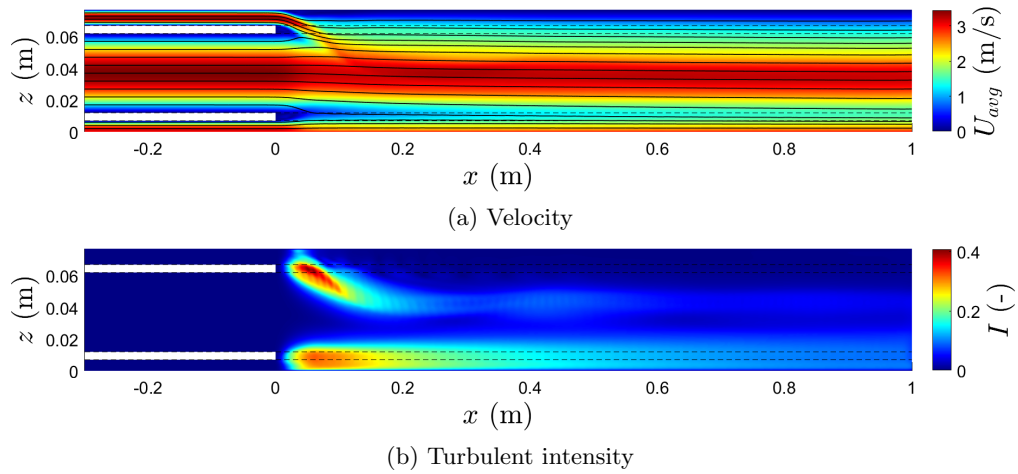


Figure 3.26: (a) Velocity and (b) turbulent intensity for $Re \approx 10000$, with the bottom wall moving at $u_{wall} = 3$ m/s

setting in the experimental setup.

With only the splitter plates between the inlet channels, the inclusion of the bottom conveyor belt moving at a similar velocity as the average merged flow, results in more fluctuations in the domain. Van Vugt[9] observed the opposite, as the belt did reduce the fluctuations during his experiments. As there is a difference between the dissipation of vortices in 2D flows and 3D turbulence[29], it is worthwhile to measure the flow field within the setup with the bottom conveyor belt experimentally. Significantly less turbulent intensity is observed when either the bottom belt velocity is increased such that there is no gradient in the average velocity at the belt, or when a second belt is installed at the top wall moving at a similar velocity. It is therefore advised to investigate these settings experimentally in the experimental setup.

3.3.4 Geometry and thickness of the splitter plates

With the splitter plates having a thickness of 5 mm, they both fill up for 6.5% of the height of the domain each, totalling 13%. Therefore, it is of interest to investigate whether either changing the thickness of the plates, or the shape of the edge of the plate results in a decrease of turbulent intensity. In this subsection, simulations are conducted where the thickness of the splitter plates have been decreased to 3 mm, while simultaneously widening both the top and bottom channel with the 2 cm removed from both plates. Furthermore, it is investigated whether rounded and triangular caps on the 5 mm plates reduce the turbulent intensity.

The effects of a thinner plate on the turbulent intensity is investigated for $Re \approx 10000$. In figure 3.27, the turbulent intensity in the wake of the 3 mm thick plates is compared with that of the 5 mm thick plates.

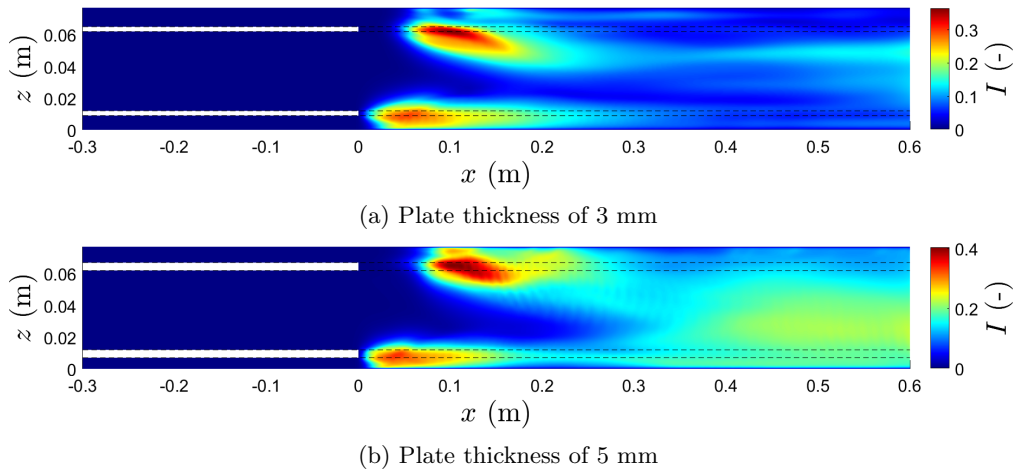


Figure 3.27: Turbulent intensity for $Re \approx 10000$, with (a) a plate thickness of 3 mm and (b) a plate thickness of 5 mm.

In figure 3.27, the location of the two turbulent intensity spot behind the plates is at similar locations for the 3 mm plates compared to that of the 5 mm plates. The difference is found in the magnitude of the fluctuations: The maximum turbulent intensity directly behind the 3mm plates is lower at values of 0.36 and 0.30 for the top and bottom plate respectively, as opposed to 0.41 behind the top plate and 0.34 behind the bottom plate for the 5 mm plates. Furthermore, the tail behind the top side turbulent intensity spot is both smaller in size, and has a lower value turbulent intensity. However, near the end of the domain, the fluctuations start to increase near the center of the channel.

The effects on the turbulent intensity are investigated for the case of attached rounded caps at the plates ends at $Re \approx 7700$ and 10000. For both simulations, the domain length was set equal to one meter behind the plates. In figure 3.28, color plots of the turbulent intensity for both Reynolds numbers with and without rounded caps are plotted.

Rounded caps do not significantly influence the locations of the high-value turbulent intensity spots. Instead, the differences are found in the tails coming from the fluctuations created behind the top plate. For instance, the top tail in figure 3.28a is directed under a less steep angle than the top tail in figure 3.28b. These tails influence the shape of the third turbulent intensity spot. A more downwards directed tail results in more flat third turbulent intensity spot. In figure 3.28c, the addition of the rounded caps results in a more downwards tail compared to figure 3.28d, whereas in figure 3.28a, the addition of caps cause the opposite effect to take place. Therefore, it

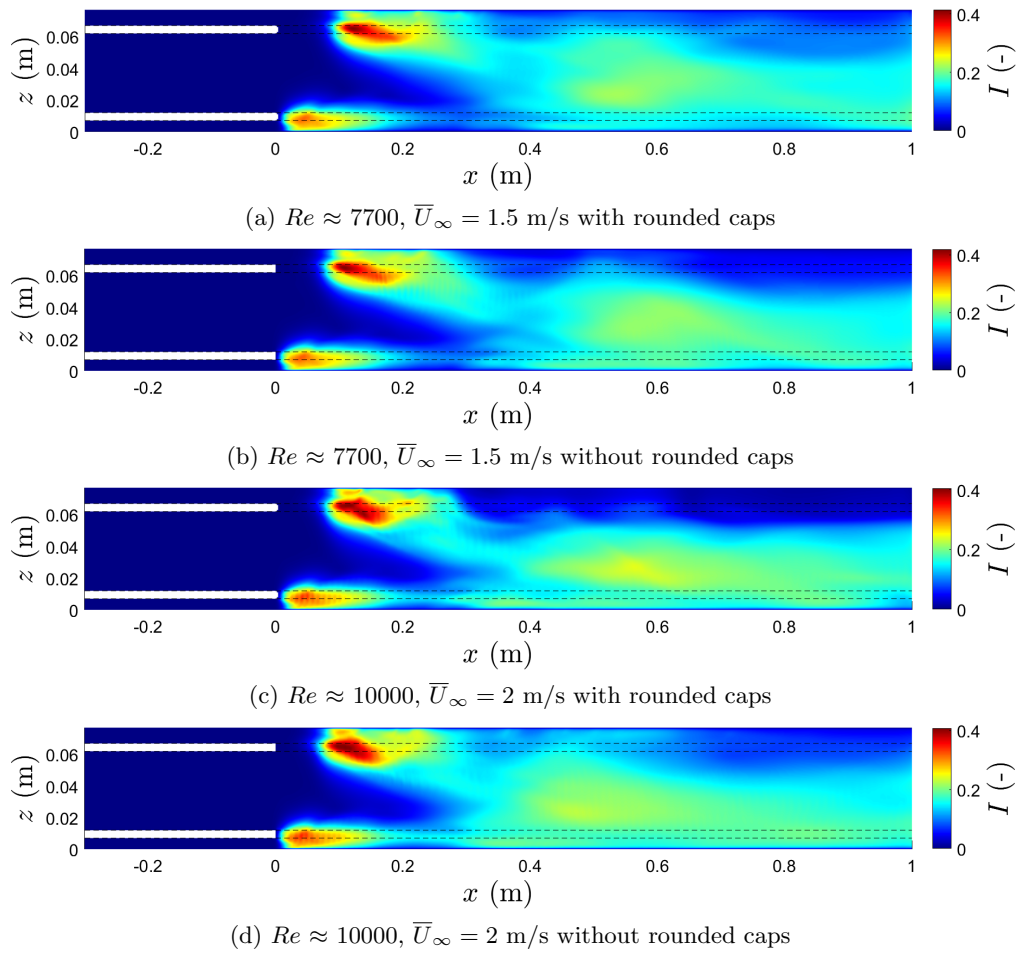


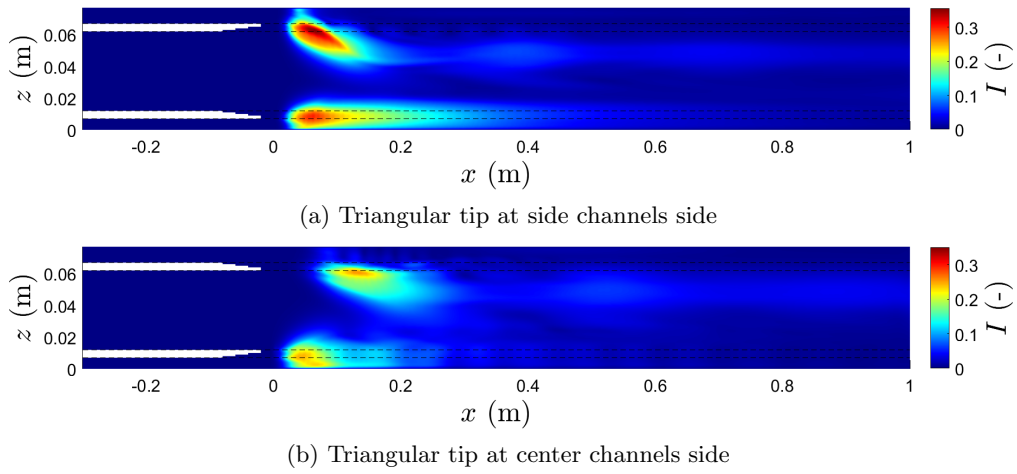
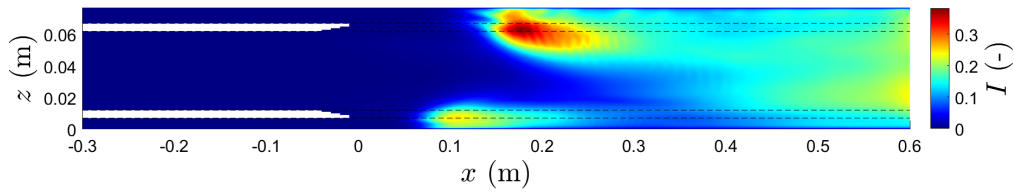
Figure 3.28: Turbulent intensity for (a,b) $Re \approx 7700$ and (c,d) $Re \approx 10000$, (a,c) with rounded caps and (b,d) without caps.

is not safe to conclude whether rounded caps results in less fluctuations.

The effects of triangular caps on the flow have been investigated. These triangles have a sharp tip at the end, which is either at the center channels side of the plate or at the side channels side of the plate. The length of these triangles has been chosen to be equal to 10 cm. In figure 3.29, the turbulent intensity is plotted for these cases.

Figure 3.29 shows that the addition of 10 cm long triangular caps at the end of a plate reduce the turbulent intensity is significantly. The caps with tips at the center channels side results in a significantly smaller turbulent intensity close to the plates than the caps with the tips at the side channel side. But near the end of the domain the turbulent intensities are similar in size.

The length of the triangular tip does influence the turbulent intensity as seen in figure 3.30, where the length of the triangular cap is only 5 cm long. The start of the fluctuations is at a further distance from the plates than observed for the 10 cm triangular plates. Furthermore, the fluctuation in the turbulent intensity spot are of larger value that result in also a larger tail of fluctuations. This tail results in a significant amount of fluctuation to start to occur near the end of the domain.

Figure 3.29: Turbulent intensity at $Re \approx 10000$ with triangular caps.Figure 3.30: Turbulent intensity at $Re \approx 10000$ with triangular caps.

In this subsection, it has been found that the splitter plate thickness influences the turbulent intensity generation in the wake of the plates. Thinner plates result in significantly less turbulent intensity. Because the plates in the experimental set-up cannot be made more thin, splitter plates with both rounded caps and triangular caps attached to their ends were simulated. While rounded caps did not result in significant differences in turbulent intensity, it was found that triangular caps reduce the turbulent intensity significantly. Based on the results, it is worthwhile to install 10 cm triangular caps, with the tips at the center channels side, on the splitter plates in the experimental set-up in order to reduce the turbulent intensity generated by these plates.

Chapter 4

Experimental Research

4.1 Experimental set-up

A top view the experimental set-up in the laboratory is displayed in figure 4.1.

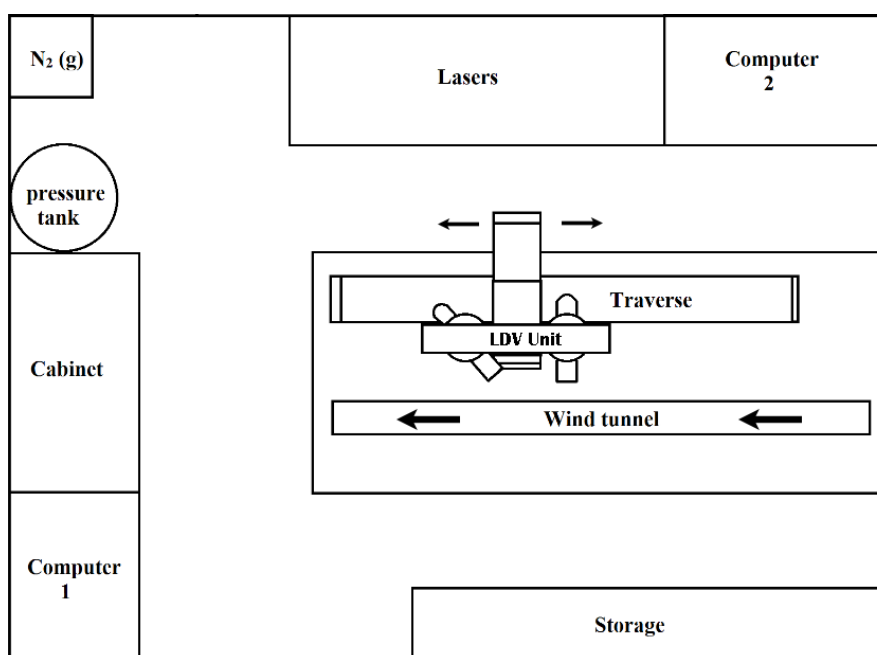


Figure 4.1: Top view of the laboratory and experimental setup. Altered from Bruining[30].

In the wind tunnel nitrogen gas is used. This gas enters the room in the top left of the figure and is fed into the pressure tank. This pressure in this tank is controlled by computer 1, and is used to maintain a constant pressure, and thus stabilizing, the flow. The nitrogen gas comes out at the other side of the pressure tank, and is fed in the cabinet where it is split into three flow streams, each for a different inlet duct in the wind tunnel. For each of these three streams, three different sized valves are present to obtain a constant desired velocity in each of the three inlet ducts. These valves are controlled by computer 1. The three streams are fed towards the right hand side of the wind tunnel via the ceiling. At the ceiling, the streams first pass humidifiers, that use distilled water to humidify the nitrogen gas. For the top and bottom inlet duct, a UCAN FT-K42UV ultrasonic humidifier unit is installed, while for the center duct, a UCAN FT-P22~302UVSV-CE ultrasonic humidifier unit is installed. At the left hand side of the wind

tunnel, a pipe is attached that transports the humidified nitrogen out of the room and outside of the building. Details of the wind-tunnel and measurement equipment are discussed in sections 4.1.1 and 4.1.2.

The measurements are conducted using Laser Doppler Velocimetry (LDV), of which the physical principle is dealt with in subsection 4.1.2. For this purpose, 3 lasers are used: Genesis MX488-1000 SLM, Genesis MX514-1000 SLM and Genesis MX532-1000 SLM. These three lasers are split in 2 beams each and are directed into optical cables that lead them to fiber optic probes attached to the Traverse that focus them in one point in the wind tunnel. The Traverse can be moved using the program Flowsizer on computer 2 in the x, y and z-direction. The probes used are a 2D TSI TR260, placed perpendicularly to the wind tunnel, and a 1D TSI TR160, that is placed under an angle. The optic signal is measured by the probes and is then directed to the TSI PDM1000 Photodetector Module that converts it to an electronic signal. This electronic signal is converted by the TSI FSA4000 Signal Processors into data that can be analysed using the TSI program Flowsizer on computer 2.

4.1.1 Wind tunnel

The measurements are conducted inside the wind tunnel. The length of the wind tunnel is about 2500 mm, and for the first meter, it is separated into three ducts by two 5 mm thick plates[8]. The x-axis has been defined in the length of the wind tunnel, with $x=0$ the end of these plates and the flow direction in the positive x-direction. The y and z-axis represent the width and height respectively. In the end of the center duct a honeycomb can be installed, resulting in the side view displayed in figure 4.2.

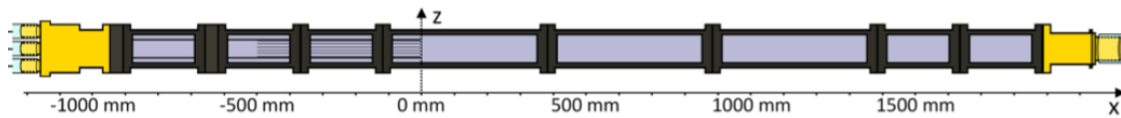


Figure 4.2: Schematic representation of the x-z cross section of the wind tunnel.[8]

Figure 4.3 shows the wind tunnel at $x=0$ mm. The honeycomb was taken out while this photo was made.



Figure 4.3: Picture of the wind tunnel with the the honeycomb and glass plate removed.

A 5 meter long conveyor belt is installed at the bottom wall, as seen in figure 4.3, for which entrance slots are made in that wall at $x=-520$ mm and near the end of the tunnel. The gap in the bottom inlet duct is made small by attaching a thin plastic strip to the top of the bottom wall

that overlaps a small part of the belt. The conveyor belt itself has thickness of 3 mm, that results in a thinner bottom inlet duct than top inlet duct as seen in the left figure in figure 4.4.

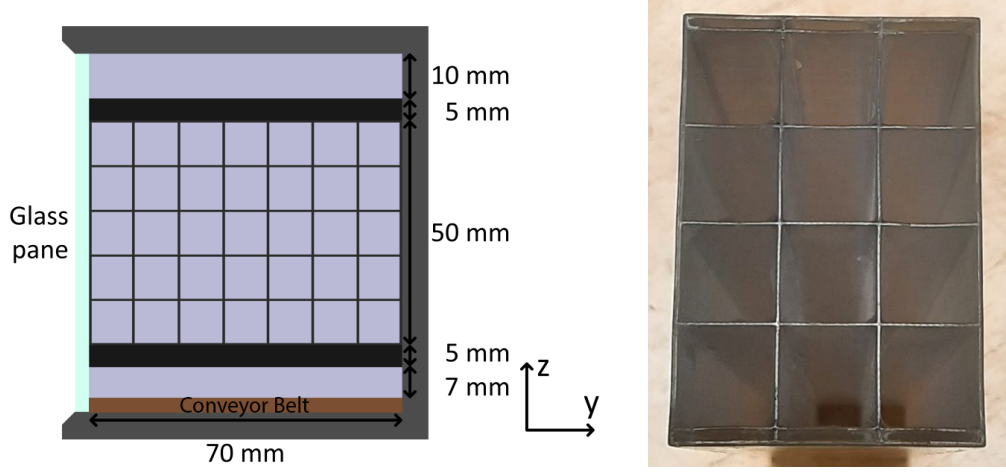


Figure 4.4: (Left) Schematic representation of the y-z cross section of the windtunnel, altered from van Vugt[9]. (Right) z-y cross section of honeycomb 3.

On the left hand side of duct, a glass plane is inserted where the lasers shine through. Furthermore, in the center duct a honeycomb is installed. The honeycomb used during this project is honeycomb 3, displayed in the right hand side of figure 4.4. It consists of 12 large cells and 6 small cells. The width and height of the honeycomb are 69.7 mm by 49.4 mm respectively.[9] The other dimensions are shown in table 4.1.

Table 4.1: The dimensions of the cells and the wall thickness of honeycomb 3[8].

Length	Height cell	Width cell	Width thin cell	Thickness wall	D_h cell	D_h thin cell
300 mm	15.6 mm	15.6 mm	1.6 mm	0.5 mm	15.6 mm	2.9 mm

With these dimensions, the porosity of the cell is calculated. When dividing sum of the areas of all the cells by the total frontal area of the honeycomb, a value of $\phi=0.892$ is found. However, when computing the Stokes equation in equation 2.12 for both a 15.6 x 15.6 mm cell and a 1.6 x 15.6 mm, it is found that for the same pressure gradient, the average velocity between these two cells differs by a factor 43. Hence, effectively the porosity is $\phi_{eff}=0.849$ for the large cells.

4.1.2 Laser Doppler Velocimetry

For each wavelength, a pair of split laser bundles are directed under an angle with respect to one another, such that the beams overlap. In this overlap an interference fringe pattern is created by the lasers. The fringe spacing depends on the wavelength and the angle of the lasers as

$$d_f = \frac{\lambda}{2 \sin \alpha}. \quad (4.1)$$

When a particle, in this case a water droplet, moves through the overlap of the lasers bundles, light is scattered with a sinusoidal varied intensity. The velocity component, in the same direction as the subtraction of the direction-vectors of the two laser beams, of that waterdroplet can be calculated using the fringe spacing and the frequency as

$$u_i = d_f f_d. \quad (4.2)$$

Hence for measuring three velocity components, three lasers are needed. In figure 4.5, the working principle of LDV is displayed.

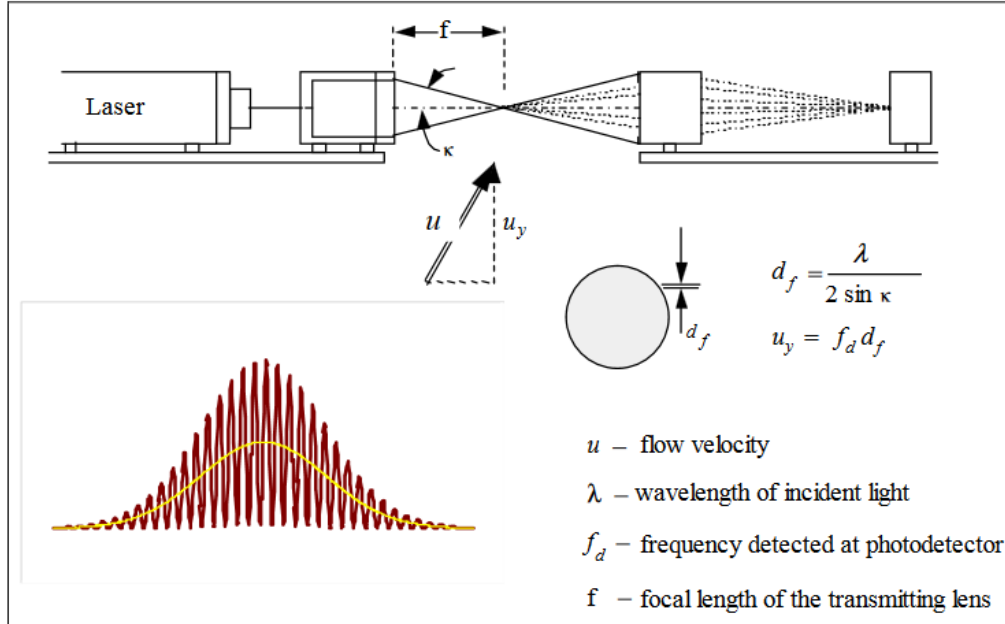


Figure 4.5: Schematic representation of the working principle of LDV.[31]

The data received from the measurements is optimized by the the TSI software to obtain reliable results. For instance, it checks whether all the droplet is measured by all 3 beams at the same by checking whether the three received pulses coincide. If the data does not coincide, it is dropped.

The location of the measurements are constructed using scan matrices within the TSI program Flowsizer. These matrices included the x, y and z-location of the measurement point. For every points, 10000 separated coincided measurements are taken, for which the velocity components and the root mean square of those velocity components are saved. In the TSI program Flow sizer, data rate is shown and the individual measurements are plotted, so the user could check whether the settings for the measurements are correct.

4.2 Results and Discussion

This section contains the results of the measurements using the experimental setup. Before conducting the experiments, the effects of the leakage in the bottom duct found by Van Vugt[9] are quantified. For this purpose, the average velocity is determined as a function of the belt velocity for velocity settings of 1 m/s, 1.5 m/s and 2 m/s, and then the effects of the set velocity is on the leakage in the bottom duct with the belt stationary is investigated. After having performed the calibration, measurements are performed to check the calibration. Furthermore, the flow profile ejecting out of the center cells of honeycomb 3 has been compared with direct numerical simulations of fully developed turbulent duct flow. Then the honeycomb was removed, and vertical measurements were performed directly behind the inlet ducts.

4.2.1 Leakage bottom duct

For the leakage of the bottom duct, it is decided to measure directly inside the bottom duct at 7.95 cm upstream of the end of the bottom channel. This is done to prevent that upstream merging

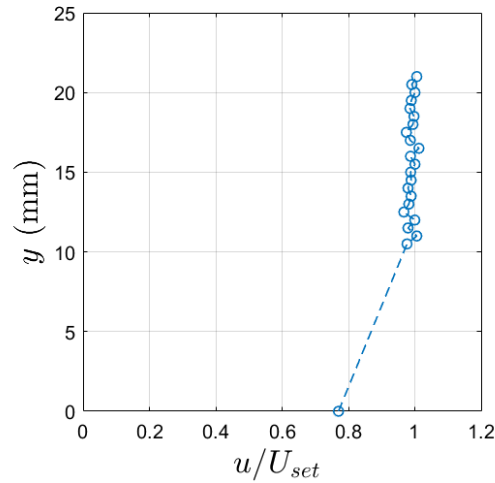


Figure 4.6: Velocity in the bottom duct versus the depth coordinate measured with the velocity set up as 2 m/s and the belt moving at 1 m/s.

affects the measured flow and generates unreliable results. Measuring the flow in a duct with aspect ratio 10 as a function of the height is difficult because of the orientation of the laser beams. Hence, the measurements of the flow inside the bottom duct were performed only as a function of the depth, in the y -direction, at roughly half height. The belt speed has a mayor influence on the flow profile, including the z -coordinate of the maximum velocity. Therefore, it is easiest to calculate the average velocity in the duct using measurements on fully developed laminar flow, as the profiles of fully developed laminar duct flows are known (see chapter 2, section 2). For this purpose, equation 2.21 is rewritten into

$$U = (u_m(y, z) - u_C(y, z)) \frac{u_{P,avg}}{u_P(y, z)} + u_{C,avg}, \quad (4.3)$$

where $u_C(y, z)$, $u_{C,avg}(y, z)$ and $u_P(y, z)/u_{P,avg}$ are all known if both the dimensions of the duct and speed of the belt are defined, and $u_m(y, z)$ is the measured velocity at a certain location in the duct. In equation 2.21 $u_m(y, z)$ is denoted as $u(y, z)$, but now it is the measured velocity. Equation 4.3 shows that measuring the data for a single point can already determine the average velocity in the domain. The accuracy of the "measured" average velocity is improved by combining the calculated averaged velocities from measurements at twenty different locations. Because of the large aspect ratio of the duct, the velocity is practically independent of the y -location for depth larger than one centimeter. Therefore, the measurement procedure was to first measure a point as close as possible to the wall ($y=0$ in figure 4.6), and then move one centimeter deeper in the domain to start the actual measurements used to calculate the average velocity. An example of a typical measurement is shown in figure 4.6, where the ratio of the measured streamwise velocity and the velocity setting is plotted as a function of the depth.

From these data points in figure 4.6, the average streamwise velocity is calculated, where errors in the belt velocity, y - and z -location and the root-mean square velocity are all taken into account. In order to make sure the flow is laminar, the turbulent intensity is calculated with the measured root-mean square velocity components and calculated average streamwise velocity. The data points of the "measured" average velocity where the turbulent intensity is large are unreliable and thus ignored. In figure 4.7, the average velocity and the turbulent intensity is plotted for a velocity set equal to 1 m/s.

In figure 4.7a, when the belt starts moving with a small velocity, the average velocity drops from 0.68 m/s to 0.61 m/s. Increasing the belt speed further results in a slow rise of the "measured" velocity towards values measured with the belt off. With the belt speed at 3 m/s, the measured

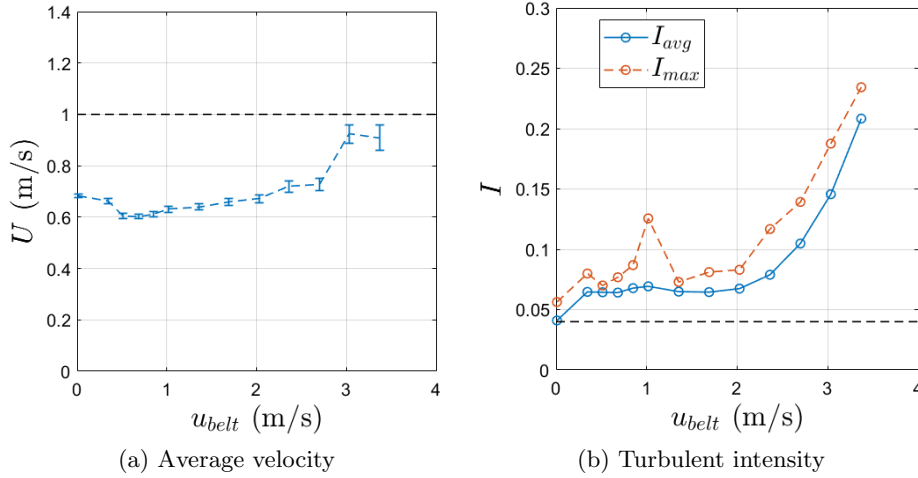


Figure 4.7: (a) Calculated average velocity and (b) turbulent intensity as a function of the belt speed for the velocity setting equal to 1 m/s.

average velocity suddenly rises to about 0.9 m/s. The error bars also increase significantly in size. This change is caused by the flow becoming turbulent, as seen in figure 4.7b. There the turbulent intensity starts to rise from steady values of about 0.07 at belt velocities up until 2 m/s, towards 0.2 for a belt velocity of 3.3 m/s. The velocity with $u_{belt} > 2$ m/s are therefore not valid results, as the flow is no longer fully laminar and thus equation 4.3 does not hold. **From $u_{belt} = 0.5$ m/s to $u_{belt} = 2$ m/s, the measured average velocity does increase at a rate of 0.04 m/s per one meter per second increase in belt velocity.**

With the belt off, the turbulent intensity is 0.04. This is due to the valves adjusting itself constantly to maintain an inlet velocity of about 1 m/s, resulting in small fluctuations in the flow. Dellaert[8] determined that the noise created by the valves is $I = 0.04 \pm 0.02$, which is in agreement with the measured value. The movement of the conveyor belt is also not perfectly smooth, which is the reason of the increase of the turbulent intensity to 0.07 when the belt is turned on.

In figure 4.8, the "measured" average velocity and turbulent intensity are plotted as a function of the belt velocity for both $u_{set} = 1.5$ m/s and $u_{set} = 2$ m/s.

In figure 4.8, the flow becomes unstable at significantly lower belt velocities than in figure 4.7b, resulting in less amount of useful data points. With these useful data points, one can determine that the belt speed has about the same rate of increase as found in figure 4.7b. Comparing this to the magnitude of the measured average velocity, the belt influence on the leakage, and thus the average flow in the bottom duct, is practically negligible compared to the average velocity. This is also assumed for larger velocity settings of the bottom duct than 2 m/s.

The previous analysis is possible, as for fully developed laminar flows, the flow profile has analytical solutions, even though they consist of infinite sums. For transitional and turbulent flows this analysis is no longer possible. This is already the case for velocities larger than 3.3 m/s, where the Reynolds numbers exceed the critical Reynolds number 2800 of a large aspect ratio rectangular duct[15]. Instead, there has been opted to compare the peak velocity in the bottom duct with stationary belt with the peak velocity in the top duct. This comparison is made, as it is known that there is no leakage in the top duct. For this purpose, similar measurements are performed as shown in figure 4.6, where the height of the measurement at half the height of the domain. For both the top and bottom duct, the peak velocity is plotted as a function of the velocity setting in figure 4.10.

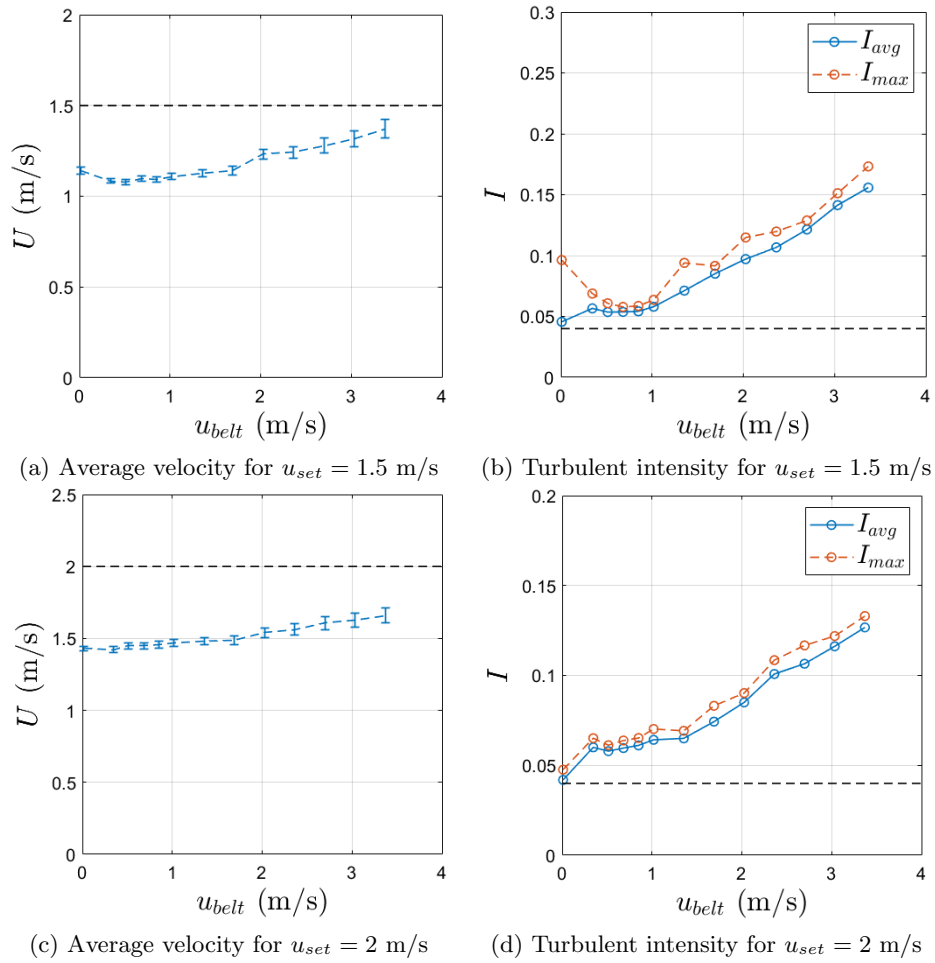


Figure 4.8: (a,c) Calculated average velocity and (b,d) turbulent intensity as a function of the belt speed for the velocity setting equal to (a,b) 1.5 m/s and (c,d) 2 m/s.

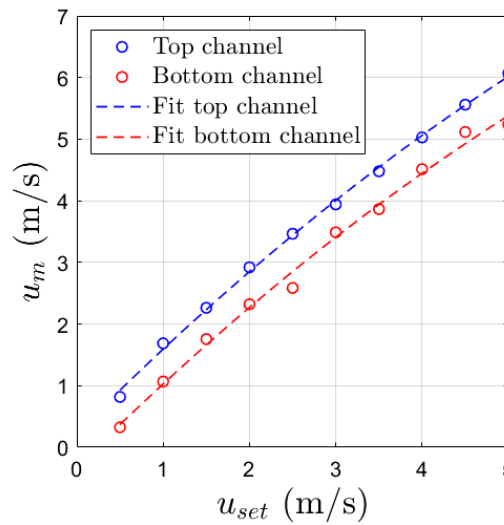


Figure 4.9: Measurement of the maximum velocity in the top and bottom duct as a function of the inlet velocity, including quadratic fits.

If the velocities in figure 4.10 would be laminar, the trends in figure 4.10 would be linear with a slope of 1.6. Because of the transition to turbulence, the K-factor decreases for larger velocities, which explains the observed curvature. The data follows a quadratic trend well, which is why it is fitted with quadratic trends. These fits are used to generate data points such that for each measured velocity, the velocity setting of the bottom inlet duct can be compared with that of the top inlet duct. With this, a relation was made between the velocity in the top duct and a velocity in the bottom duct, such that the average velocity in both ducts are the same,

$$u_{avg,bot} \simeq u_{set,top} = -0.0059u_{set,bot}^2 + 0.9732u_{set,bot} - 0.3940. \quad (4.4)$$

As the velocity set in the top duct is equivalent to the average velocity there, the average velocity in the bottom duct is also equivalent to the velocity setting in the top duct. As a result the percentage of the leaked fluid out of the bottom duct can be calculated.

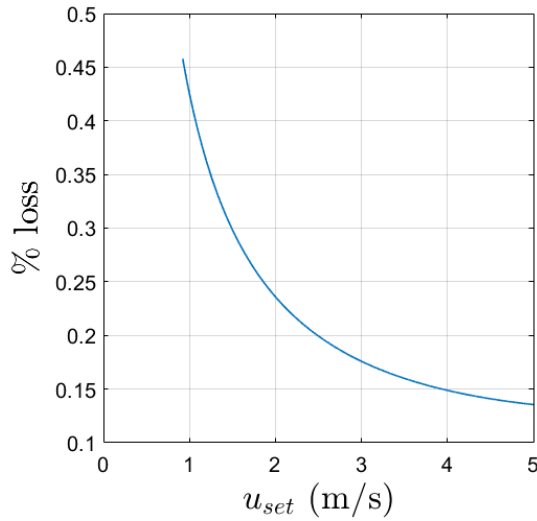


Figure 4.10: Percentage of the velocity that leaks out of the bottom duct at the start of the conveyor belt.

For low velocity settings, a significant part of the fluid leaks out of the bottom duct. The measurements done at 1 m/s, 1.5 m/s and 2 m/s only differ a few percent with the curve in figure 4.10. The leakage is relatively small for large velocity settings, with only 13% at 5 m/s inlet velocity. Somewhere during the time in between the measurements by Van Vugt[9] and these measurements, the gap at the start of the belt was closed better. Data by Van Vugt[9] indicates that more than 40% of the fluid was lost at velocity settings of roughly 2.5 m/s, whereas after the improvements of the setup only 20% of the fluid is now lost.

The top duct and bottom duct do not have completely similar dimensions, as the top duct has a aspect ratio 7, whereas the bottom duct has aspect ratio 10 while maintaining the same width. For a laminar flow solution, there is not much difference in the K-factor, as for a duct with a aspect ratio 7 it is equal to 0.648 as opposed to 0.601 for a duct with aspect ratio 10. The difference in hydraulic diameter between the 2 ducts is a factor 0.727, resulting in 1.375 times larger Reynolds number for the top inlet duct than for the bottom. This barely plays a role for fully turbulent flow, as the K-factor difference between the two ducts is only a factor 1.05 when the ratio is filled in the fit found by Driessen[6] in equation 2.46. In the transition region, the difference in Reynolds number does play a significant role, as there the K-factor changes significantly. This region is roughly between 2 and 3.5 m/s, where the fit might not exactly hold. For other velocity settings, the fit should hold, and therefore it has been used to set up the velocity at the bottom inlet duct.

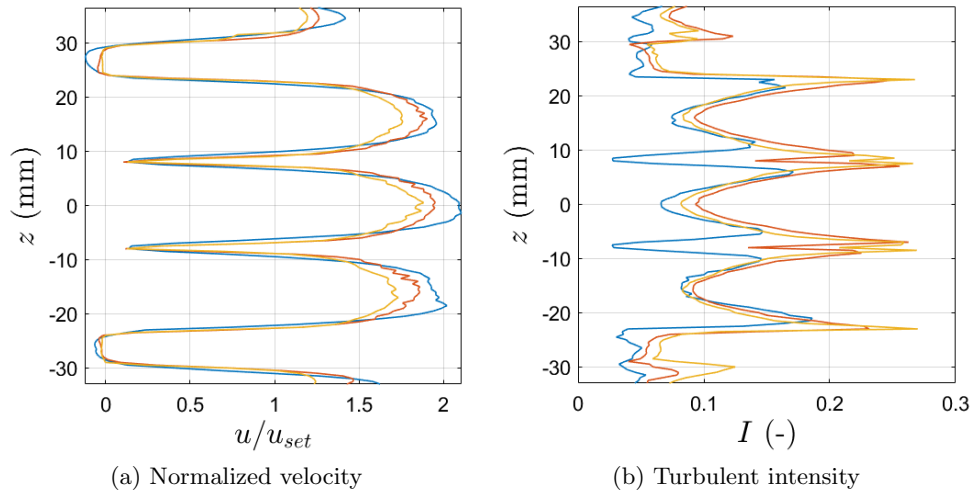


Figure 4.11: (a) Normalized velocity and (b) turbulent intensity measured at 3.5 mm behind the plates and honeycomb 3, for $u_{avg} =$ (blue) 1.5 m/s, (red) 3 m/s and (yellow) 4.5 m/s.

During this part, the leakage near the start of the conveyor belt was investigated and the implications on the flow in the bottom duct. It was found that the belt velocity had no significant effect on the leakage, but the velocity setting has an influence. A relatively large leakage was found for small velocity settings, which became smaller for increasing velocities. Lastly, a rough relation was found between the velocity setting and the average velocity in the bottom duct, that can be used to set up the velocity there properly.

4.2.2 Measurements with honeycomb 3.

Measurements at 3.5 mm behind the plates were conducted with honeycomb 3 inserted in the center inlet duct as a function of the height z . Because the width of the honeycomb is subdivided into four cells, the y -location of the measurements was taken at the center of one of the two center cells instead of the center of the inlet ducts. The measurements were conducted for average velocities equal to 1.5 m/s, 3 m/s and 4.5 m/s, with the conveyor belt turned off. In figure 4.11, the mean streamwise velocity, averaged with the velocity setting, and the turbulent intensity is plotted as a function of the height.

For a laminar flow, the velocity ratios are calculated to be 1.65 and 1.60 for the top and bottom side inlet duct respectively. The measurements for 1.5 m/s (blue) in figure 4.11a indicate that the maxima ratio of the velocity in the bottom inlet duct is in agreement with these calculated velocity values, but the ratio of top inlet duct has a value of about 0.15 too low. As the flow is expected to be laminar, it is likely that the velocity setting in the top duct is smaller than that in the bottom duct.

In figure 4.11a, the maximum velocity ratio in the center honeycomb cell is equal to 2.09 for the 1.5 m/s velocity setting. Taking the porosity of the honeycomb, $\phi = 0.849$, into account, the maximum velocity ratio is equal to 2.46 for a fully developed laminar flow. The Reynolds number of this flow through the honeycomb at a 1.5 m/s velocity setting is equal to 1700, so the flow is laminar. For the flow at this Reynolds number to be fully developed, 85 hydraulic diameters are required according to equation 2.5. The honeycomb has a length of 0.3 m, which is only twenty hydraulic diameters. Hence, the flow is not fully developed. For increasing velocities, the maximum velocity ratio decreases, but not as much as predicted by the fit for the K-factor in equation 2.46. For 4.5 m/s (yellow), $Re \approx 5100$, the fit indicates a K-factor of 0.32, which is far less than $K=0.8$ for the center honeycomb cell and $K=0.7$ for the top and bottom honeycomb cell. The difference between the K-factor of the top and bottom cell compared to the center cell hints at an inhomogeneity of the fluid distribution over all honeycomb cells, where more fluid is being

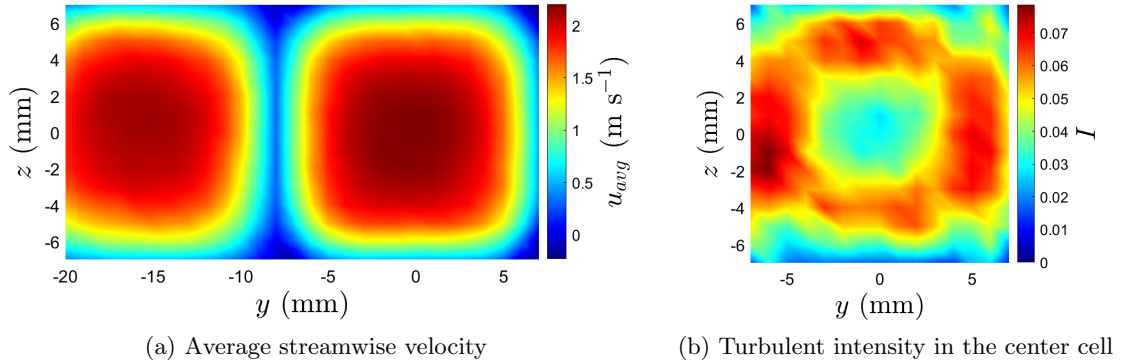


Figure 4.12: Measurement of (a) the average streamwise velocity and (b) the turbulent intensity in the wake of a center cell of honeycomb 3 with velocity setting equal to 1 m/s.

pushed through the center cells than the other cells. Driessen[6] also observed this inhomogeneity for lengths of honeycomb 3 at lengths equal to 0.7 m, which is considerably longer than the used honeycomb. The inhomogeneity can be investigated further by also measuring the velocity coming through the three cells near the glass.

Figure 4.11b shows that the turbulent intensity in the side inlet ducts are of the same magnitude as the noise found by Dellaert[8], indicating that the flow in these ducts is indeed laminar. For inlet settings 3 m/s and 4.5 m/s, the turbulent intensity in the side inlet duct at the top side increases faster than that in the bottom side inlet duct, which is the result of the larger hydraulic diameter, and thus larger Reynolds numbers. These turbulent intensities are very small compared to the turbulent intensities measured in the wake of the honeycomb cells. There the turbulent intensity has spikes up to 0.27 for both 3 m/s and 4.5 m/s velocity settings in the near wake of the honeycomb walls. The shape of the turbulent intensity in the near wake of each of the honeycomb walls is characterized by two turbulent intensity peaks at both sides of the plate, with a small dip in turbulent intensity in between. This is agreement with turbulent intensity measurement in the wake of several honeycombs by Thijs[5], where a similar patterns in turbulent intensity were observed.

The measurement with velocity setting of 1.5 m/s shows significant turbulent intensity larger than 0.1 in the wake of the honeycomb, which is possibly the result of the flow not fully developed. This can be verified by measuring the turbulent intensity behind a longer honeycomb 3.

Measurements of the three velocity components in the yz -plane at a 3.5 mm distance behind the second cell from the window side in the middle row were performed for velocity settings equal to 1 m/s, 3 m/s and 5 m/s. The resolution of these measurements is one measurement per millimeter. The measurements for 3 m/s and 5 m/s are compared with direct numerical simulation (DNS) performed by Kuerten[32]. In order to resolve one of the boundaries better, parts of the cell in the middle row next to the window was also measured. For an 1 m/s velocity setting, the measured average streamwise velocity and turbulent intensity is displayed in figure 4.12.

Figure 4.12a shows very clearly the duct profiles in the cells. There is a slight inhomogeneity in fluid distribution between the cells. The velocity maxima in the center cell is significantly larger than the cell on the left hand side. When calculating the average velocity coming out of the center cell, an average velocity of 1.35 m/s is found, which is about 20% more than the expected velocity. With the maximum measured velocity being equal to 2.2 m/s, the K-factor is only 0.6 for Reynolds number 1400. Some fluctuations are found near the edges of the center cell in figure 4.12b. Near the center of the that cell, the turbulent intensity has a value at about 0.035, which is in agreement with the 4% fluctuations of the setup.

For a Reynolds number of 1400, 70 hydraulic diameters are required for a fully developed

laminar duct flow. Comparison of the flow profile displayed in figure 4.12 is made with the fully developed laminar flow solution in equation 2.16. This is done by normalizing the both velocity profiles with their respective averages. Figure 4.13 shows that after 20 hydraulic diameters the measured flow is not fully developed. Close to the walls, for the first 1.5 mm, the profiles overlap, indicating that the flow is developing towards the fully developed laminar flow profile. However, the velocity in the center of the cell is far from developed.

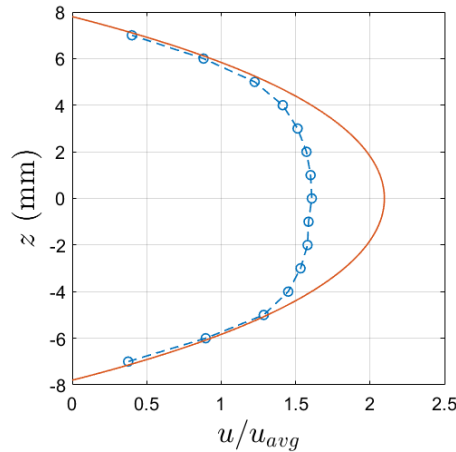


Figure 4.13: Measurement of the velocity profile over the center line of the cell compared to the fully developed laminar flow solution.

In figure 4.14, the average streamwise velocity and the turbulent intensity are displayed for 3 m/s and 5 m/s velocity settings. These are compared to direct numerical simulations conducted by Kuerten[32] at $Re = 4300$ and $Re = 7100$.

Comparison of figures 4.14a and 4.14c with figures 4.14b and 4.14d respectively, shows that area of the measurements behind the center cell is on the small side, as the top, bottom and right hand side edges are cropped off. The reason for this is that the cell height and width was 0.6 mm larger than the total area of the measurements, resulting in roughly 0.3 mm being cropped off at each side. Besides that distance being unnoticeable by eye when setting up the measurement equipment, it would also be impossible to resolve it by adding another measurement point 1 mm from the last point. Instead, a finer measurement grid with a slightly larger area would be required to resolve the edges well. Another effect of resolution of one measurement point per millimeter, is that features in the average streamwise velocity are barely to not visible. The measured ratios of the maximum streamwise velocity over the average streamwise velocity is found to be very close to the ratios obtained from the DNS; For 3 m/s velocity setting, $u_{rat}=1.30$, whereas for the DNS at $Re=4300$ a velocity ratio of 1.32 was obtained, and for the 5 m/s velocity setting, $u_{rat} = 1.26$ compared to 1.28 for the DNS at $Re=7100$. The small differences in the velocity ratios are likely a result of the area of the measurements being slightly to small, resulting in a larger measured average velocity.

For most of the area of the cell, The measured turbulent intensities in figures 4.14e en 4.14g are conform to that simulated by Kuerten[32]. At the walls, the turbulent intensities measured are larger in value than is predicted by the DNS. Likely, the phenomenon of the additional turbulent intensity is the result of fluctuations caused by the merging of the fluid layers that were separated by the walls of the honeycomb. In previous reports[8][6][7], measurements of the decay of the turbulent intensity were performed behind the center of a cell, where the amount of fluctuations is low. However, it could be worthwhile to perform additional measurements behind the walls of a honeycomb cell, especially behind the crossings of these walls.

The velocity data, displayed in figures 4.14a and 4.14c, on a horizontal line at $z = 0$ mm, from the left wall of the center cell to the center of that cell, are converted into wall units and

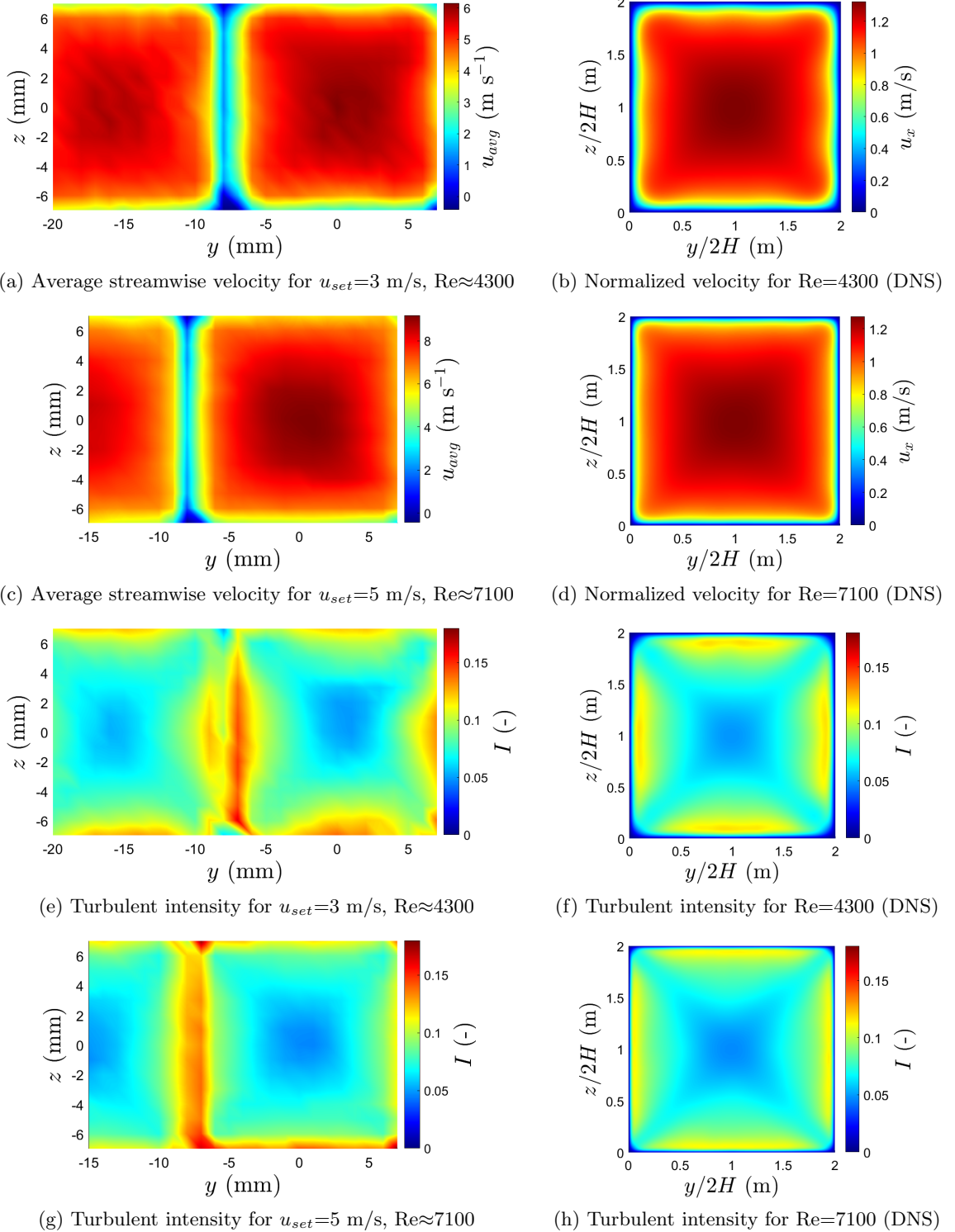


Figure 4.14: Measurements of (a,c) the average streamwise velocity and (e,g) the turbulent intensity in the center honeycomb cell for velocity settings of (a,e) 3 m/s and (c,g) 5 m/s on the left hand side compared with DNS performed by Kuerten[32] on the right hand side.

compared to both the direct numerical simulations (at $z/2H = 1$) and the theory of wall-bounded turbulence. The exact procedure for this conversion is found in the Appendix. In figure 4.15 the wall units for both the 3 m/s and the 5 m/s velocity setting are plotted.

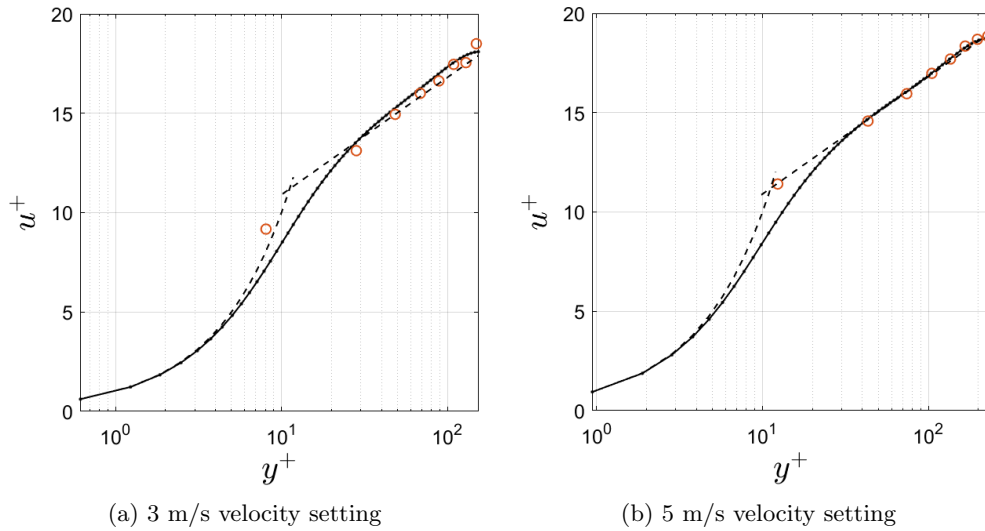


Figure 4.15: Wall units of the velocity profile in the center cell (orange circles) for (a) 3 m/s velocity setting and (b) 5 m/s velocity setting, including DNS data by Kuerten[32] (dotted line) and the theoretical fits of both the viscous sublayer and logarithmic layer (dashed lines).

In figure 4.15a, most of the measurements follow the direct numerical simulations very well, indicating a fully developed turbulent flow is emerging from the center cell. However, two outliers in the measurements are present; one near the center of the domain and one close to the wall. The outlier near the center of the cell, at $y^+ = 149$, is likely due to an measurement error. For the outlier near the wall at $y^+ = 8$, it is best to consider that the size of one y-unit is equal to 99 μm , meaning the four y-units difference accounts for a difference of 0.4 mm. Hence this outlier can be explained by error in the y-location of the measurement. In figure 4.15b, both the measurements and the DNS data are both conform to the logarithmic layer. Similarly to figure 4.15a, there is one outlier close to the wall. The data point at $y^+ = 12$ is 5 y-units to the left of the results for the DNS, which accounts for a distance of 0.3 mm as one y-unit is equal to 65 μm . It is also possible that the Reynolds number that was estimated for the simulations was slightly on the lower side, which inherently results in a shorter logarithmic layer. As the measurements are expressed in the wall units of the DNS, a larger Reynolds number results in smaller wall units and thus an upwards shift of the measurement along the dashed line, resulting in an decrease of the error.

The turbulent intensity is also plotted over the $z=0$ line in the center cell in figure 4.11. There the turbulent intensity from the DNS is also plotted for comparison.

In figure 4.16a, the difference between the measured turbulent intensity and that of the numerical simulations is small near the center. Near the walls of the cell, the measured turbulent intensity increases drastically, resulting in differences of more than 0.05 difference. Similarly, near the center in figure 4.16b, the measured turbulent intensity has the same values as the turbulent intensity of the DNS data, but near the walls the turbulent intensity also increases drastically.

4.2.3 Measurements without honeycomb

With no honeycomb inserted in the center channel, the flow profile has been measured over a vertical line at half the duct width of the center duct at inlet velocities of 1 m/s and 2 m/s with a resolution of two measurements per millimeter. These measurements are compared with DNS at

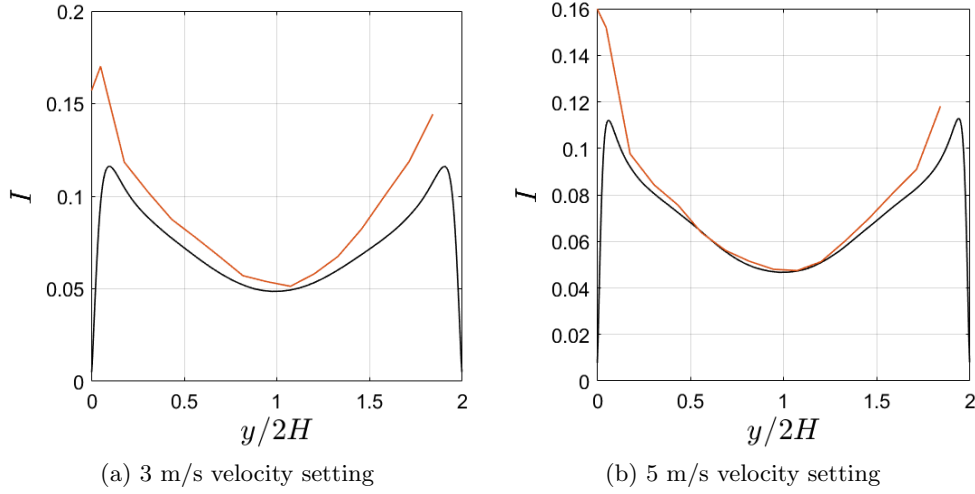


Figure 4.16: Turbulent intensity (orange) for (a) 3 m/s velocity setting and (b) 5 m/s velocity setting, including DNS data by Kuerten[32] (black).

$Re = 3868$ and $Re = 7737$ conducted by Kuerten[32]. In figure 4.17 the measured velocity profiles are compared with the DNS data.

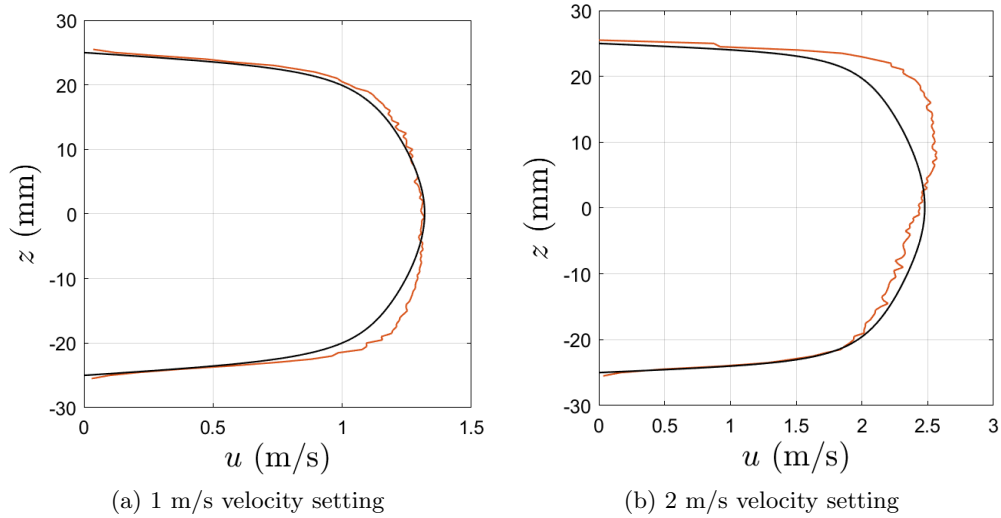


Figure 4.17: Velocity profile at the end of the center duct (orange) for (a) 1 m/s velocity setting and (b) 2 m/s velocity setting, including DNS data by Kuerten[32] (black).

The measured velocity profile in figure 4.17a, is very close to being fully developed, especially in the top half. It is expected that the flow is fully developed, as the entrance length in equation 2.44 indicates that the flow should be fully developed after 0.63 m. The velocity profile in figure 4.17b is further from being fully developed. For this velocity, the flow is expected to be developed after 0.74 m. As there The velocity profile in figure 4.17 is similar in shape to what was measured by Dellaert[8] for a velocity setting of 1.1 at $x=-575$ mm. The data in figure 4.17 has been converted into wall units. For the 1 m/s velocity setting, the top half of the velocity profile, and for the 2 m/s velocity setting, the bottom half of the velocity profile are both compared to the DNS data and theoretical fits.

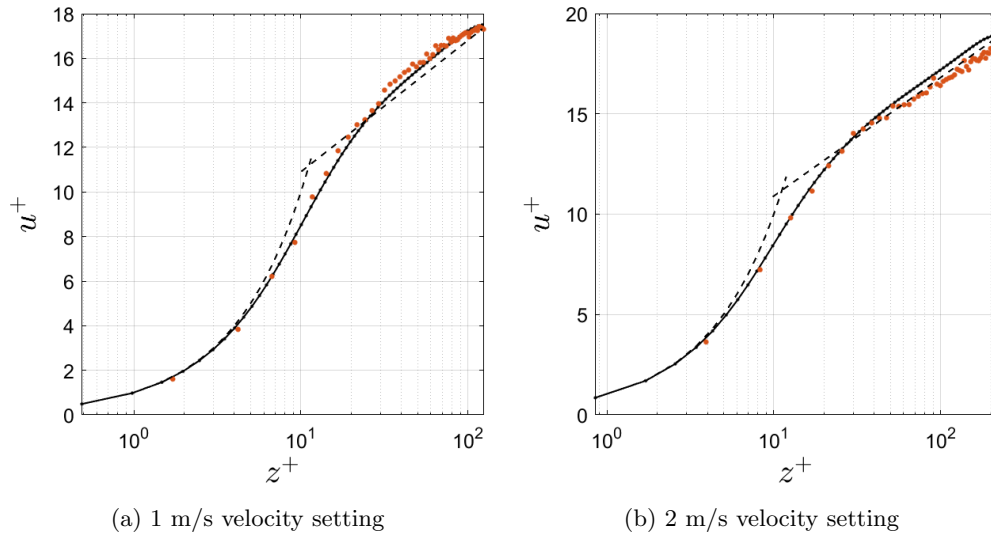


Figure 4.18: Wall units of the measured velocity profile in the center duct (orange dots) for (a) 1 m/s velocity setting and (b) 2 m/s velocity setting, including DNS data by Kuerten[32] (dotted line) and the theoretical fits of both the viscous sublayer and logarithmic layer (dashed lines).

In figure 4.18, the location of the measured data points was moved such that the measured velocities were on top of the DNS in the viscous layer. For figure 4.18a, the data is shifted 1.5 z -units in the positive direction, whereas in figure 4.18b the data is shifted 1 z -unit in the negative direction. This translates in a distance of 0.21 mm and 0.08 mm respectively, as one z -unit is equal to 140 μm and 82 μm . With this adjustment, the measurement data agrees with the DNS within the buffer layer. In the logarithmic layer, there are some differences as the flow is not fully developed, especially in figure 4.18b. The result of this undeveloped flow is also visible in the turbulent intensity displayed in figure 4.19b.

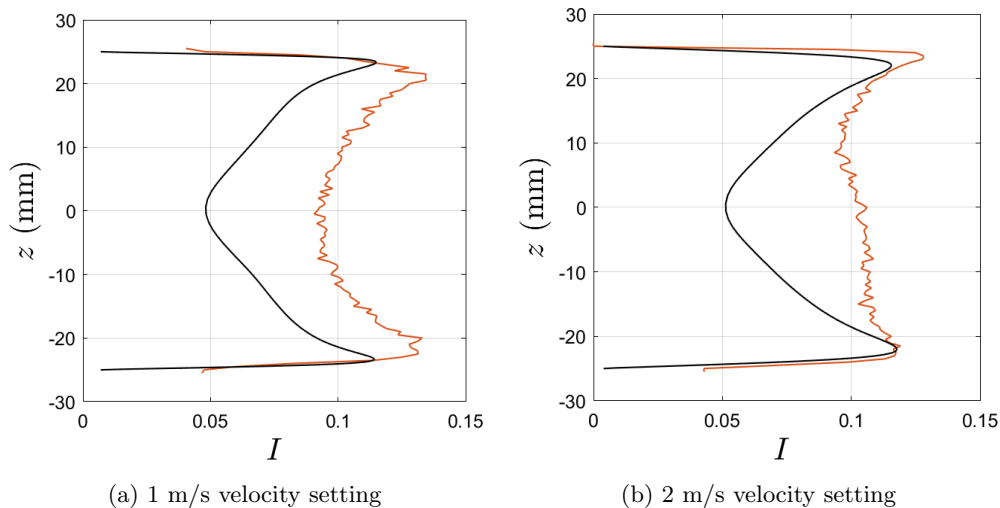


Figure 4.19: Turbulent intensity at the end of the center duct (orange) for (a) 1 m/s velocity setting and (b) 2 m/s velocity setting, including DNS data by Kuerten[32] (black).

The measured turbulent intensity profile in figure 4.19b is very different than the turbulent intensity found in the DNS, likely due to the flow being undeveloped. For a more developed flow, in figure 4.19a, the shape of the measured turbulent intensity corresponds more to that found using

the DNS, with the largest turbulent intensities close to the buffer layer. However, the measured values of the turbulent intensity are roughly 0.04 larger near the center of the duct and 0.02 larger close to the walls. This increase in turbulent intensity is caused by the inlet valves of the setup, as already discussed during the quantification of the leakage in the bottom duct.

Chapter 5

Conclusion

In this chapter, the results from the numerical simulations and the experimental work have been summarized. Recommendations for future research are given within this summary.

5.1 Numerical simulations

5.1.1 Instabilities zone

Numerical simulations are performed for the first time with a bottom conveyor belt, but without honeycomb included in the center channel. Initially the inlet channels have been set at a velocity of 77/67 times the average merged flow velocity, with the conveyor belt set equal to that velocity. In the wake of the bottom plate, the start of the fluctuations occurs very close to plate, while at the top plate, the fluctuations start several centimeters downstream of the trailing edge. For an increasing Reynolds number, the fluctuations move closer to the top plate, which was also observed in the wake of a honeycomb in previous measurements by Driessen[6].

5.1.2 Turbulent intensity in the wake of the splitter plates

The maximum turbulent intensity of the fluctuations in the wake of the plates was measured at the start of the instabilities. The fluctuation in the wake of the bottom plate jumps up from a zero value to 0.27 at a Reynolds number of 2200 to then slowly converge to a value just below 0.35. The turbulent intensity in the wake of the top plate increases more gradual: For Reynolds number up until 5000, the maximum turbulent intensity in the wake of the top plate was lower than the fluctuations in the wake bottom plate. In between $Re=5000$ and $Re=6000$, the maximum turbulent intensity at the top plate increased to 0.41, and stabilises for increasing Reynolds numbers.

For large Reynolds numbers, a tail was observed behind the turbulent intensity spot in the wake of the top plate, that diffuses downwards and causes significant turbulent intensity to appear 0.6 m downstream of the plates. There, the turbulent intensity increased up to 0.22 at Reynolds numbers above 7000. Over the next 40 cm, the turbulent intensity was observed to decay. At 0.6 cm downstream of the plates, the turbulent intensity at the top wall increases for increasing Reynolds numbers, as for increasing Reynolds numbers, more vortices are generated there.

5.1.3 Vortex shedding

Investigation of the frequencies at the maximum turbulent intensity spots showed that the vortices that are shed from the top wall are also contributing to the turbulent intensity of the fluctuations in the wake of the top plate. The vortices at the bottom plate had only one distinct frequency, and the Strouhal number calculated with that frequency resulted in values that were in agreement with measurements conducted by Dellaert[8]. In the turbulent intensity spot in the near wake of

the top plate, multiple frequencies were found, that could only be the result of vortices shed from the top wall. The shedding of vortices from the top wall was confirmed by vorticity plots.

5.1.4 Effects of the side channel velocities

When varying the velocity of the side channels at a constant center channel velocity, it was found that for increased side channel velocities, the maximum turbulent intensity also increases and vice versa for decreased side channel velocities. Furthermore, large velocity differences between the center and side channels cause significantly more fluctuations in the domain. Side channel velocities at 75% to 80% of the center channel velocity are found to be optimal, as they result in less fluctuations in the channel. This is in contrast with results on measurements without conveyor belt in the experimental set-up conducted by Giesbergen[7]. Therefore, the results of this part of the numerical work should be verified experimentally.

5.1.5 Influence of the belt

Comparison of the simulations with a moving belt, with those with a stationary belt led to the conclusion that the inclusion of the bottom conveyor belt moving at a similar velocity as the average merged flow, results in more fluctuations in the domain. Van Vugt[9] observed the opposite in experiments, as the belt did reduce the fluctuations. As there is a difference between the dissipation of vortices in 2D flows and 3D turbulence, it is worthwhile to measure the flow field with the bottom conveyor belt experimentally without leakage.

Furthermore, it was found in the simulation that significantly less turbulent intensity is observed when either the bottom belt velocity is increased such that there is no velocity gradient near the belt. When a second belt is installed at the top wall moving at a similar velocity, the turbulent intensity is also reduced significantly. These two settings could be worthwhile to use in the experimental setup.

5.1.6 Plate thickness

The plate thickness influences the turbulent intensity generation in the wake of the splitter plates. Thinner plates result in significantly less turbulent intensity. Splitter plates with both rounded caps and triangular caps attached to their ends were also simulated. While rounded caps did not result in significant differences in turbulent intensity, it was found that triangular caps reduce the turbulent intensity significantly. Based on the results, it is worthwhile to install 10 cm long triangular caps on the splitter plates in the experimental set-up, as to reduce the turbulent intensity generated by these plates.

5.2 Experiments

5.2.1 Leakage

The leakage near the start of the conveyor belt was investigated and the implications on the flow in the bottom duct. The belt velocity had no significant effect on the leakage, but the flow velocity setting has an influence. A large leakage, up to 40%, was found for small flow velocity settings, which became less for increasing velocities. At 5 m/s velocity setting, only 13% of the fluid was lost. Lastly, a relation was found between the velocity setting and the average velocity in the bottom duct, that can be used to control the velocity in the bottom duct.

5.2.2 Cell honeycomb velocity

Measurements were performed in the direct wake of honeycomb 3, of which the cells hydraulic diameter was equal to 15.6 mm. As expected by theory, the laminar flow was not fully developed when exiting the honeycomb cells. Turbulent flows, however, emerge fully developed from the honeycomb cells, as was proven by comparison with DNS performed by Kuerten[32]. The measured turbulent intensity did also agree with the DNS, but near the walls the value of turbulent intensity measured was larger than the DNS. It could be worthwhile to investigate the development of the additional turbulent intensity further downstream of the honeycomb.

5.2.3 Flow in center duct

With the honeycomb removed from the center duct, the flow profile emerging from the center duct was measured. The velocity profiles showed that the flow is not fully developed for inlet velocities larger than 1 m/s. For both the 1 m/s and the 2 m/s velocity settings, the better developed half of the velocity profile was overlapping the DNS by Kuerten within the viscous sub-layer and the buffer layer, but it slightly diverged within the logarithmic layer. The undeveloped flow resulted in different turbulent intensity profiles.

5.3 Acknowledgements

During the project, the supervision was done by Jos Zeegers. I would like to thank him for the guidance and expertise. He also put tremendous effort in making me able to complete this graduation project despite some hardships with the experimental set-up. This effort is deeply appreciated.

I also would like to thank Leon Kamp and Cem Bingol for their insights shared during our meetings about the numerical work.

Furthermore, I would like to thank Rik Dellaert for helping me by getting the setup to work and teaching me how to measure with it, despite him being done with his PhD and working at a company outside of the university.

Lastly, I want to thank Hans Kuerten for providing the numerical simulations used in section 4.2. Without these simulations, I could not have analysed the experimental results discussed there.

Bibliography

- [1] Hannah Ritchie and Max Roser. Plastic pollution. <https://ourworldindata.org/plastic-pollution>, Sep 2018. 1
- [2] Andrej Patoski. Why is most plastic not recycled? - purpose rising blog. <https://repurpose.global/blog/post/why-is-most-plastic-not-recycled>, Jun 2019. 1
- [3] Quality of recycled plastic too poor. <https://www.technologist.eu/quality-of-recycled-plastic-too-poor/>, Apr 2019. 1
- [4] S. Tajfirooz. *Numerical Methods for Dynamics of Particles in Magnetized Liquids*. PhD thesis, Mechanical Engineering, February 2021. Proefschrift. 1
- [5] L.C. Thijs. Honeycomb wake turbulence and particle dynamics in a magnetic density separation system. *Master Thesis, Eindhoven University of Technology*, 2020. 2, 6, 11, 46
- [6] R.J.A. Driessen. Turbulence in the wake of a honeycomb. *Bachelor End Project, Eindhoven University of Technology*, 2021. 2, 11, 12, 13, 19, 23, 44, 46, 47, 53
- [7] M.T.A. Giesbergen. Characterizing turbulence in the wake of a honeycomb using Laser Doppler Velocimetry. *Bachelor End Project, Eindhoven University of Technology*, 2021. 2, 11, 19, 23, 29, 47, 54
- [8] R.A. Dellaert. Turbulence and particle behavior in a magnetic density separation application: Studied with LDV, PIV PTV. *PHD Thesis, Eindhoven University of Technology*, 2021. 2, 11, 14, 24, 38, 39, 42, 46, 47, 50, 53
- [9] M.A.M.M. van Vugt. Influence of a conveyor belt on flow in the wake of a honeycomb using Laser Doppler Velocimetry. *Bachelor End Project, Eindhoven University of Technology*, 2021. 2, 11, 15, 33, 39, 40, 44, 54
- [10] James R. Welty, Gregory L. Rorrer, and David G. Foster. *Fundamentals of momentum, heat, and Mass Transfer*. Wiley, 2021. 4
- [11] R.K. Shah and A.L. London. Rectangular ducts. *Laminar Flow Forced Convection in Ducts*, page 196–222, 1978. 6
- [12] Hua-Shu Dou and Boo Cheong Khoo. Investigation of turbulent transition in plane couette flows using energy gradient method. *Advances in Applied Mathematics and Mechanics*, 3(2):165–180, 2011. 7, 8
- [13] Pijush K. Kundu, Ira M. Cohen, David R. Dowling, and Tryggvason Gretar. *Fluid Mechanics. Pijush K. Kundu, Ira M. Cohen, David R. Dowling with contributions by Gretar Tryggvason*. Elsevier, 2016. 7, 8, 9, 10, 11, 13, 14
- [14] Bayode E. Owolabi, Robert J. Poole, and David J. Dennis. Experiments on low-reynolds-number turbulent flow through a square duct. *Journal of Fluid Mechanics*, 798:398–410, 2016. 7, 12, 13

- [15] R. W. Hanks and H. C. Ruo. Laminar-turbulent transition in ducts of rectangular cross section. *Industrial and Engineering Chemistry Fundamentals*, 5(4):558–561, 1966. 7, 42
- [16] L. Klotz, G. Lemoult, I. Frontczak, L. S. Tuckerman, and J. E. Wesfreid. Couette-poiseuille flow experiment with zero mean advection velocity: Subcritical transition to turbulence. *Physical Review Fluids*, 2(4), 2017. 8
- [17] Merle C. Potter. Stability of plane couette–poiseuille flow. *Journal of Fluid Mechanics*, 24(03):609, 1966. 8
- [18] Frans T.M Nieuwstadt, Bendiks J. Boersma, and Jerry Westerweel. *Turbulence: Introduction to theory and applications of turbulent flows*. Springer, 2016. 8, 9, 11
- [19] Cengel Yunus A. and John M. Cimbala. *Fluid Mechanics: Fundamentals and Applications*. McGraw-Hill Higher Education, 2006. 11
- [20] Sergio Pirozzoli, Davide Modesti, Paolo Orlandi, and Francesco Grasso. Turbulence and secondary motions in square duct flow. *Journal of Fluid Mechanics*, 840:631–655, 2018. 12
- [21] A. Mellling and J. H. Whitelaw. Turbulent flow in a rectangular duct. *Journal of Fluid Mechanics*, 78(2):289–315, 1976. 12
- [22] D. Modesti. Private communication. 2020. 12, 13
- [23] H. Zhang. Direct numerical simulation of a fully developed turbulent duct flow up to $Re=1200$. *Int. Journal of Heat and Fluid Flow*, 2015. 12, 13
- [24] J.M.G. Kuerten. Private communication. 2020. 12, 13
- [25] Finite difference schemes. <https://www.mech.kth.se/ardeshir/courses/literature/fd.pdf>. 13
- [26] <https://www.brockmann-consult.de/CloudStructures/kelvin-helmholtz-instability-description.htm>. 13
- [27] Sadatoshi Taneda. Experimental investigation of the wakes behind cylinders and plates at low reynolds numbers. *Journal of the Physical Society of Japan*, 11(3):302–307, 1956. 14
- [28] A. Blazewicz, M. Bull, and R. Kelso. Characteristics of flow regimes for single plates of rectangular cross-section. 12 2007. 14
- [29] Nicholas T. Ouellette. Turbulence in two dimensions. *Physics Today*, 65(5):68–69, 2012. 33
- [30] I. Bruining. Decay of wake turbulence generated by honeycombs for magnetic density separation. *Bachelor End Project, Eindhoven University of Technology*, 2018. 37
- [31] TSI. *Phase Doppler Particle Analyzer (PDPA)/ Laser Doppler Velocimeter (LDV): Operations Manual*, volume Revision F. February 2008. 40
- [32] J.M.G. Kuerten. Private communication. 2022. 46, 47, 48, 49, 50, 51, 55

Appendix A

Derivation equation 2.16 from equation 2.15.

$$u_p(y, z) = -\frac{16a^2}{\pi^3 \rho} \frac{\partial p}{\partial x} \sum_{n=1,3,5,\dots}^{\infty} \frac{1}{n^3} (-1)^{(n-1)/2} \left(1 - \frac{\cosh n\pi z/(2a)}{\cosh n\pi b/(2a)} \right) \cos\left(\frac{n\pi y}{2a}\right) \quad (\text{A.1})$$

$$u_{P,avg} = \frac{\int_{-a}^a \int_{-b}^b u_p dz dy}{4ab} \quad (\text{A.2})$$

$$u_{P,avg} = -\frac{16a^2}{\pi^3 \rho} \frac{\partial p}{\partial x} \frac{1}{4ab} \sum_{n=1,3,5,\dots}^{\infty} \frac{1}{n^3} (-1)^{(n-1)/2} \left(z - \frac{2a \sinh n\pi z/(2a)}{n\pi \cosh n\pi b/(2a)} \right) \frac{2a}{n\pi} \sin\left(\frac{n\pi y}{2a}\right) \Big|_{y=-a}^a \Big|_{z=-b}^b \quad (\text{A.3})$$

$$(-1)^{(n-1)/2} \sin\left(\frac{n\pi y}{2a}\right) \Big|_{y=-a}^a = 2 : n = 1, 3, 5, \dots \quad (\text{A.4})$$

$$\left(z - \frac{2a \sinh n\pi z/(2a)}{n\pi \cosh n\pi b/(2a)} \right) \Big|_{z=-b}^b = 2 \left(b - \frac{2a}{n\pi} \tanh\left(\frac{n\pi b}{2a}\right) \right) \quad (\text{A.5})$$

$$u_{P,avg} = -\frac{16a^2}{\pi^3 \rho} \frac{\partial p}{\partial x} \frac{1}{4ab} \sum_{n=1,3,5,\dots}^{\infty} \frac{1}{n^4} \left(b - \frac{2a}{n\pi} \tanh\left(\frac{n\pi b}{2a}\right) \right) \frac{8a}{\pi} \quad (\text{A.6})$$

$$u_{P,avg} = -\frac{16a^2}{\pi^3 \rho} \frac{\partial p}{\partial x} \sum_{n=1,3,5,\dots}^{\infty} \frac{1}{n^4} \left(1 - \frac{2a}{n\pi b} \tanh\left(\frac{n\pi b}{2a}\right) \right) \frac{2}{\pi} \quad (\text{A.7})$$

$$-\frac{16a^2}{\pi^3 \rho} \frac{\partial p}{\partial x} = u_{P,avg} / \left(\frac{2}{\pi} \sum_{n=1,3,5,\dots}^{\infty} \frac{1}{n^4} \left(1 - \frac{2a}{n\pi b} \tanh\left(\frac{n\pi b}{2a}\right) \right) \right) \quad (\text{A.8})$$

$$u_p(y, z) = u_{P,avg} \frac{\sum_{n=1,3,5,\dots}^{\infty} \frac{1}{n^3} (-1)^{(n-1)/2} \left(1 - \frac{\cosh(n\pi z/2a)}{\cosh(n\pi b/2a)} \right) \cos\left(\frac{n\pi y}{2a}\right)}{\frac{2}{\pi} \sum_{n=1,3,5,\dots}^{\infty} \frac{1}{n^4} \left(1 - \frac{2a}{n\pi b} \tanh\left(\frac{n\pi b}{2a}\right) \right)}, \quad (\text{A.9})$$

Appendix B

Matlab scripts

B.1 Matlab script used in section 4.2

```
1 clear
2 close all
3 clc
4
5 %%
6 Dh=5/3; %hydraulic diameter of the duct
7 mu=Dh/7737; %
8 stat1=load('stat7737.dat'); % loading the DNS simulation
9 n=sqrt(length(stat1(:,1))); %defined such to reshape any square matrix.
10 n2=n/2;
11 stat=reshape(stat1,n,n,11);
12 x=stat(:,:,1);
13 y=stat(:,:,2);
14 uz=stat(:,:,5);
15 uy=stat(:,:,4);
16 ux=stat(:,:,3);
17 rmsuzold=stat(:,:,8);
18 rmsuyold=stat(:,:,7);
19 rmsuxold=stat(:,:,6);
20 uav=(uz(1:n-1,1:n-1)+uz(2:n,1:n-1)+uz(2:n,2:n)+uz(1:n-1,2:n))/4;
21 area=(x(2:n,2:n)-x(1:n-1,1:n-1)).*(y(2:n,2:n)-y(1:n-1,1:n-1));
22 Ub=sum(sum(area.*uav))/sum(sum(area));
23 Re_b=Dh*Ub/mu;
24 disp(Re_b)
25 uzold=uz;
26 yold=y;
27 WFu=sqrt((uz(n2,1)-uz(n2,2))/(y(n2,1)-y(n2,2))*mu); %wall friction velocity
28 uplus=uz(n2,1:n2)/Wfu; % velocity plus unit
29 yplus=y(n2,1:n2)*Wfu/mu; % wall unit
30 n2old=n2;
31 % similar but now for the other simulation
32 mu2=Dh/3868;
33 stat2=load('stat3868.dat');
34 n=sqrt(length(stat2(:,1)));
35 n2=n/2;
36 stat=reshape(stat2,n,n,11);
37 x=stat(:,:,1);
38 y=stat(:,:,2);
39 uz=stat(:,:,5);
40 uy=stat(:,:,4);
41 ux=stat(:,:,3);
42 rmsuz=stat(:,:,8);
43 rmsuy=stat(:,:,7);
44 rmsux=stat(:,:,6);
45 Ruv=stat(:,:,9);
46 Rvw=stat(:,:,10);
```

```

47 Ruw=stat(:, :, 11);
48 uav=(uz(1:n-1,1:n-1)+uz(2:n,1:n-1)+uz(2:n,2:n)+uz(1:n-1,2:n))/4;
49 area=(x(2:n,2:n)-x(1:n-1,1:n-1)).*(y(2:n,2:n)-y(1:n-1,1:n-1));
50 Ub=sum(sum(area.*uav))/sum(sum(area));
51 Re_b2=Dh*Ub/mu2;
52 disp(Re_b2)
53 WFu2=sqrt((uz(n2,1)-uz(n2,2))/(y(n2,1)-y(n2,2))*mu2);
54 uplus2=uz(n2,1:n2)/WFu2;
55 yplus2=y(n2,1:n2)*WFu2/mu2;
56 yval=find(yplus(2:length(yplus))>1/0.39*log(yplus(2:length(yplus)))/log(exp(1))
57 +5,1);
58 yval2=find(yplus2(2:length(yplus2))>1/0.39*log(yplus2(2:length(yplus2)))/log(exp(1))
59 +5,1);
60 %%plots of the wall units
61 figure(68)
62 semilogx(yplus, uplus, '-k', 'linewidth', 1)
63 set(gca, 'FontSize', 12, 'xcolor', 'k', 'ycolor', 'k')
64 set(groot, {'DefaultAxesXColor', 'DefaultAxesYColor', 'DefaultAxesZColor'}, {'k', 'k', 'k'})
65 xlabel('$z^+$', 'fontsize', 20, 'Interpreter', 'Latex')
66 ylabel('$u^+$', 'fontsize', 20, 'Interpreter', 'Latex')
67 %xlim([min(min(x)) max(max(x))])
68 %ylim([min(min(uz)) max(max(uz))])
69 axis square
70 grid on
71 hold on
72
73 figure(69)
74 semilogx(yplus2, uplus2, '-k', 'linewidth', 1)
75 set(gca, 'FontSize', 12, 'xcolor', 'k', 'ycolor', 'k')
76 set(groot, {'DefaultAxesXColor', 'DefaultAxesYColor', 'DefaultAxesZColor'}, {'k', 'k', 'k'})
77 xlabel('$z^+$', 'fontsize', 20, 'Interpreter', 'Latex')
78 ylabel('$u^+$', 'fontsize', 20, 'Interpreter', 'Latex')
79 %xlim([min(min(x)) max(max(x))])
80 %ylim([min(min(uz)) max(max(uz))])
81 axis square
82 grid on
83 hold on
84
85 %% Loading the measurement data
86 opts = delimitedTextImportOptions(" NumVariables", 9);
87 opts.DataLines = [2, Inf];
88 opts.Delimiter = ",";
89 opts.VariableNames = ["Var1", "TransVelMeanCh2msec", "Var3", "TransVelRMSCh1msec",
90 "TransVelRMSCh2msec", "TransVelRMSCh3msec", "Var7", "Var8", "ZAxisPosition"];
91 opts.SelectedVariableNames = ["TransVelMeanCh2msec", "TransVelRMSCh1msec",
92 "TransVelRMSCh2msec", "TransVelRMSCh3msec", "ZAxisPosition"];
93 opts.VariableTypes = ["string", "double", "string", "double", "double", "double", "double", "string", "string", "double"];
94 opts.ExtraColumnsRule = "ignore";
95 opts.EmptyLineRule = "read";
96 opts = setvaropts(opts, ["Var1", "Var3", "Var7", "Var8"], "WhitespaceRule", "preserve");
97 opts = setvaropts(opts, ["Var1", "Var3", "Var7", "Var8"], "EmptyFieldRule", "auto");
98 vell = table2array(readtable("C:\Users\20165294\OneDrive - TU Eindhoven\Documents\
99 TRANSFER CC3.08\uitwerking\centerchannel\validationvellinstantmerged.csv", opts));
100 clear opts
101 opts = delimitedTextImportOptions(" NumVariables", 9);
102 opts.DataLines = [2, Inf];
103 opts.Delimiter = ",";
104 opts.VariableNames = ["Var1", "TransVelMeanCh2msec", "Var3", "TransVelRMSCh1msec",
105 "TransVelRMSCh2msec", "TransVelRMSCh3msec", "Var7", "Var8", "ZAxisPosition"];

```

```

102 | opts.SelectedVariableNames = ["TransVelMeanCh2msec", "TransVelRMSCh1msec", "
      | TransVelRMSCh2msec", "TransVelRMSCh3msec", "ZAxisPosition"];
103 | opts.VariableTypes = ["string", "double", "string", "double", "double", "double", "
      | string", "string", "double"];
104 | opts.ExtraColumnsRule = "ignore";
105 | opts.EmptyLineRule = "read";
106 | opts = setvaropts(opts, ["Var1", "Var3", "Var7", "Var8"], "WhitespaceRule", "
      | preserve");
107 | opts = setvaropts(opts, ["Var1", "Var3", "Var7", "Var8"], "EmptyFieldRule", "auto");
108 | vel2 = table2array(readtable("C:\Users\20165294\OneDrive - TU Eindhoven\Documents\
      | TRANSFER CC3.08\uitwerking\centerchannel\validationvel2instantmerged.csv", opts
      | ));
109 | clear opts
110 |
111 | %Converting data to wall units to plot in the figures.
112 | vel11=vel1(17:117,:);
113 | vel21=vel2(17:117,:);
114 | correction=-yplus(2)/(Wfu/mu); % 1 z-unit length in mm, which is used to shift the
      | curve.
115 | vel11(:,5)=(vel11(:,5)-(min(vel11(:,5))+max(vel11(:,5)))/2)/25*(5/7)+3.5*correction
      | ; % correcting for 1.5 z-units in mm
116 | vel21(:,5)=(vel21(:,5)-(min(vel21(:,5))+max(vel21(:,5)))/2)/25*(5/7)+0.5*correction
      | ; % correcting for 0.5 z-units in mm
117 | y1plus=vel11(:,5)*0;
118 | y2plus=vel11(:,5)*0;
119 | vel2plus=vel11(:,1)/Wfu2;
120 | vel2plus(52:101)=vel11(101:-1:52,1)/Wfu2;
121 | y2plus(1:51)=(vel11(1:51,5)+5/7)*Wfu2/mu2;
122 | y2plus(52:101)=(5/7-vel11(101:-1:52,5))*Wfu2/mu2;
123 | vel1plus=vel21(:,1)/Wfu;
124 | vel1plus(52:101)=vel21(101:-1:52,1)/Wfu;
125 | y1plus(1:51)=(vel21(1:51,5)+5/7)*Wfu/mu;
126 | y1plus(52:101)=(5/7-vel21(101:-1:52,5))*Wfu/mu;
127 | % finalizing the figures
128 | figure(69)
129 | plot(y2plus((52:101)), vel2plus((52:101)), '.', 'MarkerSize', 10)
130 | plot(yplus2(1:yval2+1), yplus2(1:yval2+1), '-k', 'linewidth', 1)
131 | plot(yplus2(yval2-1:n2), 1/0.39*log(yplus2(yval2-1:n2))/log(exp(1))+5, '-k',
      | 'linewidth', 1)
132 | saveas(gcf, 'Re3868wallunits.png')
133 |
134 | figure(68)
135 | plot(y1plus((1:51)), vel1plus((1:51))/2, '.', 'MarkerSize', 10)
136 | plot(yplus(1:yval+1), yplus(1:yval+1), '-k', 'linewidth', 1)
137 | plot(yplus(yval-1:n2old), 1/0.39*log(yplus(yval-1:n2old))/log(exp(1))+5, '-k',
      | 'linewidth', 1)
138 | saveas(gcf, 'Re7737wallunits.png')
139 |
140 | %Velocity plots (1 and 2) and turbulent intensity plots (3 and 4)
141 | figure(1)
142 | plot(vel1(16:118,1), vel1(16:118,5)-(min(vel1(16:118,5))+max(vel1(16:118,5)))/2,
      | 'color', [0.8500 0.3250 0.0980], 'linewidth', 1)
143 | set(gca, 'FontSize', 12, 'xcolor', 'k', 'ycolor', 'k')
144 | set(groot, {'DefaultAxesXColor', 'DefaultAxesYColor', 'DefaultAxesZColor'}, {'k', 'k', 'k'
      | })
145 | ylabel('$z$ (mm)', 'fontsize', 20, 'Interpreter', 'Latex')
146 | xlabel('$u$ (m/s)', 'fontsize', 20, 'Interpreter', 'Latex')
147 | %xlim([min(min(x)) max(max(x))])
148 | %ylim([min(min(uz)) max(max(uz))])
149 | axis square
150 | grid on
151 | hold on
152 | plot(uz(n2, 1:n), (y(n, 1:n)-5/7)*35, 'k', 'linewidth', 1)
153 | saveas(gcf, 'Re3868velocity.png')
154 |
155 | figure(2)

```

```

156 | plot(vel2(16:118,1),vel2(16:118,5)-(min(vel2(16:118,5))+max(vel2(16:118,5)))/2,'
      |     color',[0.8500 0.3250 0.0980],'linewidth',1)
157 | set(gca,'FontSize',12,'xcolor','k','ycolor','k')
158 | set(groot',{'DefaultAxesXColor','DefaultAxesYColor','DefaultAxesZColor'},{'k','k','k'
      |     })
159 | ylabel('$z$ (mm)','fontsize',20,'Interpreter','Latex')
160 | xlabel('$u$ (m/s)','fontsize',20,'Interpreter','Latex')
161 | %xlim([min(min(x)) max(max(x))])
162 | %ylim([min(min(uz)) max(max(uz))])
163 | axis square
164 | grid on
165 | hold on
166 | plot(uzold(n2,1:n)*2,(yold(n,1:n)-5/7)*35,'k','linewidth',1)
167 | saveas(gcf,'Re7737velocity.png')
168 |
169 | figure(3)
170 | plot(sqrt(1/3*(vel1(16:118,2).^2+vel1(16:118,3).^2+vel1(16:118,4).^2)),vel1
      |     (16:118,5)-(min(vel1(16:118,5))+max(vel1(16:118,5)))/2,'color',[0.8500 0.3250
      |     0.0980],'linewidth',1)
171 | set(gca,'FontSize',12,'xcolor','k','ycolor','k')
172 | set(groot',{'DefaultAxesXColor','DefaultAxesYColor','DefaultAxesZColor'},{'k','k','k'
      |     })
173 | ylabel('$z$ (mm)','fontsize',20,'Interpreter','Latex')
174 | xlabel('$I$','fontsize',20,'Interpreter','Latex')
175 | %xlim([min(min(x)) max(max(x))])
176 | %ylim([min(min(uz)) max(max(uz))])
177 | axis square
178 | grid on
179 | hold on
180 | plot(sqrt(1/3*(rmsuxold(n2,1:n).^2+rmsuyold(n2,1:n).^2+rmsuzold(n2,1:n).^2)),(y(n
      |     ,1:n)-5/7)*35,'k','linewidth',1)
181 | saveas(gcf,'Re3868TI.png')
182 |
183 | figure(4)
184 | plot(sqrt(1/3*(vel2(16:118,2).^2+vel2(16:118,3).^2+vel2(16:118,4).^2))/2,vel2
      |     (16:118,5)-(min(vel2(16:118,5))+max(vel2(16:118,5)))/2,'color',[0.8500 0.3250
      |     0.0980],'linewidth',1)
185 | set(gca,'FontSize',12,'xcolor','k','ycolor','k')
186 | set(groot',{'DefaultAxesXColor','DefaultAxesYColor','DefaultAxesZColor'},{'k','k','k'
      |     })
187 | ylabel('$z$ (mm)','fontsize',20,'Interpreter','Latex')
188 | xlabel('$I$','fontsize',20,'Interpreter','Latex')
189 | %xlim([min(min(x)) max(max(x))])
190 | %ylim([min(min(uz)) max(max(uz))])
191 | axis square
192 | grid on
193 | hold on
194 | plot(sqrt(1/3*(rmsux(n2,1:n).^2+rmsuy(n2,1:n).^2+rmsuz(n2,1:n).^2)),(y(n,1:n)-5/7)
      |     *35,'k','linewidth',1)
195 | saveas(gcf,'Re7737TI.png')
196 | % calculating the z-unit lengths that were displayed in the report
197 | zunitlength=mu/WFu*0.025;
198 | zunitlength2=mu2/WFu2*0.025;
199 | disp(zunitlength)
200 | disp(zunitlength2)

```

B.2 Matlab scripts laminar flow

```

1  % This script computes the solution of a fully developed laminar duct flow
   % profile described in section 2.2.2 based on the dimensions of the duct, average
   % velocity and belt velocity.
2
3  clear all
4  close all
5  clc
6  height=0.01; %height duct
7  width=0.07; %width duct
8  b=height/2;
9  a=width/2;
10 gridpoints=100; %total (2*gridpoints+1)^2
11 y=-a:a/gridpoints:a;
12 z=-b:b/gridpoints:b;
13 y= repmat(y',1,2*gridpoints+1);
14 z= repmat(z,2*gridpoints+1,1);
15
16 N=round(200*a/b); %keep this at max at 200*b/a
17 upp=z*0;
18 upd=0;
19 uc=upp;
20 ucavg=0;
21 tic
22 %% Loop below contains the theoretical solution described in section 2.2.2.
23 for n=1:2:N
24     upp=upp+(-1)^((n-1)/2)*(1-cosh(n*pi*z/(2*a))/cosh(n*pi*b/(2*a))).*cos(n*pi*y
        /(2*a))/n^3;
25     upd=upd+2/pi*1/n^4*(1-2*a/(n*pi*b)*tanh(n*pi*b/(2*a)));
26     uc=uc+4/pi*1/n*sinh(n*pi*(-z+b)/(2*a))/sinh(n*pi*b/a).*sin(n*pi*(y+a)/(2*a));
27     ucavg=ucavg+8*a/(pi^3*b)*1/n^3*(1/tanh(n*pi*b/a)-1/sinh(n*pi*b/a));
28 end
29 %% Loops below have hyperbolic terms expanded as they became to small for matlab to
   % compute without errors.
30 for n=N+1+rem(N,2):2:round(150*N*b/a)
31     upp=upp+(-1)^((n-1)/2)*(1-exp(n*pi*(z-b)/(2*a))-exp(n*pi*(-z-b)/(2*a))).*cos(n*
        pi*y/(2*a))/n^3;
32     uc=uc+4/pi*1/n*(exp(n*pi*(-z-b)/(2*a))-exp(n*pi*(z-3*b)/(2*a))).*sin(n*pi*(y+a)
        /(2*a));
33 end
34 toc
35 tic
36 for n=N+1+rem(N,2):2:round(1000*N*b/a)
37     upd=upd+2/pi*1/n^4*(1-2*a/(n*pi*b)*tanh(n*pi*b/(2*a)));
38     ucavg=ucavg+8*a/(pi^3*b)*1/n^3*(1/tanh(n*pi*b/a)-1/sinh(n*pi*b/a));
39 end
40 toc
41 %% plot
42 Uboundary=0; %% belt velocity
43 Uaverage=1; %%Uboundary*ucavg for Couette flow
44 ucnet=uc.*Uboundary;
45 ucavgnet=ucavg*Uboundary;
46 u=ucnet+(Uaverage-ucavgnet)*upp/upd; %equation 2.21
47 uaverageout=sum(sum(u))/(2*gridpoints)^2;
48 urat=max(u)/Uaverage;
49
50 close all
51 sizefigure=330;
52 figure
53 set(gca,'FontSize',15,'xcolor','k','ycolor','k')
54 set(groot,{'DefaultAxesXColor','DefaultAxesYColor','DefaultAxesZColor'},{'k','k','k'
        })
55 surface(y+a,z+b,u)
56 shading interp
57 grid()
58 colormap(jet)

```



```

59 xlabel('y$ (m)', 'Interpreter', 'Latex', 'FontSize', 25);
60 ylabel('z$ (m)', 'Interpreter', 'Latex', 'FontSize', 25);
61 h = colorbar;
62 ylabel(h, '$u(y,z)$ (m/s)', 'Interpreter', 'Latex', 'FontSize', 25)
63 set(gcf, 'units', 'points', 'position', [0,50, sizefigure*min([a/b 5])+100, sizefigure])
64 xlim([0, 2*a])
65 ylim([0, 2*b])
66 %saveas(gcf, 'savename.png')
67
68 figure
69 contour(y+a, z+b, u, 20, 'linewidth', 1)
70 set(gca, 'FontSize', 15, 'xcolor', 'k', 'ycolor', 'k')
71 set(root, {'DefaultAxesXColor', 'DefaultAxesYColor', 'DefaultAxesZColor'}, {'k', 'k', 'k'})
72 shading interp
73 grid()
74 colormap(jet)
75 xlabel('y$ (m)', 'Interpreter', 'Latex', 'FontSize', 25);
76 ylabel('z$ (m)', 'Interpreter', 'Latex', 'FontSize', 25);
77 h = colorbar;
78 ylabel(h, '$u(y,z)$ (m/s)', 'Interpreter', 'Latex', 'FontSize', 25)
79 set(gcf, 'units', 'points', 'position', [0,50, sizefigure*min([a/b 5])+100, sizefigure])
80 [ymax, zmax]=find(u==max(max(u(:,:))));
81 %saveas(gcf, 'savename2.png')
82
83 figure
84 plot(y(:, zmax(ceil(length(zmax)/2))+a), u(:, zmax(ceil(length(zmax)/2))), 'DisplayName',
      strcat('$z$ = $ $', num2str(max(z(:, zmax(ceil(length(zmax)/2)))*1000)+1000*b),
      '$\cdot 10^{-3}$', ' m'))
85 grid()
86 xlabel('$u(y)$ (m)', 'Interpreter', 'Latex', 'FontSize', 20);
87 ylabel('$y$ (m)', 'Interpreter', 'Latex', 'FontSize', 20);
88 axis square
89 xlim([0, 2*a])
90 legend('show', 'Interpreter', 'Latex', 'FontSize', 16, 'Location', 'south')

```

```

1 % This script computes the solution of equation 2.12 based on the dimensions of
2   the duct, belt velocity and the streamwise pressure gradient.
3 clear all
4 close all
5 clc
6
7 a=0.0156;
8 b=0.0156;
9 mu=1.508e-5; viscosity of the gas
10 dpdx=-4; %Streamwise pressure gradient in order to get an Poisseuille flow.
11 Ubelt=0; %Belt speed
12 pointsy=100; % Points in the y-direction, matrix scales as (pointsy+pointsz)^2
13 pointsz=100; % Points in the z-direction, matrix scales as (pointsy+pointsz)^2.
14 z=(0:1/pointsz:1)*b;
15 y=(0:1/pointsy:1)*a;
16 dz=z(2)-z(1);
17 dy=y(2)-y(1);
18 %Boundary conditions
19 z0=Ubelt;
20 z1=0;
21 y0=0;
22 y1=0;
23 L=dpdx/mu; %constant, commonly denoted as \eta in literature
24 %% Centre of domain
25 bmatrix=-dz^2*dy^2/(30/12*dz^2+30/12*dy^2)*L*ones(length(y)*length(z),1);
26 matrix=16/12*diag(ones(length(y)*length(z)-1,1),1)*dz^2/(30/12*dz^2+30/12*dy^2);
27 matrix=matrix+16/12*diag(ones(length(y)*length(z)-1,1),-1)*dz^2/(30/12*dz^2+30/12*
28   dy^2);
29 matrix=matrix-1/12*diag(ones(length(y)*length(z)-2,1),2)*dz^2/(30/12*dz^2+30/12*dy
30   ^2);
31 matrix=matrix-1/12*diag(ones(length(y)*length(z)-2,1),-2)*dz^2/(30/12*dz^2+30/12*dy
32   ^2);
33 matrix=matrix+16/12*diag(ones(length(y)*length(z)-length(y),1),length(y))*dy
34   ^2/(30/12*dz^2+30/12*dy^2);
35 matrix=matrix+16/12*diag(ones(length(y)*length(z)-length(y),1),-length(y))*dy
36   ^2/(30/12*dz^2+30/12*dy^2);
37 matrix=matrix-1/12*diag(ones(length(y)*length(z)-2*length(y),1),2*length(y))*dy
38   ^2/(30/12*dz^2+30/12*dy^2);
39 matrix=matrix-1/12*diag(ones(length(y)*length(z)-2*length(y),1),-2*length(y))*dy
40   ^2/(30/12*dz^2+30/12*dy^2);
41 %% z-boundaries
42 matrix(1:2*length(y),:)=0;
43 matrix(length(y)*(length(z)-2)+1:length(y)*(length(z)),:)=0;
44 for j=1:length(y)
45   matrix(j+length(y),j)=dy^2/(2*dz^2+2*dy^2);
46   matrix(j+length(y),j+2*length(y))=dy^2/(2*dz^2+2*dy^2);
47   matrix(j+length(y),j+length(y)+1)=dz^2/(2*dz^2+2*dy^2);
48   matrix(j+length(y),j+length(y)-1)=dz^2/(2*dz^2+2*dy^2);
49   bmatrix(j+length(y))=-dz^2*dy^2/(2*dz^2+2*dy^2)*L;
50   matrix(j+length(y)*(length(z)-2),j+length(y)*(length(z)-3))=dy^2/(2*dz^2+2*dy
51     ^2);
52   matrix(j+length(y)*(length(z)-2),j+2*length(y)+length(y)*(length(z)-3))=dy
53     ^2/(2*dz^2+2*dy^2);
54   matrix(j+length(y)*(length(z)-2),j+length(y)+1+length(y)*(length(z)-3))=dz
55     ^2/(2*dz^2+2*dy^2);
56   matrix(j+length(y)*(length(z)-2),j+length(y)-1+length(y)*(length(z)-3))=dz
57     ^2/(2*dz^2+2*dy^2);
58   bmatrix(j+length(y)*(length(z)-2))=-dz^2*dy^2/(2*dz^2+2*dy^2)*L;
59 end
60 bmatrix(1:length(y))=z0;
61 bmatrix(length(y)*(length(z)-1)+1:length(y)*(length(z)),:)=z1;
62 %% y-boundaries
63 for k=2:length(z)-1
64   matrix(1+(k-1)*length(y),:)=0;
65   matrix((k)*length(y),:)=0;
66   bmatrix(1+(k-1)*length(y),:)=y0;
67   bmatrix((k)*length(y),:)=y1;

```

```

56     matrix(2+(k-1)*length(y),:)=0;
57     matrix(2+(k-1)*length(y),2+(k-2)*length(y))=dy^2/(2*dz^2+2*dy^2);
58     matrix(2+(k-1)*length(y),2+(k)*length(y))=dy^2/(2*dz^2+2*dy^2);
59     matrix(2+(k-1)*length(y),1+(k-1)*length(y))=dz^2/(2*dz^2+2*dy^2);
60     matrix(2+(k-1)*length(y),3+(k-1)*length(y))=dz^2/(2*dz^2+2*dy^2);
61     matrix((k)*length(y)-1,:)=0;
62     matrix(k*length(y)-1,(k-1)*length(y)-1)=dy^2/(2*dz^2+2*dy^2);
63     matrix(k*length(y)-1,(k+1)*length(y)-1)=dy^2/(2*dz^2+2*dy^2);
64     matrix(k*length(y)-1,k*length(y))=dz^2/(2*dz^2+2*dy^2);
65     matrix(k*length(y)-1,k*length(y)-2)=dz^2/(2*dz^2+2*dy^2);
66     bmatrix(2+(k-1)*length(y),:)= -dz^2*dy^2/(2*dz^2+2*dy^2)*L;
67     bmatrix((k)*length(y)-1,:)= -dz^2*dy^2/(2*dz^2+2*dy^2)*L;
68 end
69 %% corner boundaries
70 bmatrix(1)=(y0+z0)/(2);
71 bmatrix(length(y))=(y1+z0)/(2);
72 bmatrix(1+(length(z)-1)*length(y))=(y0+z1)/(2);
73 bmatrix(length(z)*length(y))=(y1+z1)/(2);
74 %% finalisation and solution
75 matrix=matrix-eye(length(y)*length(z));
76 bmatrix=bmatrix*-1;
77 uout=matrix^-1*bmatrix;
78 uout=reshape(uout,[length(y),length(z)]);
79 uaverage=sum(sum(uout(:,:)))/(length(z)-1)/(length(y)-1);
80 umax=max(max(uout(:,:)));
81 urat=umax/uaverage;
82 disp('average')
83 disp(uaverage)
84 disp('rat')
85 disp(urat)
86 %% plot
87 figure
88 surface(y,z,transpose(uout))
89 shading interp
90 grid()
91 colormap(jet)
92 xlabel('$y$ (m)', 'Interpreter', 'Latex', 'FontSize', 20);
93 ylabel('$z$ (m)', 'Interpreter', 'Latex', 'FontSize', 20);
94 h = colorbar;
95 ylabel(h, '$u(y,z)$ (m/s)', 'Interpreter', 'Latex', 'FontSize', 20)
96 axis square
97 %saveas(gcf,'colorplotname.png')
98 figure
99 contour(y,z,transpose(uout),20)
100 shading interp
101 grid()
102 colormap(jet)
103 xlabel('$y$ (m)', 'Interpreter', 'Latex', 'FontSize', 20);
104 ylabel('$z$ (m)', 'Interpreter', 'Latex', 'FontSize', 20);
105 h = colorbar;
106 ylabel(h, '$u(y,z)$ (m/s)', 'Interpreter', 'Latex', 'FontSize', 20)
107 axis square
108 %saveas(gcf,'contourplotname.png')
109 %% clearing matrix for memory
110 clear matrix bmatrix
111 %%
112 [ymax,zmax]=find(uout==max(max(uout(:,:))));
113 figure
114 plot(y,uout(:,zmax(ceil(length(zmax)/2))), 'DisplayName',strcat('$z$ = $ $', num2str(
    max(z(zmax))*1000), '$\cdot 10^{-3}$', 'm'))
115 grid()
116 ylabel('$u(y)$ (m)', 'Interpreter', 'Latex', 'FontSize', 20);
117 xlabel('$y$ (m)', 'Interpreter', 'Latex', 'FontSize', 20);
118 axis square
119 legend('show', 'Interpreter', 'Latex', 'FontSize', 16, 'Location', 'south')

```

B.3 Matlab script for determination leakage for different belt velocities.

```

1 clear
2 close all
3 clc
4 height=0.007;
5 width=0.07;
6 b=height/2;
7 a=width/2;
8 gridpoints=500; %total (2*gridpoints+1)^2
9 y=-a:a/gridpoints:a;
10 z=-b:b/gridpoints:b;
11 y= repmat(y',1,2*gridpoints+1);
12 z= repmat(z,2*gridpoints+1,1);
13
14 N=round(200*a/b); %keep this at max at 200*b/a
15 upp=z*0;
16 upd=0;
17 uc=upp;
18 ucavg=0;
19 tic
20 for n=1:2:N
21     upp=upp+(-1)^((n-1)/2)*(1-cosh(n*pi*z/(2*a))/cosh(n*pi*b/(2*a))).*cos(n*pi*y
22         /(2*a))/n^3;
23     upd=upd+2/pi*1/n^4*(1-2*a/(n*pi*b)*tanh(n*pi*b/(2*a)));
24     uc=uc+4/pi*1/n*sinh(n*pi*(-z+b)/(2*a))/sinh(n*pi*b/a).*sin(n*pi*(y+a)/(2*a));
25     ucavg=ucavg+8*a/(pi^3*b)*1/n^3*(1/tanh(n*pi*b/a)-1/sinh(n*pi*b/a));
26 end
27 for n=N+1:rem(N,2):2:round(150*N*b/a)
28     upp=upp+(-1)^((n-1)/2)*(1-exp(n*pi*(z-b)/(2*a))-exp(n*pi*(-z-b)/(2*a))).*cos(n*
29         pi*y/(2*a))/n^3;
30     uc=uc+4/pi*1/n*(exp(n*pi*(-z-b)/(2*a))-exp(n*pi*(z-3*b)/(2*a))).*sin(n*pi*(y+a)
31         /(2*a));
32 end
33 toc
34 for n=N+1:rem(N,2):2:round(1000*N*b/a)
35     upd=upd+2/pi*1/n^4*(1-2*a/(n*pi*b)*tanh(n*pi*b/(2*a)));
36     ucavg=ucavg+8*a/(pi^3*b)*1/n^3*(1/tanh(n*pi*b/a)-1/sinh(n*pi*b/a));
37 end
38 %% Calculation of the average velocity based on the data.
39 tabletoread='bottomchannelvel1Ubelt1000.csv';
40 measurementheight=0.004;
41 mheight=round(measurementheight/(2*b)*(2*gridpoints+1));
42 T=readtable(tabletoread);
43 disp(tabletoread)
44 T=table2array(T);
45 yuncertainty=round(1e-2/a*gridpoints);
46 zuncertainty=round(5e-4/b*gridpoints);
47
48 data=T(:,[7 2 5]);
49 data(:,1)=(data(:,1)-min(data(:,1)))/1000;
50 datmin=find(data(:,1)>=1e-2,1);
51 datplus=find(data(:,1)<=2e-2,1,'last');
52 um=data(datmin:datplus,2);
53 umstd=data(datmin:datplus,3);
54 dat1=data(datmin:datplus,1);
55 ypoints=zeros(length(datmin:datplus),1);
56 for i=1:-datmin+datplus+1
57     ypoints(i)=find(abs(y(:,3)-dat1(i))==min(abs(y(:,3)-dat1(i))));
58 end
59 Voltage=input(" Voltage (mV): ");
60

```

```

61 %calculating the velocity based on the measurements in each point.
62 Uboundary=3.36e-3*Voltage+0.01;
63 if Voltage==0
64     Uboundary=input(" Uboundary (m/s):      ");
65     Voltage=(Uboundary-0.01)/3.36e-3;
66 end
67 ucnet=uc.*Uboundary;
68 ucavgnet=ucavg*Uboundary;
69 ucout=ucnet(ypoints+floor(yuncertainty/2),mheight);
70 upout=upp(ypoints+floor(yuncertainty/2),mheight)/upd;
71 Uout=ucavgnet+(um-ucout)./upout;
72
73 % uncertainty in belt velocity
74 Uboundarystd=0.0001*Voltage+0.03;
75 ucavgnetstd=ucavg*Uboundarystd;
76 upstd=upout*0;
77 ucstd=ucout*0;
78 % uncertainty in measurement location
79 for i=1:length(ypoints)
80     upstd(i)=sqrt(1/((2*zuncertainty+1)*(yuncertainty+1))*sum(sum((upp(ypoints(i):
        ypoints(i)+yuncertainty,mheight-zuncertainty:mheight+zuncertainty)/upd-
        upout(i)).^2)));
81     ucstd(i)=sqrt(1/((2*zuncertainty+1)*(yuncertainty+1))*sum(sum((uc(ypoints(i):
        ypoints(i)+yuncertainty,mheight-zuncertainty:mheight+zuncertainty)-ucout(i)
        /Uboundary).^2)));
82 end
83 ucoutstd=sqrt((ucstd./uc(ypoints(i),mheight)).^2+(Uboundarystd/Uboundary).^2).*
    ucout;
84 if Uboundary==0
85     ucoutstd=ucout*0;
86 end
87 %uncertainty in the calculated average velocities
88 Uoutstd=sqrt(ucavgnetstd.^2+1/upout.^2*(umstd.^2+ucoutstd.^2)+(um-ucout).^2./upout
    .^4.*upstd.^2);
89 %Combination of all velocities to get 1 value.
90 Uaverage=(sum(Uout./Uoutstd.^2)./sum(1./Uoutstd.^2));
91 Uaveragestd=sqrt(1./sum(1./Uoutstd.^2));
92
93
94 disp('relative error measurement')
95 disp(sum(umstd./um)/length(um))
96 disp(max(umstd./um))
97 disp('Uaverage')
98 disp(Uaverage)
99 disp('Uaveragestd')
100 disp(Uaveragestd)
101
102
103 umstd1=T(datmin:datplus,4);
104 umstd2=T(datmin:datplus,6);
105 TI=sqrt(1/3*(umstd.^2+umstd1.^2+umstd2.^2))/Uaverage;
106 disp('TI')
107 disp(sum(TI)/length(TI))
108 disp(max(TI))
109
110 disp('uavgmeasured')
111 disp(sum(data(2:length(data),2))/length(data(2:length(data),2)))

```